Università degli Studi di Firenze

DOTTORATO DI RICERCA IN

"Ingegneria Industriale e dell'Affidabilità"

CICLO *XXV*

COORDINATORE Prof. Mario Tucci

DEVELOPMENT OF AN INNOVATIVE LOCALIZATION ALGORITHM FOR RAILWAY VEHICLES

Settore Scientifico Disciplinare ING-IND/13

Dottorando
Ing. *Gregorio Vettori*

Tutore
Prof. *Benedetto Allotta*

Anni 2010/2012

Ai miei genitori e a mia nonna Bruna per il profondo legame di affetto e di comprensione che ci unisce

A nonno Siliano che, anche da lassù, continuerà ad essere orgoglioso di me

A Valentina per la fiducia e l'amore reciproco

Contents

List of Figures

List of Tables

Ringraziamenti

Questa tesi di dottorato nasce dal coinvolgimento del Dipartimento di Energetica “S.Stecco” dell’Università di Firenze in un progetto a cui ha preso parte il laboratorio di Modellazione Dinamica e Meccatronica (MDMLAB) del Dipartimento stesso, con sede a Pistoia, presso l’ITTS “Silvano Fedi” e l’azienda ECM Spa di Serravalle Pistoiese.

Questa esperienza, in unione con le altre attività svolte nei tre anni di dottorato, ha arricchito molto le mie competenze teniche, organizzative e relazionali, dando un vero slancio alla mia professione.

Di questo, quindi, non posso che ringraziare il Prof. Paolo Toni e il Prof. Benedetto Allotta che mi hanno sempre seguito con grande professionalità ed attenzione, riponendo su di me grosse aspettative, alle quali spero di aver risposto positivamente, e alimentando il mio senso di responsabilità, impegno e motivazione per le discipline della robotica, del segnalamento ferroviario e della meccatronica in generale.

Una menzione particolare al Magnifico Rettore dell’Università di Firenze, Prof. Alberto Tesi, che mi ha conosciuto come giovane studente, insegnandomi i fondamenti dell’automazione, ed ha sempre creduto in me, .

Mi sento, inoltre, di ringraziare tutti i colleghi con i quali ho instaurato un rapporto di amicizia, stima e collaborazione reciproca, a cominciare dagli Ing. Alessandro Ridolfi, Riccardo Costanzi, Luca Pugi e Monica Malvezzi con i quali ho lavorato a fianco in molti progetti, continuando con l’Ing. Andrea Rindi, sempre attento alle mie istanze logistiche, ai colleghi con i quali ho condiviso una piacevole “convivenza” nel laboratorio di Pistoia, ovvero gli Ing. Yurj Auciello, Fabio Bartolini, Lorenzo Marini, Niccolò Monni, Johnatan Gelli e Marco Natalini, e, infine, ma non meno importanti, i colleghi “fiorentini”, gli Ing. Susanna Papini, Enrico Meli, Mirko Ignesti, Roberto Conti, Francesco Cangioli, Stefano Falomi, Alice Innocenti.

Un doveroso e caloroso ringraziamento ai tesisti per la collaborazione nelle varie attività di questo lavoro, Francesca Giardi, Lorenzo Becciolini, Fabrizio Michelotti e Lorenzo Damiano, e al personale di ECM, in particolare l’Ing. Filippo Salotti e l’Ing. Lorenzo Landi, che mi hanno sempre supportato con strumenti, e utili con-

sigli tecnici, mettendomi a disposizione gli spazi e le strumentazioni dell'azienda.

Infine un ringraziamento sentito ai miei genitori Marcello e Mariateresa che hanno sempre creduto nelle mie potenzialità, sostenendomi con amore e coinvolgimento per il concretizzarsi dei miei sogni, ai miei nonni Bruna e Siliano, per i quali sono sempre stato motivo di orgoglio, a Giovanni, Maura e Milena, per il sostegno, e poi un bacio speciale a Valentina per il reciproco sentimento di fiducia e amore.

Firenze, 19 Dicembre 2012

Gregorio

Introduction

The aim of this work is the development of an innovative localization algorithm for railway vehicles.

Since the importance of monitoring and control systems is continuously growing up in the modern railway network, train protection systems are essential to increase the infrastructure capacity, by maintaining a proper level of operation safety.

Automatic Train Control (ATC) is the term adopted to describe the architecture of train safety systems, by automatically guarding against the consequences of driver mistakes. It is composed of Automatic Train Protection (ATP), Automatic Train Operation (ATO) and Automatic Train Supervisor (ATS).

ATP [28, 2, 3] is essential for increasing the safety of rail transport, as it ensures that trains comply with speed restrictions. The system can help to prevent collisions through a driver's failure to observe a signal and stop the train independently in these circumstances.

For this reason, since the early nineties, all the major European countries have developed some domestic systems, i.e. the Italian "Sistema Controllo Marcia Treno" (SCMT).

Since the last 90s (Directive 96/48/EC) the European Union has defined the standards, procedures and technologies for interoperable rail signaling system at the European level ("European Rail Traffic Management System", ERTMS), in order to permit the transit of trains over the boundaries of individual countries, without the need to replace locomotives and/or personnel, while maintaining high the security level of the system.

ERTMS [55, 38, 39, 37] is a particularly advanced ATP and, in particular, there are three different levels for the same ERTMS:

- ERTMS Level 1: it requires a traditional signaling system, since it provides information to the driver by the light signals similar to those used for the traffic control for cars. The system has the task of checking that the driver adjusts the traction/braking in a way compliant with the signaling instructions and activate automatic braking when this does not happen;

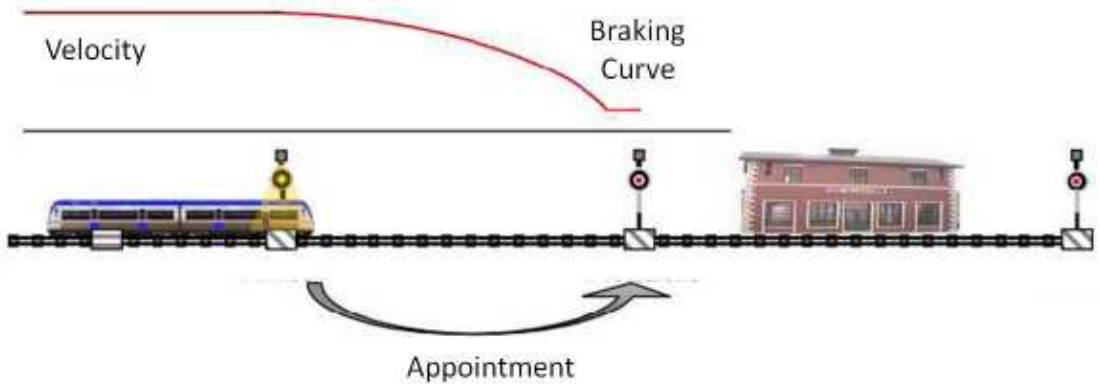

Figure 1: Signaling system with fixed informative points

- ERTMS Level 2 and 3: they are independent to the existence of the traditional type signaling system. Through a continuous exchange of information between devices on-track and on-board, the pilot shall receive all the necessary information on the dashboard to adjust the running of the train.

The electronic devices placed along the railway line are the track subsystem in itself (called "SottoSistema di Terra", SST, in the Italian signaling system); electronic equipment installed on the train, instead, are the on-board subsystem ("SottoSistema di Bordo", SSB). The transfer of data from the SST to the SSB takes place through the so called "Informative Points", which could be fixed or variable. The fixed balises *, which are part of the SST, give to the train a series of information:

- the current position
- distance to a target where speed restrictions have to be achieved
- target speed not to be exceeded when the train passes through a target point

Between two succeeding information acquisitions from the SST, the SSB continuously calculates a *Braking Curve*, a reference speed dependent to the distance to target, which it must not be exceeded, otherwise the automatic braking is activated (see Fig. 1), [10, 9].

A reliable estimate of distance to target and actual velocity is crucial to evaluate braking resources, in terms of available deceleration, in order to reach the target at the required speed. An error on the train position may lead to a potentially dangerous overestimation of the distance available for braking.

The instantaneous localization of a train on the track is provided by the on-board module called *Odometry* by dead reckoning and/or absolute navigation. The

*electronic beacon or transponder placed between the rails of a railway

word odometry is composed from the Greek words ὸδος (meaning "travel", "journey") and $\mu\epsilon\tau\rho o\nu$ (meaning "measure").

About vehicles, the word odometry usually refers to the use of data derived from sensors, typically on the wheels, for estimating the motion of the complete vehicle. The basic concept is developing a mathematical model that describes how the motions of the wheels, joints, etc., induce the motion of the vehicle itself. Then, integrating with respect to time of these specific motions, it is possible to develop a model of the pose of the vehicle as a function of time. The use of odometry information in order to know the pose of the vehicle as a function of time is known as "dead reckoning" and finds wide application in underwater and terrestrial navigation. Typically, in railway application the dead reckoning relies on wheel angular speed sensors, but other type of sensors can be used: radar Doppler sensors, accelerometers, gyroscopes, etc.

The reliability of dead reckoning is then related to the working conditions in which the sensors operate. For instance, wheel angular speed sensors located on two independent wheels give a reliable and accurate estimation of the train speed, but only when good adhesion conditions between wheel and rail occur. When pure rolling conditions do not hold anymore and macroscopic sliding occurs, the estimated error may become very high.

The development of an innovative *Odometry Algorithm* based on cheap and easy-to-install sensors responds to the need of *ECM Spa*[†] company to enhance the reliability of odometric estimation. This work, in fact, has been supported by ECM S.p.A. within the project COINS (Cooperative Odometry-Inertial Navigations System), funded by Regione Toscana under the program "BANDO UNICO R&S anno 2008 - linea A".

Sensor fusion techniques based on Kalman Filter theory have the potentialities to increase the accuracy of the localization, compared to the commonly adopted solutions, especially in critical adhesion conditions. The strategies of data fusion allow to make up for the limits and the drawbacks of each single sensor, whose information is properly weighted according to specific operative conditions.

The rapid technological development of low cost Micro Electro-Mechanical Systems (MEMS) Inertial Measurement Unit (IMU) made very interesting the integration of Inertial Navigation System (INS) into odometric estimation. An important part of the dissertation consists in the study of this type of inertial sensors, through theoretical analysis and experimental verifications.

[†]Italian company located in Serravalle Pistoiese (Pistoia, Italy), which provides solutions and technologies for the safety, control and enhancement of railway infrastructures - www.ecmre.com

In order to guarantee the robustness and the safety of the proposed solution the odometric algorithm should be tested with a huge number of real cases. Since the realization of experimental runs is difficult and expensive, a Hardware in The Loop test rig has been implemented. The opportunity to set up a testing simulator capable of replicating in a realistic fashion the dynamic effects of the vehicle motion on inertial sensors allows to avoid expensive on-board acquisitions and to speed up algorithm tuning. The Hardware-In-The-Loop test rig is composed of a Matlab-Simulink 3D multibody model of a railway vehicle able to reproduce most of the conditions that may affect the reliability of the sensors, a commercial anthropomorphic manipulator with spherical wrist and an IMU designed by ECM Spa.

The reliability of the speed and distance estimates have to be taken into account with respect to the performance requirements fixed by the European Rail Traffic Management System (ERTMS).

Original contribution on the thesis

The main innovative contribution of this work is the development of a low-cost inertial platform based on MEMS sensors and the relative localization algorithm for the train localization, which is going to become an industrial product of the portfolio of the company involved in the project, ECM spa. Any vendors, in fact, have not yet developed an odometry application based on the sensor fusion between an IMU sensors and a tachometer.

In the detail of the design choices, the integration of a triaxial accelerometer can be considered an innovating alternative compared to the classical choice of a monoaxial accelerometer. This choice allows to recover the misalignment errors due to the assembling errors.

The latest in railway application is the use of a triaxial gyroscope. Its contribution is basic in the estimation of the attitude of the train, in particular for the real-time line gradient estimation which is relevant for the correct compensation of gravity from the accelerometers.

The strategy adopted for the estimation of the attitude of the train, the so called "Orientation Kalman Filter", is innovative since it allows managing the native error in INS estimators, through the identification of some particular conditions (Coasting phase, Straight line, ecc.) and the subsequent actions of reset of the estimates.

Another relevant contribution given to the application is the possibility to use only one tachometer; by the contrary, classical applications need two tachometers, as the minimum setting of sensors for the estimation of the adhesion of the wheels. The solution proposed in this work exploits a reliable acceleration criterion deriving from the robustness of the orientation estimator. The omission of one tachometer has a relevant and positive impact on the devices, since these sensors show a lot of mechanical and maintenance problems.

As regards the testing of the algorithm, this dissertation offers an important contribution in developing a Hardware In the Loop (HIL) test rig being able to replicate in a realistic way the dynamic effects of the vehicle motion on inertial sensors. The opportunity to set up this testing simulator allows to avoid expensive on-board acquisitions and speeding up algorithm tuning.

The adaptation to the testing of inertial sensors can be considered an original application for the main software component of the test rig, i.e. the Washout Filters. In fact, WFs are usually used in flight or drive simulators in order that the pilot would experience the same dynamic effects as in the real scenario.

Structure of the thesis

This thesis resumes the activities that allowed to define the structure of the innovative localization algorithm, starting from the definition of the algorithm up to the testing of a *prototype* board.

The thesis starts with a beginning chapter which the state-of-the-art of the odometry algorithm for railway vehicle is reported in.

The second chapter introduces the concept of Inertial Navigation System; the considerations which lead to the definition of a sensor fusion strategy of integration between wheel angular speed sensors and an IMU are shown. Finally the main features of the innovative localization algorithm are described.

The third chapter deals with the preliminary results obtained in a simulated scenario through Matlab-Simulink^{TM}: this scenario includes a 3D multibody model of the railway vehicle, which provides kinematic inputs to the algorithm, a sensor mask which permits to take into account the errors of the sensors, a post-process procedure, based on Monte Carlo simulations, which provides a reliable benchmark for the testing of the algorithm performance.

The fourth chapter provides a theoretical study about the development of a dynamic simulator able to replicate in a realistic way the dynamic effects of the vehicle motion on inertial sensors: the differences caused by the adaptation of Washout Filters to the inertial sensors case are compared to the classical approach and the design of the strategy of feedback control for the tracking of the position and orientation values provided by Washout Filters is described. Preliminary simulation results based on the kinematic model of an available on market anthropomorphic robot are shown.

In the fifth chapter, the architecture of the Hardware In the Loop (HIL) test rig is described: each component of the dynamic simulator is described, in particular the open controller for the robot and the post-process procedure based on the Wavelet Transform. The results of the validation procedure of the HIL test rig, thanks to the available on the market IMU, MTi-G by Xsens, are displayed.

The sixth chapter deals with the design and the testing activities of the custom IMU board designed by ECM: i.e. the market research, for the identification of the

most suitable commercial MEMS sensors, the thermal analysis of the board, performed in the ECM climate chamber, and the testing activities through the HIL test rig previously defined. The last section reports the results of the application of the custom IMU board outputs, to be used as inputs for the localization algorithm.

Chapter 1

State of the art of odometry algorithms for railway applications

In this chapter the state of the art for odometry railway algorithms is reported. The researchers of the Department of Energy Engineering of University of Florence, since the last years 90s, have worked with the Italian Railway Companies (Trenitalia) in the design of the odometry algorithm for the Italian ATP system, named SCMT (Italian acronym for Sistema Controllo Marcia Treno), exploiting only data coming from of two encoders measuring axle angular speed, [6, 25]. A number of algorithms were analyzed and compared (for example based on fuzzy logic and neural networks), but the solution chosen by Trenitalia is based essentially on heuristic considerations in reason of higher integrity and safety targets [4]. A lot of papers about the sensor fusion techniques for the railway application have been investigated, [32, 33, 34, 14, 24]. An original approach is provided by [21], even though it is far from the target of this work.

The following sections explain in detail the solutions provided by the latest works of the University of Florence, which have been used as a starting point for the discussion of this thesis.

1.1 SCMT odometry algorithm

SCMT, the Italian ATP system, supports an odometry algorithm [6, 25] based on the measurement coming from two angular speed sensors on two independent axles.

1.1.1 Wheel Angular Speed Sensors

Wheel angular speed sensors are widely diffused in railway applications due to their robustness and reliability (e.g., they are exploited by the Wheel Slide Protection WSP and anti-skid systems). The sensor output is a signal proportional to the pulse counter c, in the generic time sample i. The wheel angular speed ω_i can be evaluated by finite derivatives as follows:

$$\omega_i = \frac{2\pi}{N}\frac{(c_i - c_{i-1})}{\Delta T} \tag{1.1}$$

where c_i is the current sample, c_{i-1} is the preceding sample, N is the number of impulses per revolution, ΔT is the sampling time.

From the wheel angular speed sensor measure the wheel peripheral speed can be calculated multiplying this value by the wheel radius.

$$v_i = R_i * \omega_i \tag{1.2}$$

It is worth to note that the wheel radius information sometimes may be not reliable, since railway wheels are subject to wear and periodical mechanical returnings. The weak point is the low reliability under degraded adhesion conditions [26], which is rather common in railway practice. If the wheel is not sliding this sensor provides a good and reliable estimation of the train speed, but, when the wheel-rail adhesion conditions are degraded and the train is accelerating or braking, pure rolling conditions between the wheel and the rail do not hold any more and macroscopic slidings arise.

$$v_i - R_i * \omega_i = \delta_i \tag{1.3}$$

If the train is accelerating the wheel peripheral speed tends to overcome the train speed ($\delta_i < 0$), while during the braking phase the wheel peripheral speed is lower than train one ($\delta_i > 0$). The dynamics of the wheels in sliding mode depends significantly on the mechanical feature of the vehicle (masses and inertia, geometric properties, suspension characteristics, etc.) and on the interaction among the different on board subsystems, in particular braking systems, WSP, traction systems and anti-skid, [41].

The adhesion conditions are estimated by means of two criteria:

- the so called *tachometric criterion* states that two wheels (or at least one of them) are sliding or skidding if the absolute value of the difference between

their wheel peripheral speeds (v_1, v_2) overcomes a fixed threshold (Δ_v):

$$|v_1 - v_2| > \Delta_v \tag{1.4}$$

- the *accelerometric criterion* compares the wheel peripheral accelerations: a wheel is sliding if the absolute value of its acceleration (a_1, a_2) overcomes a fixed threshold (Δ_a):

$$|a_1| > \Delta_a \qquad\qquad |a_2| > \Delta_a \tag{1.5}$$

The detection of the condition of the adhesion shows some weak points: in fact, if both wheels slide, the possibility that the "tachometric criterion" fails is high, as actually happens in its practical applications. In this case the "accelerometric criterion" should be able to recognize the sliding phase. In the worst-case of sliding of all the wheels and with low acceleration, both the criteria may fail.

The fake detection of the adhesion condition happens frequently on the railway network, so SCMT algorithm is often affected by non-negligible errors. If the estimated adhesion conditions are judged as "good", according to the previously mentioned criteria, the train speed can be evaluated directly from the peripheral speeds of the wheels.

When the wheels are sliding and the train is accelerating (or braking), the speed can be evaluated as the minimum (maximum) between the speeds of the two wheels and a speed estimate obtained by integrating a constant acceleration (deceleration) value, previously established, according to the dynamical performances of the train. Some different solutions were developed and compared, using a variety of methods including neural networks, fuzzy logic and crisp logic.

1.1.2 Trenitalia-Unifi Crisp Algorithm

The Trenitalia-Unifi Crisp Algorithm [4, 6, 25] is based on a series of if-then rules, devised on the basis of expert knowledge and of a series of experimental tests. The algorithm runs with a frequency of 10Hz: this value is a compromise between the precision of the estimation and the computational burden of the system.

The algorithm can be divided into a series of phases, as shown in Fig. 1.1:

1. Variable Initialization;
2. Data Acquisition and Conditioning;
3. State Variable Evaluation;

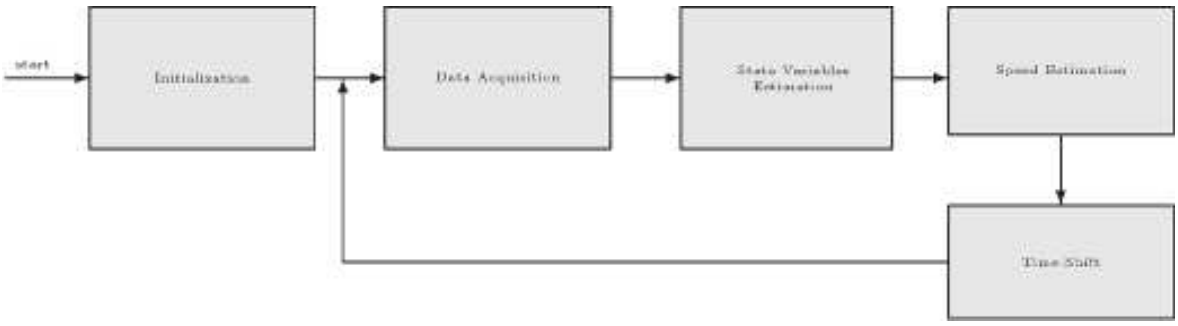

Figure 1.1: Trenitalia-Unifi Crisp Algorithm

4. Train Speed and Travelled Distance Evaluation;
5. Time Shift and Data Storing.

Variable Initialization

This phase consists of the following steps:

1. definition of parameters, i.e. thresholds, cut-off frequency filter, etc.;
2. initialization of variables.

Data Acquisition and Conditioning

The system reads the values stored in the counters, $c_1(i)$ and $c_2(i)$, and from them it evaluates wheel peripheral speeds, through Eq. 1.1. Then the wheel peripheral accelerations, $a_1(i)$ and $a_2(i)$, are evaluated using first-order finite differences and a first-order low-pass filter, in order to reduce the noise in the acceleration estimation.

State Variable Evaluation

On the basis of speed and acceleration information, the system decides whether pure rolling conditions between each wheel and the rail are verified or the axles are slipping or skidding, through tachometric and acceleration criteria (Eq. 1.4 and 1.5).

A logic variable is used to describe whether the train is accelerating or braking. If adhesion is good, this evaluation is made by comparing the mean between wheel accelerations with a fixed value that takes into account the internal and aerodynamic resistance and the line gradient. If adhesion is poor, the decision is taken by

ep value	Axle Stable	Estimation procedure
1 or -1	-	$\hat{v}(i)$=max$(v_1(i), v_2(i))$
2 or 3	Yes	$\hat{v}(i)=v_k(i)$
2 or 3	No	$\hat{v}(i)=\hat{v}_k(i-1)+\hat{a}\,T$
4	-	$\hat{v}=\hat{v}(i-1)$
- 2 or - 3	-	$v_{ref}(i)$=min$(v_1(i), v_2(i))$ $a_{ref}(i)=a_1(i)$ if $v_1 < v_2$ $a_{ref}(i)=a_2(i)$ otherwise $\hat{v}(i)=v_{ref}(i)$ if $a_{ref}(i)<a_{max}$ $\hat{v}(i)=\hat{v}(i-1)+a_{max}T$ if $a_{ref}(i)>a_{max}$

Table 1.1: Estimation procedure

observing the sign of the difference between the mean acceleration and the fixed threshold for a fixed time window.

The speed of a wheel can be considered “stable” if its acceleration and variation of acceleration is “small” for a fixed time interval.

The type of evaluation procedure is represented by an integer variable, ep, which can assume seven possible values corresponding to seven different situations:

1. slipping phase, ep = -3;
2. not certain adhesion in an accelerating phase, ep = -2;
3. adhesion in an accelerating phase, ep = -1 ;
4. adhesion in a braking phase, ep = 1;
5. not certain adhesion in a braking phase, ep = 2;
6. skidding phase, ep = 3;
7. beginning of a skidding phase, ep = 4;

Train Speed and Travelled Distance Evaluation

Once the state of the system has been evaluated, the algorithm decides the type of speed estimation and computes train speed and position. The different estimation procedures are summarized in Tab. 1.1.

Time Shift and Data Storing

The final step is devoted to the memorization of variable values relative to the present sample. The vectorial variable components are shifted in order to allow the memorization of the subsequent value.

1.1.3 Soft Computing Alternatives

An alternative version of the odometry algorithm has been studied and its structure is similar to the one of Fig. 1.1, but the state variable and the speed estimation blocks of the Trenitalia-Unifi crisp algorithm are substituted by a soft computing based procedure.

In particular both fuzzy inference systems and neural networks [6, 11] have been evaluated. These solutions show much better performance and efficiency with respect to the crisp algorithm, but, on the other hand, do not allow an immediate correspondence to be established between parameter values and physical quantities that are easily measured.

1.2 ERTMS Solution

The ERTMS system [27] uses a set of sensors including two encoders positioned on two independent axles, a radar sensor positioned on the locomotive case and a longitudinal accelerometer. In fact the ability of one isolated sensor to provide accurate reliable data is limited as the environment is usually not very well defined. Furthermore the environmental condition may vary during train operations, and each sensor has a limited range in which it has optimal performance. Sensor fusion techniques allow to limit the drawbacks of single sensors by combining information from independent sources, in order to extract better information in terms of accuracy and reliability. Furthermore data fusion techniques are able to reduce the system vulnerability to failure of a single components and can provide more accurate informations.

1.2.1 Monoaxial accelerometer

A reliable measure of train longitudinal acceleration could be very useful in the odometric evaluation in order to recognize particular operative conditions, e.g. wheel adhesion losses and slidings. Moreover when the reliability of the other sensors is low, train acceleration measure could also be used to roughly estimate train speed and travelled distance by numerical integration. The main characteristics of the ideal accelerometer suitable for this application are:

- low bandwidth (about 2-3 Hz);
- possibility of measuring continuous accelerations;

- robustness and high insensitivity to lateral (or vertical) acceleration components.

The accelerometer is then able to measure the train "real" longitudinal acceleration, but, if the sensor sensitive axle is not perfectly assembled and/or train acceleration is not only longitudinal (presence of vertical and/or lateral components) the accelerometer output signal could be affected by a significant error. For example if the sensor sensitive axis is not perfectly perpendicular to the gravity vector, the output signal is not null, even if the accelerometer is perfectly still (the accelerometer works as an inclinometer).

In order to quantify the error due to the sensor misalignment and to the lateral (or vertical) acceleration components, two reference systems were then defined as follows.

The former is fixed on the track, its origin O_0 is a generic point in rail plane, the z_0 axis is vertical and ascending, the x_0 axis is in rail plane and aligned with track longitudinal direction, the y_0 axis is consequently defined (lateral direction).

The latter reference system is fixed on the sensor and its x_1 axis is along the accelerometer sensitive axis. Because of track gradient and vehicle dynamics on suspension system, the two reference systems are usually misaligned in operative conditions (see Fig. 1.2).

The relative orientation between the two reference systems can be, as usual, described by the Euler Angles, i.e. Roll-Pitch-Yaw angles (ψ, θ and ϕ). The rotation matrix expressed as a function of these angles is:

$$R = \begin{bmatrix} c(\phi)c(\theta) & c(\phi)s(\theta)s(\psi) - s(\phi)c(\psi) & c(\phi)s(\theta)c(\psi) + s(\phi)s(\psi) \\ s(\phi)c(\theta) & s(\phi)s(\theta)s(\psi) + c(\phi)c(\psi) & s(\phi)s(\theta)c(\psi) - c(\phi)s(\psi) \\ -s(\theta) & c(\theta)s(\psi) & c(\theta)c(\psi) \end{bmatrix} \tag{1.6}$$

The absolute acceleration referred to the body on which the accelerometer is located, is represented in the fixed reference system by the following vector:

$$\vec{a}^0 = \left[a_x^0 \; a_y^0 \; (a_z^0 + g) \right]^T \tag{1.7}$$

which may be easily expressed in the local sensor-mounted reference system as follows:

$$\vec{a}^1 = R^T \vec{a}^0 \tag{1.8}$$

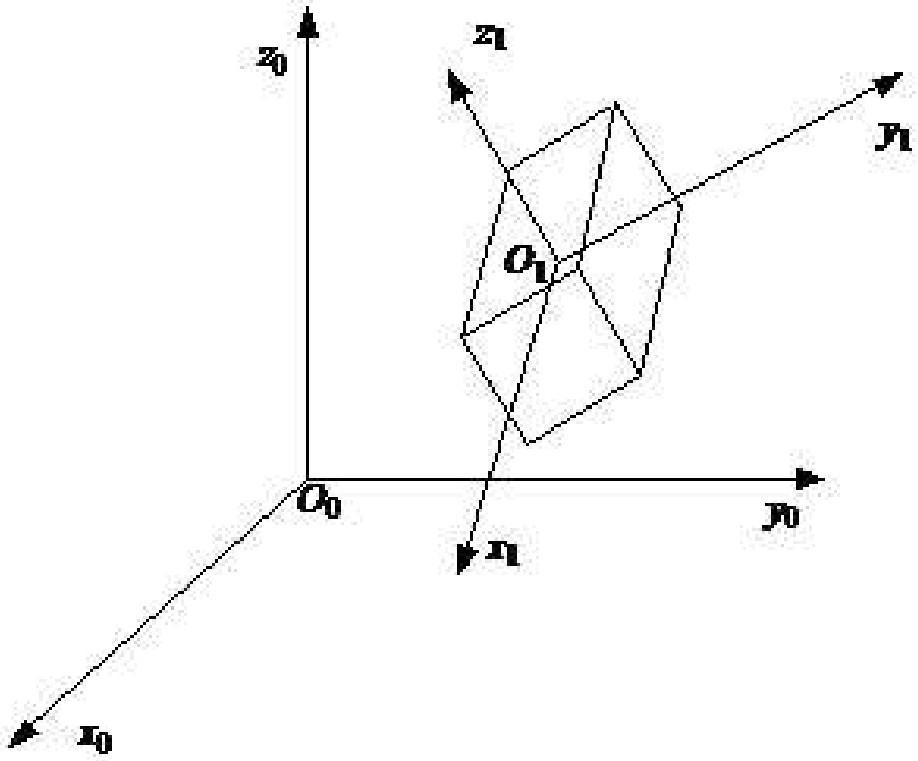

Figure 1.2: Fixed and accelerometer reference frames

Since the sensor output is only proportional to the force component aligned to the x_1 axis direction, the measured acceleration can be expressed as follows:

$$a_m = a_x^1 = \cos(\phi)\cos(\theta)a_x^0 + \sin(\phi)\cos(\theta)a_y^0 - \sin(\theta)(a_z^0 + g) \tag{1.9}$$

The sensor output signal does not depends significantly on the angle ψ (roll angle). The acceleration component in the lateral direction a_y^0 influences the measure only if $\phi \neq 0$. The angle θ, which includes the pitch motion of the vehicle and the line gradient, influences strongly the measurement since it is amplified by the gravity.

If the accelerometer is correctly mounted on the vehicle and it does not have significant angular dynamics during the operative conditions, the sensitive axis coincides with the longitudinal direction, so $\psi = \theta = \phi = 0$ and consequently $a_m = a_x^0$: the sensor correctly measures the longitudinal acceleration.

In case of line gradient ($\theta \neq 0$, $\psi = \phi = 0$), the sensor output (a_m, measured acceleration) is:

$$a_m = \cos(\theta)a_x^0 - \sin(\theta)(a_z^0 + g) \tag{1.10}$$

The effect of the line gradient can be compensated if the information about the gradient (i_c, corresponding to an inclination angle θ_c) is communicated to the on-board subsystem by the balises of the ground signaling subsystem.

$$a_m = \frac{1}{\cos(\theta)}\big(a_m - g\sin(\theta)\big) \cong a_m - g\tan(\theta_c) = a_m - g\,i_c \tag{1.11}$$

The approximations introduced in the previous expression is generally acceptable since the line gradient is small. For this aim, the maximum gradient line the railway tracks supports, about 3%, helps. Unfortunately the balises provide the information of track gradient as mean or minimum value; this lack of instantaneous information penalize the use of the accelerometers. The error due to other types of misalignment and the presence of lateral/vertical acceleration components cannot be compensated without adding other sensors.

1.2.2 Radar Doppler

A radar Doppler sensor measures the relative speed between the body on which it is located and the surface on which it points, by detecting the frequency shift between the transmitted and the reflected signals. The reliability of the measure depends on different parameters and it can be affected by non negligible errors. For example an extremely smooth surface may cause offsets and systematic error in the measure and it is furthermore highly influenced by the vehicle dynamics (pitch motion, local vibrations, etc.), [42].

Because of a number of economic, safety and reliability reasons, it was not included in the ERTMS odometric solution proposed by the Department of Energy of University of Florence.

1.2.3 ERTMS Algorithm

The ERTMS solution, so as provided by the Department of Energy in [27], shows the same architecture as that shown in Fig. 1.1. In the next paragraphs the differences with the SCMT algorithm are highlighted.

Data Acquisition and Conditioning

As in the SCMT algorithm, the peripheral wheel velocities are calculated by means of numerical derivatives, starting directly from the pulse counters, and then elaborated by derivative filters, in order to obtain an estimation of the peripheral wheel acceleration, too.

The accelerometer is measured and corrected taking into account the information of the line gradient available from the on track subsystem, according to Eq. 1.10. It is then evident that the reliability of the corrected acceleration is strictly related to the reliability of the information of the line gradient.

State Variable Evaluation

The State Variable Evaluation is yet based on tachometric and accelerometric criteria. With respect to the SCMT algorithm the difference stands on the second criterion, since it compares the wheel peripheral accelerations with the train mounted accelerometer measure: a wheel is sliding if the absolute value of the difference between its acceleration and those measured by the accelerometer overcomes a fixed threshold. So for each axis the degraded adhesion condition is verified if:

$$|v_1 - v_2| > \Delta_v \text{ or } \left|a_i - a_{mc}\right| > \Delta_a \tag{1.12}$$

where i=1,2 refers to the axle, a_{mc} is the compensated acceleration measurement and Δ_a is the threshold.

State variables, as those explained in the Sect. 1.1.2, are calculated combining information from the adhesion conditions, the stability of the axles and the type of phase (braking or traction).

Train Speed and Travelled Distance Evaluation

If the adhesion conditions are estimated "good", the train speed can be evaluated directly from the peripheral speeds of the wheels:

$$v(i) = \max(v_1(i), v_2(i)) \tag{1.13}$$

When the wheels are sliding and the train is accelerating, the speed is evaluated as the minimum between the speeds of the two wheels and a "reference" value obtained by integrating the estimated train acceleration:

$$v(i) = \min(v_1(i), v_2(i), v(i-1) + a_{est}\,T) \tag{1.14}$$

where the estimated acceleration a_{est} is calculated as a function of the train acceleration measured by the accelerometer and the mean between the wheel peripheral accelerations:

$$a_{est} = \max\left(\min\left(\frac{a_1 + a_2}{2}, a_m + \Delta a\right), a_m - \Delta a\right) \tag{1.15}$$

If the wheels are sliding and the train is braking, the speed is evaluated as the maximum value among the between the two wheel peripheral speeds and the velocity value obtained by integrating the estimated train deceleration:

$$v(i) = \max(v_1(i), v_2(i), v(i-1) - d_{est}\,T) \tag{1.16}$$

The estimated deceleration d_{est} is calculated as a function of the measured train and the mean value between wheel peripheral accelerations:

$$d_{est} = \max\left(\min\left(-\frac{a_1 + a_2}{2}, -a_m + \Delta d\right), -a_m - \Delta d\right) \tag{1.17}$$

When the system recognizes the beginning of a sliding during a braking phase, starting from an initial adhesion phase, the estimated speed remains constant for a time interval whose amplitude depends on the speed. This allows to compensate eventual delays in the recognition of the sliding due to the effect of the filters used in data acquisition/storage modules.

The travelled distance is then evaluated as numerical integration of the estimated speed v_i as follows:

$$s(i) = s(i-1) + v(i)T \tag{1.18}$$

The traveled distance estimation is reset when the train passes on a track reference point (balise).

Chapter 2

Design of the innovative localization algorithm

The state-of-the-art of the localization algorithms for railway vehicles shows that during the last few years, complex algorithms have been developed. They are mainly based on the tachometers installed on two independent axles and on hypothesis on the maximum acceleration or deceleration performed by a train. These algorithms are able to reach an accuracy on the estimation of position and speed, considered sufficient for practical purposes.

But these solutions show the following problems:

- the wheel diameter greatly affects the accuracy and varies over time due to the consumption of material (wear), needing complex operations of recalibration of the algorithm parameters;
- odometric algorithms are very sensitive to phenomena of sliding, which increase significantly the uncertainty in the estimation of velocity and acceleration;
- installation and maintenance of tachometers is complicated and expensive.

Furthermore the more advanced solutions which exploit other kind of sensors, such as radar Doppler or monoaxial accelerometer, show the following drawbacks:

- the precision of the radar Doppler depends too much on the conditions of the surface on which the sensor points;
- the measurement of the train longitudinal acceleration carried by a monoaxial accelerometer is affected by lateral or vertical components due to the assembly errors;

- a non reliable estimation of the line gradient causes non negligible errors in the compensated body longitudinal acceleration.

In order to overcome the drawbacks of each type of sensor and thus improve the quality of the estimate the use of sensor fusion techniques has been evaluated appropriate. These data fusion strategies try to combine measurements from various types of independent sensors, so as to extract the best information in terms of accuracy and reliability. The use of multiple types of sensors also reduces the vulnerability of the system with respect to faults of each individual components.

Moreover the development of the Micro Electro-Mechanical Systems (MEMS) technology, in terms of continuous decrease of the price and the dimension of sensors such as accelerometers, gyroscopes, magnetometer, etc. helps MEMS to expand penetration into diverse applications: automotive electronics, hard disk drives, wireless devices, medical equipment, smartphones and other portable electronics.

So the combination of the necessity to resolve the issues, previously summarized, and the opportunity given by this innovative range of cheap sensors, have opened the road for the idea of approaching the problem of localization of the train with original solutions, exploiting the technological advances in the field of Inertial Navigation Systems and GPS localization.

2.1 Inertial Navigation Systems

An inertial navigation system is based on the laws of Newtonian mechanics. The advantage of an inertial system is to be fully contained within the vehicle, i.e. there is no need of any external reference to determine its position, its orientation, or its speed. The Inertial Navigation Systems [57, 40, 36, 49] allow estimating the current position of a vehicle by means of the measure of its translational and rotational motion with respect to an inertial reference system.

Therefore, before proceeding with the description of sensors needed, it is important to define the reference systems used in these applications. It follows the description of some of the systems described in the literature (see Fig. 2.1) (it is specified that these reference systems are all orthogonal and right-handed):

- Inertial frame (i-frame): has the origin in the center of the earth and its axes do not rotate with respect to the fixed stars. Its z axis coincides with the polar axis of the Earth. Strictly speaking, it is the only reference system which could be called “inertial”;

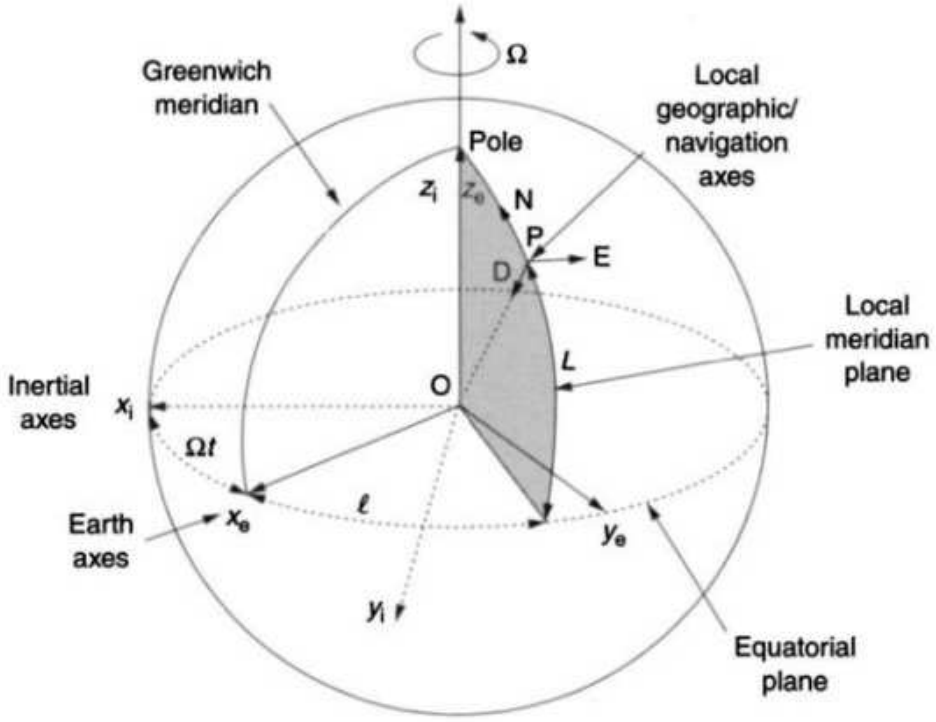

Figure 2.1: Reference systems used in the Inertial Navigation Systems

- Earth frame (e-frame): has the origin in the center of the earth and axes fixed with respect to the earth itself. Its z axis coincides with the polar axis of the Earth, its x axis, instead, is defined by the intersection of the equatorial plane with the plane of the meridian of Greenwich. The e-frame rotates with respect to the i-frame with angular velocity Ω along the z axis;

- Navigation frame (n-frame): is a local geographic with origin coincident with the location of the origin of the inertial navigation system (the point P in Fig. 2.1) and the axes defined by the direction of North, East and the local vertical (toward the center of the earth). The change of orientation of the n-frame with respect to the e-frame depends on the motion of the point P (and thus by the motion of the vehicle) with respect to the Earth;

- Body frame (b-frame): has its origin at the point of the vehicle on which the inertial sensors are installed; its axes are aligned with the roll, pitch and yaw axes of the vehicle itself.

In order to introduce the description of the sensors, it is worth to note that the estimated speed and position of the vehicle are essentially obtained as successive time integrations of the acceleration measurements provided by accelerometers. Usually a triaxial accelerometer is used, so as to be capable of measuring the acceleration in each direction. The measuring of the accelerometers follows the b-

frame, the gyroscopes, instead, allow rotating the measurements of acceleration in the inertial reference system.

So the application of INS techniques in the railway context requires the use of a platform, mounted on the vehicle, which contains an Inertial Measurement Unit (IMU) and other sensors that may be useful in the localization, such as the magnetometers and the GPS.

2.1.1 Inertial Measurement Unit

IMU (Inertial Measurement Unit) is an electronical device composed of a triaxial accelerometer and a triaxial gyroscope. It can measure triaxial b-frame acceleration:

$$\vec{f}^b = \begin{bmatrix} f_x^b & f_y^b & f_z^b \end{bmatrix}^T \tag{2.1}$$

and triaxial b-frame angular rate:

$$\vec{\omega}^b = \begin{bmatrix} \omega_x^b & \omega_y^b & \omega_z^b \end{bmatrix}^T \tag{2.2}$$

The accelerometer provides an output proportional to the non-gravitational force per unit mass (f) to which the sensor is subjected along its sensitive axis (an acceleration dimensionally); it is, instead, insensitive to the gravitational acceleration (g). In order to retrieve the acceleration due to the movement (a), the following operation must be performed:

$$a = f + g \tag{2.3}$$

Gyroscopes measure angular rates in correspondence of rotations of the platform where IMU is assembled with respect to the i-frame inertial frame.

Classical IMUs are very expensive and very accurate, but modern accelerometers and gyros are often small Micro Electro-Mechanical Systems (MEMS) with low cost and quite high noise. For this reason, the error sources of accelerometer and gyroscope (respectively e_a and e_g) are not negligible and have to be taken into account:

$$\begin{aligned} \bar{f} &= f + e_a = f + b_a + S_a f + m_a f + \eta_a \\ \bar{w} &= w + e_g = w + b_g + S_g w + m_g w + \eta_g \end{aligned} \tag{2.4}$$

where, $\bar{\cdot}$ denotes the measured value by the sensor, the subscript a means ac-

celerometer specific errors, and g means gyroscope specific errors. The symbols in Eq. (2.4) mean: f is the specific force, w is the angular rate, b is the sensor bias, S is the scale-factor error, m is the assembly error, and η is the sensor random noise. The bias is generally composed of two parts, a deterministic bias offset and a random bias-drift. A focus on each error source will be open in Sect. 3.2.

2.1.2 Magnetometer

A magnetometer is a device used to measure the strength and the direction of the magnetic field near the instrument and, in lack of local magnetism, it can detect Earth's magnetic field. A three-axis magnetometer $m = [m_x \; m_y \; m_z]$ can be used to improve the orientation estimate (Roll, Pitch, Yaw). A variety of systematic errors [17] can get worse the accuracy of these sensors, according to:

$$\bar{m} = C_m \cdot C_{sf} \cdot C_{si} \cdot (m + \delta m) + \eta_m \tag{2.5}$$

where, m is the Magnetic Field, δm represents the Hard Iron biases, C_{si} takes into account the Soft Iron errors, C_{sf} reckons with the scale factor errors, C_m represents the misalignment errors, and η_m is the sensor random noise.

2.1.3 GPS

GPS is the acronym for Global Positioning System and it is a location estimation technology. The system is based on received radio signals transmitted by satellites orbiting the Earth. The estimation provided is a three-dimensional position in absolute coordinates with accuracy of 10-20 m for standard implementations and 1-2 m for enhanced GPS such as Wide-Area Augmentation System (WAAS). The most widely accepted system is base on NAVSTAR satellite, deployed and maintained by the United States Army. The Russian government operates a similar system, named GLONASS, and another alternative is being deployed by the European Union, named Galileo.

GPS can guarantee absolute and drift-free position estimation but it can fail due to inaccessibility of a satellite signal in particular situations. Moreover GPS data frequency is lower (1-10 Hz) than on-board-sensor frequency (10-100 Hz). So GPS is not able to meet the basic requirements of integrity and availability and the vehicle can't be equipped only by a satellite receiver but also by inertial navigation sensor.

2.1.4 INS Navigation Algorithms

The outputs of the IMU can be processed to determine the position, velocity and attitude of a vehicle through algorithms called Inertial Navigation Systems (INS). The most detailed architecture of an INS algorithm is shown in Fig. 2.2 and represents the so called "Local reference strapdown mechanization algorithm" [57].

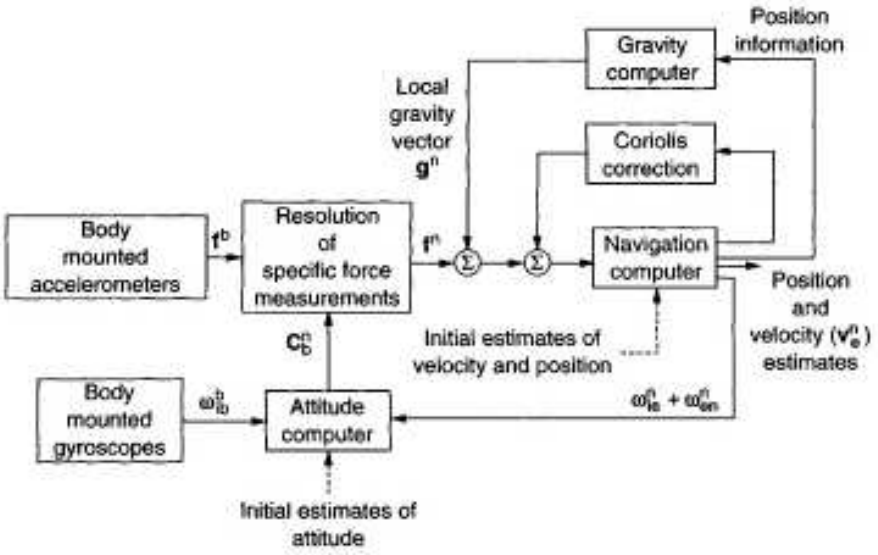

Figure 2.2: INS Algorithm

Attitude computation

The attitude of the body with respect to the chosen reference frame is required to resolve the specific force measurements into the reference frame, thus to compute an estimate for the rotation matrix C_b^n, which expresses the relationship between navigation and body frame.

The vector

$$\omega_{ib}^b = \left[(\omega_{ib}^b)_x \, (\omega_{ib}^b)_y \, (\omega_{ib}^b)_z \right]^T \tag{2.6}$$

represents the turn rate of the body with respect to the i-frame as measured by the gyroscopes.

In order to retrieve the body rate with respect to the navigation frame, ω_{nb}^b, the measured body rates, ω_{ib}^b are differenced with the estimates of the components of the navigation frame rate, ω_{in}. The latter term is obtained by summing the Earth's rate with respect to the inertial frame and the turn rate of the navigation frame with respect to the Earth, that is, $\omega_{in} = \omega_{ie} + \omega_{en}$.

$$\omega_{nb}^{b} = \omega_{ib}^{b} - C_{n}^{b}\left(\omega_{ie}^{n} + \omega_{en}^{n}\right) \tag{2.7}$$

The computation may be defined in a number of different ways: the most common are those based on the Euler angles and on the quaternion.

The first method exploits the nonlinear relationship between the derivatives of the Euler angles and the body angular rates:

$$\begin{cases} \dot{\psi} &= \left(\omega_y \sin(\psi) + \omega_z \cos(\psi)\right)\cos(\theta) + \omega_x \\ \dot{\theta} &= \left(\omega_y \cos(\psi) - \omega_z \sin(\psi)\right) \\ \dot{\phi} &= \frac{1}{\tan(\theta)}\omega_y \sin(\psi) + \omega_z \cos(\psi) \end{cases}$$

The Euler angles (ψ, θ, ϕ) are then computed by time integration and the rotation matrix calculated as Eq. 1.6.

The quaternion attitude representation is a four-parameter representation based on the idea that a transformation from one coordinate frame to another may be effected by a single rotation about a vector ϵ defined with respect to the reference frame.

The quaternion, denoted here by the symbol q, is a four element vector, the elements of which are functions of this vector and of the magnitude of the rotation:

$$\vec{q} = \begin{bmatrix} \cos\left(\frac{\eta}{2}\right) \\ \epsilon_x \sin\left(\frac{\eta}{2}\right) \\ \epsilon_y \sin\left(\frac{\eta}{2}\right) \\ \epsilon_z \sin\left(\frac{\eta}{2}\right) \end{bmatrix} \tag{2.8}$$

The quaternion-based attitude computation is made through:

$$\hat{q}(k+1) = \hat{q}(k) + \frac{1}{2}\Omega_k \hat{q}(k) dt \tag{2.9}$$

where k is the sample time and Ω_k is the 4x4 skew symmetric matrix based on the angular rate components:

$$\Omega_k = \begin{bmatrix} 0 & -\omega_z & \omega_y & \omega_x \\ -\omega_z & 0 & \omega_x & \omega_y \\ \omega_y & -\omega_x & 0 & \omega_z \\ -\omega_x & -\omega_y & -\omega_z & 0 \end{bmatrix} \tag{2.10}$$

The obtained 3x3 rotation matrix C_n^b is used to transform the acceleration mea-

surements from the *b-frame* to the *n-frame*. The quaternion approach, unlike the Euler angles, has the benefit to avoid the singularities.

It allows to calculate C_b^n, through the following:

$$C_b^n = \begin{bmatrix} 2(\eta^2+\epsilon_x^2)-1 & 2(\epsilon_x\epsilon_y-\eta\epsilon_z) & 2(\epsilon_x\epsilon_z+\eta\epsilon_y) \\ 2(\epsilon_x\epsilon_y+\eta\epsilon_z) & 2(\eta^2+\epsilon_y^2)-1 & 2(\epsilon_y\epsilon_z-\eta\epsilon_x) \\ 2(\epsilon_x\epsilon_z-\eta\epsilon_y) & 2(\epsilon_y\epsilon_z+\eta\epsilon_x) & 2(\eta^2+\epsilon_z^2)-1 \end{bmatrix} \tag{2.11}$$

Strapdown local navigation

The rotation matrix C_b^n expresses the relationship between navigation and body frame and is used to transform the acceleration measurements from the *b-frame* to the *n-frame*, therefore:

$$a^n = C_b^n f^b - (2\omega_{ie}^n + \omega_{en}^n) \wedge v^n + g^n \tag{2.12}$$

where f^b is defined in Eq. 2.1, g^n is the gravity vector equal to $[0\ 0\ -9.81]^T$, the term $(2\omega_{ie}^n + \omega_{en}^n) \wedge v^n$ is the sum of two correction terms: the first caused by the vehicle's velocity over the surface of a rotating Earth, usually referred to as the Coriolis acceleration, the second by the centripetal acceleration of the vehicle, resulting from its motion over the Earth's surface.

It is then possible to estimate the velocity of the vehicle (v^v), through an integration of the transformed acceleration:

$$v^n = \begin{bmatrix} v^N & v^E & v^D \end{bmatrix} = \int a^n dt \tag{2.13}$$

where v^N is the speed along the North side, v^E is the speed along the East side and v^D is consequently the speed toward the bottom.

A second temporal integration allows to calculate the position in the fixed reference:

$$p^n = \begin{bmatrix} p^N & p^E & p^D \end{bmatrix} = \int v^n dt \tag{2.14}$$

In literature [57], among other things, it is possible to find:

- the effective quantification of ω_{ie}^n and ω_{en}^n as function of the angular velocity, the radius of the Earth and the height above the surface of the Earth;
- the effect on gravity of the combined effects of the mass attraction of the Earth and the centripetal acceleration caused by the Earth's rotation;

- the relationship between the position expressed in the fixed frame and the coincident value of latitude and longitude.

Sensor error propagation

The lack of the strapdown INS algorithm is that it blindly processes the raw inertial data affected by errors and, due to time integration performed, introduces errors in attitude $\delta\Phi$, velocity δv and position δp. The orientation error ($\delta\Phi$), coming from the integration of the angular rates, causes an incorrect projection of the acceleration signals onto the global axes, i.e. a tilt error ($\delta\theta = e_g t$) will cause a component of the acceleration due to gravity with magnitude, $g\sin(\delta\theta)$, to be projected onto the horizontal axes. This error propagates on the velocity and position in according to::

$$\begin{aligned} \delta v &= \hat{v} - v = \int \bar{a}\,dt - v = \int a\,dt + \int e_a\,dt + \int g e_g t\,dt - v \\ &= v + e_a t + \frac{1}{2} e_g g t^2 - v = e_a t + \frac{1}{2} e_g g t^2 \end{aligned} \tag{2.15}$$

$$\begin{aligned} \delta p &= \hat{p} - p = \int \hat{v}\,dt - p = \int e_a t\,dt + \int \frac{1}{2} e_g g t^2 dt - p \\ &= p + \frac{1}{2} e_a t^2 + \frac{1}{6} e_g g t^3 - p = \frac{1}{2} e_a t^2 + \frac{1}{6} e_g g t^3 \end{aligned} \tag{2.16}$$

Deterministic compensation is not sufficient to erase the error due to random white noise: in fact it introduces a zero-mean random walk error into the integrated signal, whose standard deviation grows proportionally to the square root of time:

$$\sigma_\theta(t) = \sigma\sqrt{t} \tag{2.17}$$

where σ is the standard deviation of the measurement signal and σ_θ is the growing standard deviation of the integrated signal. This quantity is also known as Angular Random Walk (ARW) [61].

Stochastic filters such as Extended Kalman Filter (EKF) [60, 12] can improve the estimation performances of INS algorithms.

The theory of Kalman Filter is suitable to implement to the sensor fusion strategy of the Aided Inertial Navigation System, which is conceptually described in Fig. 2.3.

This technique employs some additional source of navigation information, external from the inertial system, to improve the accuracy of the inertial navigation

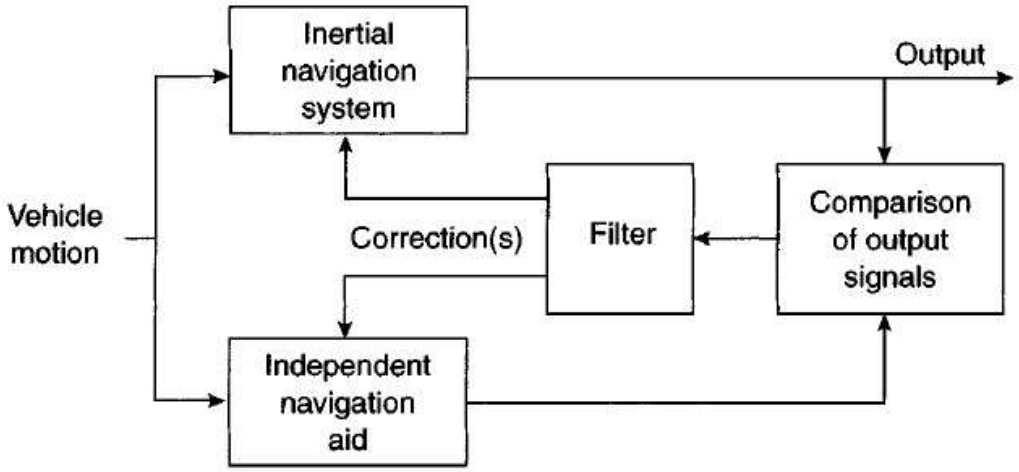

Figure 2.3: Basic principle of an integrated navigation system

system. An example is the integration between INS and GPS.

INS/GPS Sensor Fusion

A number of different integration architectures have been developed to allow INS and GPS to be combined, [57, 40]:

- *Uncoupled systems* in which GPS estimated position is simply used to reset the INS indicated position at regular intervals of time;
- *Loosely coupled systems* in which the INS and GPS estimates of position and velocity are compared, the resulting differences forming the measurement inputs to a Kalman filter;
- *Tightly coupled systems* in which the GPS measurements of pseudo-range and pseudo range rate are compared with estimates of these quantities generated by the inertial system;
- *Ultra-tightly coupled systems* which combine the GPS signal tracking function and the INS/GPS integration into a single algorithm.

In order to implement the coupled solutions, it is necessary to develop a linear dynamic model of the errors that are to be estimated. The error model may be expressed in matrix form as:

$$\delta \dot{x} = F \delta x + G w \tag{2.18}$$

The vector δx represents the error state of the system. Usually it consists of the three attitude errors ($\delta\psi$, $\delta\theta$, $\delta\phi$), three velocity errors δv^N, δv^E, δv^D and three position errors δp^N, δp^E, δp^D. F is the state matrix, G is the matrix which correlates the process noise (w) to the state. Refer to [40, 49] for the explicit form of these matrices.

The system of the error in the finite state form is:

$$\delta x(k+1) = \Phi(k)\delta x(k) + w(k) \tag{2.19}$$

where $\Phi(k)$ is the system transition matrix at time k, which may be expressed in terms of the system matrix F as follows:

$$\Phi(k) = e^{Fdt} \tag{2.20}$$

The error of velocity and position between the INS estimation and the GPS measurement is considered the observation vector of the Kalman Filter:

$$z(k) = \begin{bmatrix} p^n_{INS} - p^n_{GPS} \\ v^n_{INS} - v^n_{GPS} \end{bmatrix} \tag{2.21}$$

The conceptual schema of the aided navigation has been taken into account in the definition of the innovative localization algorithm for the railway scenario. At the same time the implementation of an error model has been evaluated a complex solution: in fact, as it will be clearer in the next section, the working scenario in the railway application is slightly simpler.

2.2 Sensor fusion between odometers and INS

In this section the architecture of the innovative localization algorithm is presented. A preliminary consideration has leaded to the omission of GPS. At a first analysis it seems that the GPS can solve the problem of the odometry estimate. However, since the availability of the GPS signal is not always guaranteed (for example in tunnels), it is necessary to consider alternative solutions.

Furthermore, even if the signal is present, for the particular application, it is not possible to exploit directly the information of position provided by the GPS: in fact it has already been pointed out as the performance requirement is reported as progressive distance traveled. The lack of the georeferentation information discourages the using of the GPS: in fact georeferentation of the track lines could be a possibility for an accurate estimation of the position. In this way odometry could

take advantage of Global Position Systems (GPS) to detect each point on the track as longitude, latitude and height and match it to the length of the line up to that point.

Also the magnetometer has been omitted from the final solution of the algorithm: in fact its benefit are more about a better estimation of the yaw angle. It has been evaluated that the effort to solve the problems associated with the filtering of this sensor are not rewarded by a real benefit in the performance of the localization algorithm.

Some preliminary numerical experiments have proved that INS itself, as already anticipated in Sect. 2.1.4, cannot provide the high accuracy required for velocity and position estimates. So,according to the directives of the sensor fusion techniques INS is *fused* with a tachometer in order to optimize the odometric estimation reliability.

The concept is to allow to integrate the measures from different sources trying to choose in every condition the sensor that has the maximum reliability and to identify and compensate the sensor measurement errors. Compared to previously introduced odometry algorithms [6, 27], the proposed algorithm can take advantage of the integration of the INS with a wheel angular speed sensor and the reset of the position estimation when a balise occurs along the track.

The following considerations leaded to the idea of separating the 3D attitude estimation with the 1D speed/travelled distance estimation:

- even though the relevant orientation angle is the pitch, since it is related to the line gradient estimate, the high nonlinearity of the relation between gyroscopes and euler angles makes necessary the estimation of all the euler angles (roll, pitch, yaw);
- ETCS requirements [55, 38, 39, 37] which are used to test the performances of odometry algorithms are based on the longitudinal speed error and the travelled distance error, so lateral and vertical displacements are not relevant;
- the comparison between the speed estimated by the integration of the accelerometer and the speed measured by the tachometer, and also the reset of the estimate of the travelled distance in correspondence of a balise, are simply and directly available.

It is worth to note that, for the aim of this work, the contribution of ω_{ie}^{n} and of ω_{en}^{n} is considered negligible, since it is much less than the signal coming from the movement, therefore:

$$\omega_{ib}^{b} = \omega_{nb}^{b} \tag{2.22}$$

The proposed algorithm is summarized by the block diagram in Fig. 2.4, where $\hat{R}_n^b$ represents the rotation matrix from *n-frame* (defined as the initial body frame of the vehicle) to *b-frame* and $\vec{g}$ is the gravitational vector.

Two Kalman Filters are implemented in this diagram:

- *Orientation Kalman Filter* estimates the orientation of the train from *b-frame* to *n-frame* in terms of Euler angles (roll, pitch, yaw), fusing the information of angular rate coming from the gyroscope with the wheel peripheral acceleration, derived from the tachometer;
- *INS-ODO Kalman Filter* estimates speed and travelled distance, fusing the gravity compensated body longitudinal acceleration with the wheel peripheral speed [12].

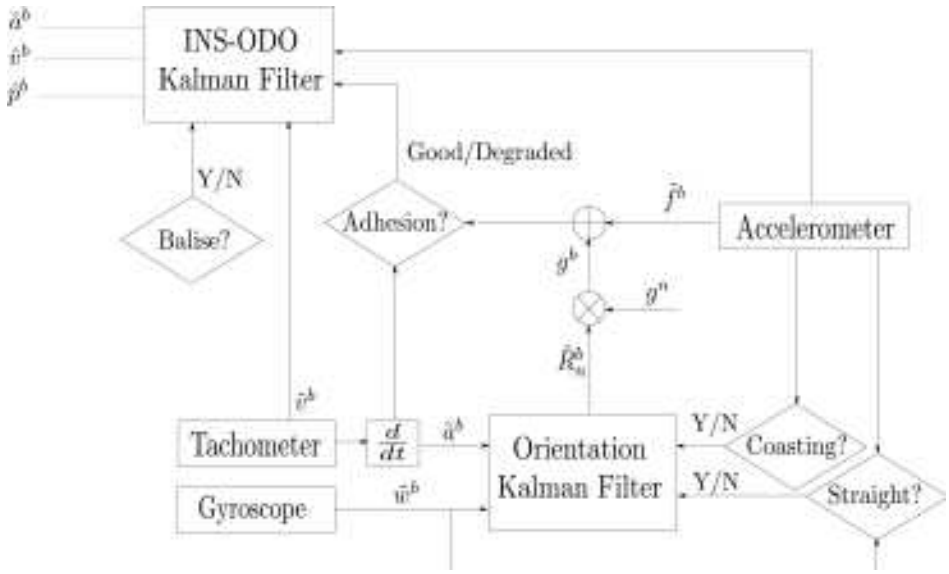

Figure 2.4: Block diagram of the localization algorithm

As shown in Fig. 2.4, the algorithm provides four *diamond* boxes, related to some relevant working conditions (Coasting, Straight, Adhesion, Balise). Their meaning will be explained in the Sect. 2.2.1 and 2.2.2.

2.2.1 Orientation Kalman Filter

The state equation of the Orientation Kalman Filter in block matrix form is:

$$\vec{x}_{Gi}(k+1) = F_{Gi}\vec{x}_{Gi}(k) \tag{2.23}$$

where $i = x,y,z$ and:

$$\begin{aligned}\vec{x}_{Gx} &= \left[\psi\ \dot{\psi}\right]^{\mathrm{T}}\\ \vec{x}_{Gy} &= \left[\theta\ \dot{\theta}\right]^{\mathrm{T}}\\ \vec{x}_{Gz} &= \left[\phi\ \dot{\phi}\right]^{\mathrm{T}}\end{aligned}$$

where: ψ, θ, and ϕ are respectively the roll, pitch and yaw angles , $\dot{\psi}$, $\dot{\theta}$, and $\dot{\phi}$ are their derivatives with respect to time, and the matrix F_G is defined as follows:

$$F_{Gi} = \begin{bmatrix} 1 & T_s \\ 0 & 1 \end{bmatrix} \tag{2.24}$$

with $i = x,y,z$, T_s is the sampling time (equal to 0.1 s, in accordance with the sampling time of the classical odometry algorithms).

Process noise covariance matrix Q_G is assumed as:

$$Q_G = \mathrm{diag}(Q_{Gx},Q_{Gy},Q_{Gz}), \quad Q_{Gi} = \begin{bmatrix} \frac{T_s^3}{3}\sigma_i^2 & \frac{T_s^2}{2}\sigma_i^2 \\ \frac{T_s^2}{2}\sigma_i^2 & T_s\sigma_i^2 \end{bmatrix} \tag{2.25}$$

with $i = x,y,z$; in this equation σ_i values represent the experimentally determined standard deviations of the components of the state vector.

The observation array is:

$$\vec{z}_G = \begin{bmatrix} \bar{\omega}_x^b \\ \bar{\omega}_y^b \\ \bar{\omega}_z^b \\ \bar{a}_x^b \\ 0 \end{bmatrix} \tag{2.26}$$

The first three components are the *b-frame* angular rates measured by the gyroscope; the fourth, instead, is the longitudinal component of the *b-frame* acceleration obtained by the finite derivatives (Euler backward method) of two subsequent tachometer measures:

$$\bar{a}_x^b(i) = \frac{\bar{v}_x^b(i) - \bar{v}_x^b(i-1)}{T_s} \tag{2.27}$$

where i is the time sample.

The last component is the zero value for the reset of the roll angle which can

occur in the particular condition of straight track.

The H_G matrix, which correlates observations with the state is:

$$H_G = \begin{bmatrix} 0 & 1 & 0 & 0 & 0 & -s\theta \\ 0 & 0 & 0 & c\psi & 0 & c\theta s\psi \\ 0 & 0 & 0 & -s\psi & 0 & c\theta c\psi \\ 0 & 0 & 0 & g_z & 0 & 0 \\ 1 & 0 & 0 & 0 & 0 & 0 \end{bmatrix} \tag{2.28}$$

where $s\theta = \sin(\theta)$ and $c\theta = \cos(\theta)$ and g_z = -9.81 m/s^2.

Since pitch angles are small, the following approximation can be assumed:

$$a_x = g_z \sin(\theta) \approx g_z \theta \tag{2.29}$$

Sensor noise covariance matrix R_G is assumed as:

$$R_G = \text{diag}(\sigma^2_{\omega_x}, \sigma^2_{\omega_y}, \sigma^2_{\omega_z}, \sigma^2_{a_b}, \sigma^2_0) \tag{2.30}$$

where the elements in the diagonal matrix are the standard deviations of sensor measures.

The R_G matrix is adaptive with respect to the conditions *Coasting* and *Straight* represented in the diamond boxes in Fig. 2.4.

The coasting is a phase where neither traction and braking occur. Since a movement caused only by the line gradient is compensated by the gravity term (Eq. 2.3), it can be said that the coasting phase is related to the fact that the longitudinal component of the accelerometer is close to "zero". In this case the wheel peripheral acceleration (Eq. 2.27) is substantially equal to the longitudinal acceleration, since in the coasting phases, phenomena of degraded adhesion does not have effect. In this way it is possible to retrieve a reliable estimate of the line gradient, through the inversion of the Eq. 2.29 (taken into account in the H_G matrix), from a source decoupled from the gyroscopes.

$$\begin{cases} \sigma^2_{\omega_y} >> \sigma^2_{a_b}, & \text{if } \left|\bar{f}^b_x\right| < \eta_{f_x} \\ \sigma^2_{\omega_y} << \sigma^2_{a_b}, & \text{otherwise} \end{cases} \tag{2.31}$$

The Eq. (2.31) explains how the Coasting phase is handled by the Orientation Kalman Filter. When "zero" longitudinal accelerations occur, sensor noise covari-

ance values ($\sigma^2_{\omega_y}$ and $\sigma^2_{a_b}$) are set so as to enable the contribution of the tachometer and disable the component y of the gyroscope.

The complementary case, instead, occurs when longitudinal component of the accelerometer is far from zero (traction and braking phases).

The Straight condition states the condition of reset of the roll angle: in fact, neglecting roll variations due to the suspensions, relevant values of this angle occur when the track is curvilinear in presence of *cant* angles.

The requirement of "zero" lateral acceleration is not sufficient to state the absence of curved track: in fact the compensation of the total lateral acceleration can subsist when the centrifugal acceleration, due to the train motion in curve, is compensated by the "gravity lateral acceleration", due to the presence of *cant* in the curves of a railway track. It is, thus, necessary to include conditions on the gyroscopes, that is "zero" angular rates over x and z axes:

$$\begin{cases} \sigma^2_{\omega_x} >> \sigma^2_0, & \text{if } \left(\left|\bar{f}^b_y\right| < \eta_{f_y} \;\&\; \left|\bar{\omega}^b_x\right| < \eta_{\omega_x} \;\&\; \left|\bar{\omega}^b_z\right| < \eta_{\omega_z}\right) \\ \sigma^2_{\omega_x} << \sigma^2_0, & \text{otherwise} \end{cases} \tag{2.32}$$

The condition (2.32) allows "turning on" the contribution of the roll reset when the three requirements explained ("zero" lateral acceleration, "zero" x and z angular rates) occur at the same time.

The thresholds $\eta_{f_x}, \eta_{f_y}, \eta_{\omega_x}, \eta_{\omega_z}$ have been experimentally tuned.

2.2.2 INS-ODO Kalman Filter

The state equations of the INS-ODO Kalman Filter, expressed in block matrix form, are:

$$\begin{bmatrix} p^b_x(k+1) \\ v^b_x(k+1) \\ a^b_x(k+1) \end{bmatrix} = \begin{bmatrix} 1 & T_s & \frac{1}{2}T_s^2 \\ 0 & 1 & T_s \\ 0 & 0 & 1 \end{bmatrix} \begin{bmatrix} p^b_x(k) \\ v^b_x(k) \\ a^b_x(k) \end{bmatrix} \tag{2.33}$$

where: p^b_x is the distance travelled by the train, v^b_x is the train speed, a^b_x is the *b-frame* acceleration.

The process noise covariance matrix Q_A is assumed as:

$$Q_A = \begin{bmatrix} \frac{T_s^5}{20}\sigma_a^2 & \frac{T_s^4}{8}\sigma_a^2 & \frac{T_s^3}{6}\sigma_a^2 \\ \frac{T_s^4}{8}\sigma_a^2 & \frac{T_s^3}{3}\sigma_a^2 & \frac{T_s^2}{2}\sigma_a^2 \\ \frac{T_s^3}{6}\sigma_a^2 & \frac{T_s^2}{2}\sigma_a^2 & T_s\sigma_a^2 \end{bmatrix} \tag{2.34}$$

where σ_a represents the experimentally determined standard deviation of the components of the state vector.

The observation array is:

$$\vec{z}_A = \begin{bmatrix} f_x^b - R_n^b g^n \\ v_x^b \\ 0 \end{bmatrix} \tag{2.35}$$

The first component is the compensated longitudinal gravity acceleration, the second is the speed of the train measured by the tachometer, the third is the zero point of the position reset sent by the balise, which is supposed to occur each 1000 m.

The H_a matrix, which correlates the observations with the state, is:

$$H_a = I_{3x3} \tag{2.36}$$

Sensor noise covariance matrix R_A is assumed as:

$$R_A = diag(\sigma_{a_x}^2, \sigma_{v_x}^2, \sigma_{p_x}^2) \tag{2.37}$$

where the elements in the diagonal are the standard deviation values of the sensor measures.

The R_A matrix is adaptive with respect to the conditions *Adhesion* and *Balise* represented in the diamond boxes in Fig. 2.4.

The Adhesion condition is determined through the condition reported in Eq. 2.38. The master criterion is the "accelerometric criterion": if the difference between the wheel peripheral acceleration (a_x^b) and the gravity compensated body longitudinal acceleration ($f_x^b - \hat{R}_n^b g$) is less than a threshold (η_{ad}), the adhesion is considered good. In order to avoid that "fake" good adhesion conditions are considered, a slave "tachometric criterion" has been implemented: it allows the speed reset only if the difference between the actual estimated speed ($\hat{v}^b$)and the wheel peripheral speed (v_x^b) is lower than a threshold (η_v). It is worth pointing out that, compared to the classical SCMT solutions, only one tachometer is sufficient for the detection of the wheel-rail adhesion condition.

$$\begin{cases} \sigma^2_{a_x} >> \sigma^2_{v_x}, & \text{if}\left(\left|f^b_x - \hat{R}^b_n g - a^b_x\right| < \eta_{ad} \;\&\; \left|\hat{v}^b - v^b_x\right| < \eta_v\right) \\ \sigma^2_{a_x} << \sigma^2_{v_x}, & \text{otherwise} \end{cases} \tag{2.38}$$

(2.38) states that, when good adhesion between the wheel and the rail occurs, the measurement update of the Kalman Filter can rely on the contribution of the speed measures provided by the tachometer. Moreover, although degraded adhesion conditions occur, the longitudinal acceleration signal provides anyway an estimate of speed and travelled distance.

The thresholds η_{ad}, η_v have been experimentally tuned in the testing phase.

The Balise condition (2.39) allows to reset the travelled distance estimate, recognizing the occurrence of a balise. During the operative conditions a logic signal reveals the presence of a balise. In a simulated scenario it has been hypothesized the occurrence of a balise every 1000 m, assuming a five meters bidirectional error (expressed by η_{ba}) on its positioning along the track. This value of uncertainty is obtained considering empirical knowhow about the tolerances linked to the balise positioning along the line.

$$\begin{cases} \sigma^2_{a_x} >> \sigma^2_{r_x}, & \text{if}\left|p^b_x - 1000\right| < \eta_{ba} \\ \sigma^2_{a_x} << \sigma^2_{r_x}, & \text{otherwise} \end{cases} \tag{2.39}$$

Chapter 3

Testing of the innovative localization algorithm in a simulated scenario

The testing procedure, sketched in Fig. 3.1, is described in detail in this section. The procedure is composed only of simulated tasks. It lets the algorithm to perform a first tuning and get results for a preliminary assessment of the strategy.

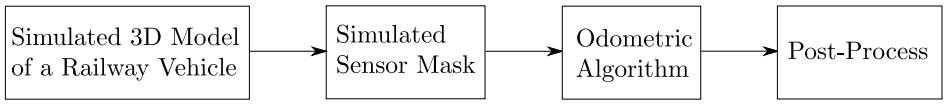

Figure 3.1: Testing procedure

3.1 Multibody model

The development and calibration of the odometric algorithm, described in Section 2.2, involves the availability of coherent kinematic inputs (wheel angular speed, acceleration and angular orientation) and the simulation of a wide range of working conditions, whose realization by means of experimental test runs is difficult and expensive.

On the other hand, for this type of application, the use of available multibody softwares is quite difficult, since the simulation of degraded adhesion conditions involves the co–simulation of on-board mechatronic devices, such as WSP, anti-skid, etc..

In order to overcome all these problems a complete 3D multibody model of a railway vehicle has been developed using Matlab-Simulink^{TM}, which is able to reproduce different working conditions, with arbitrary tracks, including ones which

may stress the sensors behaviour, in order to investigate their critical aspects [30, 7].

In particular the 3D multibody model of a high speed train was implemented. A single unit, composed of a coach connected to two bogies, was modelled. Using a multibody approach, the system is divided in one coach, two bogie frames, eight axle boxes, and four wheelsets. The coach is held by a rear and front bogie with a two-stage suspension system (Fig. 3.2). The railway vehicle has a B_0-B_0 wheel-and-axle set (each bogie has two mechanically independent engine axles).

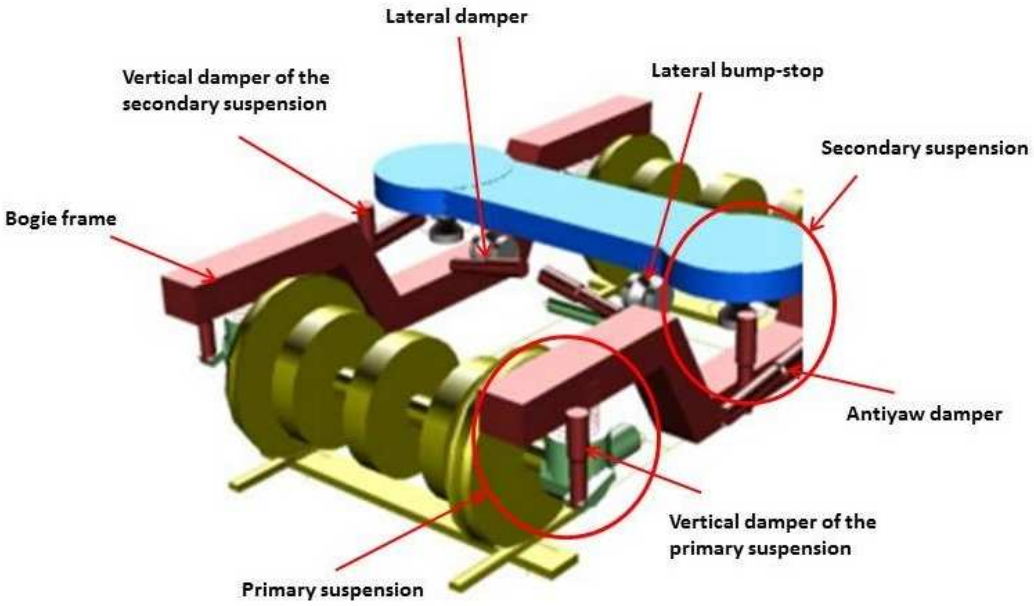

Figure 3.2: Two-stage suspension bogie model

The rail vehicle is provided with a double suspension stage (first and second stages in both vertical and lateral directions) between the coach, the bogies and the axles, damping devices (vertical, lateral, anti-yaw dampers) with non-linear characteristics, anti-roll bar and bump-stop plugs (to reduce the carbody roll motion, and other coach motions, respecting the vehicle loading gauge).

Force elements (e.g. the two suspension stages and the bump-stops) have been modelled by means of springs and dampers, with opportunely defined non-linear characteristics reproducing the real component behaviour (used data reproduce in a quite realistic way the typical properties of a high speed train).

In Tab. 3.1 the main properties of the rail vehicle are shown. In Tab. 3.2 the elastic characteristics of the connection elements are displayed.

Parameter	Units	Value
Total mass	[kg]	≈ 56000
Wheel-and-axle set	–	B_0-B_0
Bogie wheelbase	[m]	2.42
Bogie distance	[m]	16.9
Wheel diameter	[m]	0.92
Primary suspended masses own frequency	[Hz]	≈ 4.5
Secondary suspended masses (carbody) own frequency	[Hz]	≈ 0.8

Table 3.1: Main characteristics of the vehicle model

Element	Transl. Stiff. x [N/m]	Transl. Stiff. y [N/m]	Transl. Stiff. z [N/m]	Rotat. Stiff. x [Nm/rad]	Rotat. Stiff. y [Nm/rad]	Rotat. Stiff. z [Nm/rad]
Primary suspension	844000	844000	790000	10700	10700	0
Secondary suspension	124000	124000	340000	0	0	0
Axlebox bushing	40000000	6500000	40000000	45000	9700	45000
Anti roll bar	0	0	0	2506400	0	0

Table 3.2: Elastic characteristics of the two-stage suspension

Vertical and lateral damping devices assure a relatively high damping of the modes of vibration of the system: these elements are modelled with non-linear characteristics to reproduce the real behaviour. The wheel profile used for the simulations is the standard ISO ORE S1002, while the rail profile is an UIC60 with a 1/20 cant [15].

Concerning the motion resistance and the possible presence of the towed vehicles, the resistant contributions, such as the cushion friction and the aerodynamic resistance, have been considered, applying a longitudinal force to the center of the coach mass; the overall resistance is modelled according to a second order polynomial function of the longitudinal speed whose coefficients are estimated in accordance with the data available in literature [23, 59].

The simulated tests have the following characteristics:

- long time running: in order to have high INS integration errors;

- degraded adhesion: in order to stress tachometer measures;
- line gradient: it significantly affects the accelerometer error, see Eq. 2.29;
- curves and cant angles: a good estimation of the line gradient in the Attitude Kalman Filter is influenced by the good estimation of yaw and roll angles;
- patterns of irregularities of the rail line (rail gauge irregularities, cant, etc.).

In order to guarantee the robustness and the safety of the proposed solution the odometric algorithm has to be tested with a huge number of long paths, so that a strong computational effort is involved.

In order to avoid it, some basic modules with a great variability of features have been simulated. Then the required long paths have been created settling these basic modules the one with the other; in this way the computational effort is distributed on a limited set of short simulations.

3.2 Sensor mask

The accelerations and angular rates reproduced by the Matlab-Simulink^{TM} model have been processed by a mask which simulates the sensor errors described in Section 2.1.1 and 1.1.1.

3.2.1 IMU sensor mask

First of all, a short description of the sources of error which affect the IMU sensors is reported, referring to Eq. 2.4, [18].

Bias

The bias for an inertial sensor is defined as the average of the output over a specified time, measured at specified operating conditions that have no correlation with input acceleration or rotation [1]. The bias is typically expressed with the same unit of measure of the related quantity.

The bias is generally considered as having two parts, a deterministic bias offset (often termed as turn-on bias) and a bias-drift. Turn-on bias is the bias in the inertial sensor output, when the sensor is turned on. This bias part remains constant over a particular mission, and thus is deterministic through lab calibration procedures.

For low cost sensors such as the MEMS sensors, these errors are quite large and their repeatability is typically poor and thus, frequent calibration, which is every time the sensor is used, becomes a necessity.

The bias-drift refers to the rate at which the error in inertial sensor accumulates with time [13]. This part is random in nature, and thus has to be modelled stochastically.

Scale Factor

A scale factor is the ratio of a change in the output to a change in the input intended to be measured [1]. These errors are expressed in PPM. Typically these errors have been modeled as deterministic components.

Noise

Noise is an additional signal resulting from the sensor itself or other electronic equipment that interferes with the output signals being measured [13]. In general, noise is non-systematic and therefore cannot be removed from the data using deterministic models [22]. It can only be modeled by a stochastic process, where it is often considered as zero mean white Gaussian noise. As anticipated in Sect. 2.1.4 the error which arise in gyro and accelerometer measurements due to white noise is termed as angular/velocity random walk.

Assembly error

This error is not intrinsic in the nature of a MEMS sensor, but it comes out from a not aligned assembly of the device with respect to the gravity. Usually, in order to avoid a displacement in the attitude estimation, an initial alignment procedure is is obtained by *accelerometer levelling*, which uses knowledge of gravity sensed by each accelerometer, under static conditions:

$$\psi = \sin^{-1}\left(\frac{f_y^b}{g}\right)$$
$$\theta = -\sin^{-1}\left(\frac{f_x^b}{g}\right)$$

An initial estimate of the yaw could be determined by *gyro compassing*, which uses knowledge of the Earth rotation rate sensed by each gyro, under static conditions. This method is not feasible with low cost IMUs, since their gyro biases (turn-

on bias and drifts) and noise typically exceeds the Earth rotation rate. A potential source for such heading information is a magnetometer, which provides heading information by sensing the surrounding magnetic field, or to perform dynamic heading alignment using GPS velocities.

Assumptions for the IMU sensor mask

About the values to associate to each source of error in the simulated sensor mask, the following assumptions have been made:

- the random noise has been simulated, both for accelerometer and for gyroscope, as a Gaussian white noise with zero mean and standard deviation, η_a and η_g, as in Tab. 3.3;
- deterministic biases have not been simulated, since they are supposed to be removed during the calibration phase;
- random biases, b_a and b_g, have been simulated with the value in Tab. 3.3;
- scale factor errors have not been simulated, since they do not influence the results;
- a two degrees assembly error has been simulated for each Euler angle. This value has been obtained from the experience of the manufacturers. This error could be removed for roll and pitch angles through an initial gravity calibration. The inaccuracy which persists after this procedure has been simulated with a zero-mean Gaussian noise with standard deviation η_m, as in Tab. 3.3.

Parameter	Units	Value
η_a	m/s^2	2.2e-3
η_g	rad/s	7.8e-4
b_a	m/s^2	4.1e-3
b_g	rad/s	2.5e-5
η_m	rad	2.2e-4

Table 3.3: Errors of sensors - IMU

The values η_a, b_a and η_g, b_g are obtained, respectively, from the data sheet of a commercial accelerometer and the data sheet of a commercial gyroscope.

3.2.2 Tachometer sensor mask

The more relevant error sources have been added to the wheel angular velocity value (ω), get as output of the 3D multibody model. It is worth to not that, for these sensors, the most relevant source error derives from the losses of adhesion, which is a phenomenon just taken into account in the mathematical model.

For first, in order to simulate the influence of the quantization of the measure on the accuracy, the pulse counter $c(k)$ of the tachometer have been simulated:

$$\begin{aligned} \theta(k) &= \theta(k-1)+\omega(k)dt \\ c(k) &= \left\lceil \frac{\theta(k)N\text{res}}{2\pi} \right\rceil \end{aligned}$$

where N is the number of the teeth (N=80), res is the resolution (if the reading pulses are both on the rising and falling edge and phased by $\frac{\pi}{2}$, res=4)

Then the wheel angular speed has been retrieved by the pulse counter as effectively performed by the tachometer itself:

$$\bar{\omega}(k)=\left(\frac{c(k)-c(k-1)}{dt}\right)\frac{2\pi}{N\text{res}} \tag{3.1}$$

It is then assumed that mechanical and electronic errors are added to the angular displacement (θ) performed by the tachometer:

$$\bar{\theta}(k)=\theta(k)+\chi(k)+\sigma_\theta(k) \tag{3.2}$$

where χ(k) is the error due to eccentricity of the wheels, i.e. the not perfect alignment that exists between the center of rotation of the wheel and the center of rotation of the tachometer. This imperfection, often due to a mounting error, induces a reading error of the angle that can be formulated as:

$$\chi(k)=\sin^{-1}\left(\frac{e}{r}\sin(\omega t)\right) \tag{3.3}$$

where e is the eccentricity and r is the radius of the wheel.

Through the white noise with zero mean and standard deviation σ_θ are considered other sources of errors such as [31]:

- *Cycle error*: the term Cycle indicates the amount of rotation effected between two rising edges of the encoder signal; the Cycle error indicates the differ-

ence between the angle observed that gives rise to an electrical degree and the nominal angular increment;

- *Pulse width error*: deviation of the pulse amplitude compared the nominal π;
- *Phase error*: deviation of the phase of the channel compared to the nominal $\frac{\pi}{2}$;
- *Jitter*: deviation in amplitude of the square wave channels.

Since the wheel peripheral speed is obtained by multiplicating the wheel angular one with the radius, the slow variation of the dimension of radius, due to wear of the ferrous material, has been modeled:

$$r_{real} = r_{ideal} - \epsilon_r t \tag{3.4}$$

where $0 < \epsilon_r \ll 1$.

Assumptions for the Tachometer sensor mask

The Tab. 3.4 summarizes the values for each parameter explained previously. The data come from the features of the tachometers (N, res), the experience of the manifacturers (e, ϵ_r) and the feature of the train (r). The contribution of the white noise has been considered negligible and has not been modelled.

Parameter	Units	Value
N	-	80
res	-	4
e	m	0.04e-3
r	m	0.46
ϵ_r	m/s	0.0000006

Table 3.4: Errors of sensors - tachometer

3.3 Post-Process and evaluation of the performances of the algorithm

Since the inertial sensors are affected by stochastic noise, the efficiency of the algorithm cannot be evaluated analytically. Monte Carlo runs are made to obtain an estimation of the expected value of the performance from a sample average of

independent realizations [8]. A large number of runs increases the power of the hypothesis testing. The performance estimation related to N independent runs is the mean of the N cost values:

$$\overline{C} = \frac{1}{N}\sum_{i=1}^{N} C_i \tag{3.5}$$

where the *i-th* cost value C_i is the error between the true and the estimated travelled distance ($\tilde{p}_x^b = p_x^b - \hat{p}_x^b$) or speed ($\tilde{v}_x^b = v_x^b - \hat{v}_x^b$).

The mean error between true and estimated speed (or travelled distance) can be compared with the same cost obtained with the SCMT algorithm, described in paragraph 1.1. In order to evaluate the advantages of the localization algorithm in terms of reliability, it is possible to evaluate the percentage of time the signal error does not meet the requirements shown in Fig. 3.3, 3.4 where the blue line identifies the ETCS requirements described in [55, 38, 39, 37]. Since, as will be detailed in the following section, the proposed localization algorithm allows to obtain speed and travelled distance errors much lower than the values imposed by the ETCS requirements, the obtained results are compared with error limits stricter than the ETCS values, equal respectively to one half, one fourth and one eight of the ETCS limit. These reduced performance thresholds are shown in Fig. 3.3, 3.4.

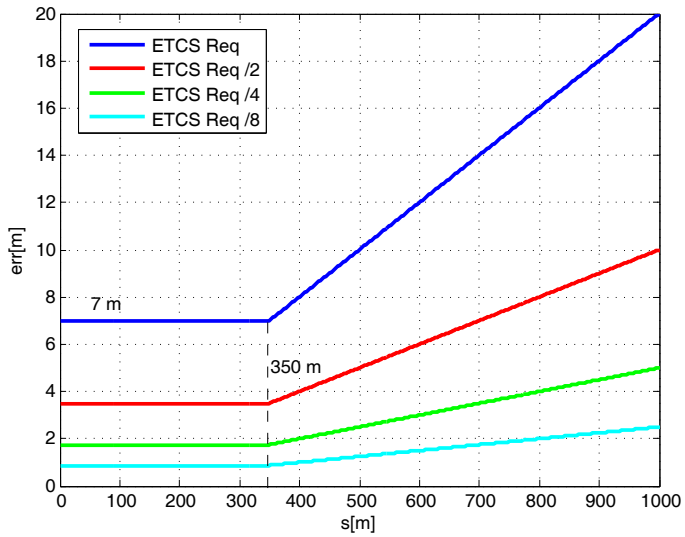

Figure 3.3: ETCS requirements - Travelled Distance: reference values (blue line), and reduced values

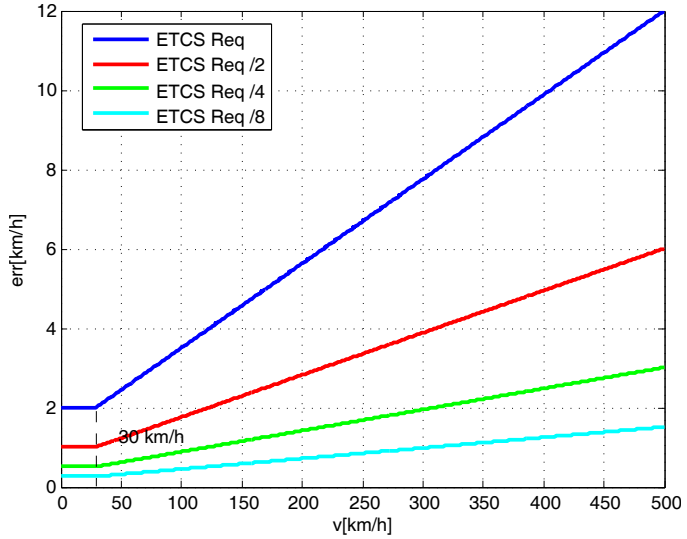

Figure 3.4: ETCS requirements - Speed: reference values (blue line), and reduced values

3.4 MonteCarlo simulation results

The testing procedure has been applied to ten worst-case-design paths, whose features are summarized in Tab. 3.5, 3.6, 3.7 and 3.8. Every path is compound of three phases of traction and braking, affected by degraded adhesion and interspersed by a phase of coasting. As concerns the adhesion, the railway paths have some sections characterized by good adhesion conditions, with a static adhesion coefficient equal to 0.3 (no slidings between the wheel and the rail), and some sections under degraded adhesion conditions, with a static adhesion coefficient equal to 0.1 (slidings between the wheel and the rail occur).

A degree of weakness (high or very high) is assigned to each testing path, in relation to the features which highlight the weaknesses of the sensors. The first five are characterized by a high degree of weakness, since the changes of slopes and the curves are faced at a such speed that the angular rates are greater than the noise of the gyroscope. The last five paths are characterized by a very high degree of weakness, since the high level of stress imposed to the sensors.

ID	Degree of Weakness	Characteristics
1	High	Articulated altimetry, with uphills and downhills up to 30 ‰, without any curves
2	High	Curved track with a radius of curvature of 1800 m, but level (there are no uphills or downhills)
3	High	Combination of curves (radius of curvature of 1800 m) and slopes (uphills and downhills up to 30 ‰)
4	High	Curves (radius of curvature of 1800 m) and uphills (downhills) with mixed slopes (10, 20, 20 ‰)
5	High	Very similar to the previous ones, but the curves are faced at a such speed and with a radius of curvature that the lateral acceleration is zero (testing of the weakness of the roll reset)
6	Very High	Very long (nearly 30 km) with slopes in the coasting phase, too
7	Very High	The first uphill, with slope of 30 ‰, is faced at a speed of about 15 km/h (testing if the gyroscope can read the angular rates over y axis)
8	Very High	The first uphill, with slope of 10 ‰, is faced at a speed of 35 km/h (same objective of the previous)
9	Very High	Very similar to the seventh, but the facing speed is about 8 km/h
10	Very High	The first curve (radius of curvature of 10000 m) is faced at speeds below 40 km/h (testing if the gyroscope can read the angular rates over z axis)

Table 3.5: Testing paths: characteristics

ID	Length km	% of Deg. Adhesion	% of Speed $v < v_1$	% of Speed $v_1 < v < v_2$	% of Speed $v > v_2$
1	20.91	40.14	7.28	51.56	41.15
2	20.71	41.84	7.15	50.48	42.36
3	20.63	49.51	7.24	47.92	44.84
4	26.59	40.25	6.61	49.16	44.23
5	31.40	33.07	4.92	52.48	42.60
6	36.76	43.59	4.22	51.87	43.91
7	21.31	39.26	8.85	50.40	40.76
8	21.03	39.70	8.22	49.88	41.89
9	21.31	39.27	9.28	50.21	40.52
10	21.16	42.63	7.99	48.60	43.41

Table 3.6: Testing paths: length, percentage of degraded adhesion and distribution of speed (v_1=50 km/h, v_2=150 km/h)

ID	% of Yaw Rate $\dot{\phi} < \dot{\phi}_1$	% of Yaw Rate $\dot{\phi}_1 < \dot{\phi} < \dot{\phi}_2$	% of Yaw Rate $\dot{\phi} > \dot{\phi}_2$
1	100	0	0
2	71.18	5.36	23.46
3	71.86	5.21	22.94
4	73.48	4.39	22.13
5	57.12	6.48	36.40
6	72.13	5.14	22.74
7	100	0	0
8	100	0	0
9	100	0	0
10	71.52	13.28	15.20

Table 3.7: Testing paths: distribution of curved track ($\dot{\phi}_1$=1e-4 rad/s, $\dot{\phi}_2$=0.005 rad/s)

ID	% of Slopes $\theta < 5$ ‰	% of Slopes $5 < \theta < 15$ ‰	% of Slopes $\theta > 15$ ‰
1	86.96	1.37	11.67
2	100	0	0
3	73.10	2.46	24.45
4	84.22	3.21	12.58
5	83.85	4.66	11.49
6	62.91	6.95	30.15
7	83.75	2.01	14.23
8	85.82	8.15	6.03
9	82.92	2.04	15.04
10	81.07	1.74	17.19

Table 3.8: Testing paths: distribution of sloped track

The histograms in Fig. 3.5 summarize the performance parameter explained in Sect. 3.3, where the mean errors of speed and travelled distance are obtained after 100 Monte Carlo runs. The results are subdivided in four sets: one with performances of speed estimation for paths with high degree of weakness (Fig. 3.5a), one with performances of travelled distance estimation for paths with high degree of weakness (Fig. 3.5c), one with performances of speed estimation for paths with very high degree of weakness (Fig. 3.5b) and the last with performances of travelled distance estimation for paths with very high degree of weakness (Fig. 3.5d). Each figure shows, on the first planar axis, the requirement used (ETCS or its sub-

divisions), on the second planar axis, the ID of the path and, on the vertical axis, the value of the calculated performance parameter. Since the results for SCMT algorithm (blue histograms) are significant just considering the ETCS requirements, the comparison with its subdivisions has been performed only for INS/ODO algorithm (green histograms).

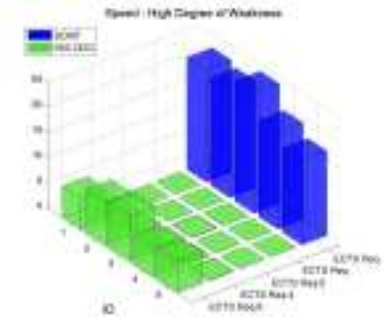

(a) Speed - High Degree of Weakness

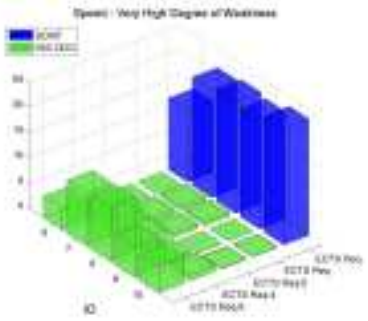

(b) Travelled distance - High Degree of Weakness

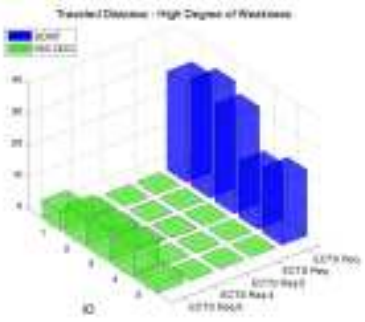

(c) Speed - Very High Degree of Weakness

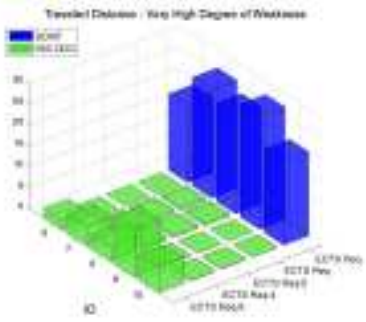

(d) Travelled distance - Very High Degree of Weakness

Figure 3.5: Percentage of time error does not meet ETCS requirements

The histograms point out some relevant results: the INS/ODO has sensibly better performances compared to SCMT algorithms. The requirements should be kept to one eight of the ETCS limit, in order to appreciate a significant error of estimate. The worst results involve paths # 7 and # 8, since even with respect to ETCS requirement, the speed and travelled distance errors are different from zero (i.e. the limit thresholds are overcome).

3.4.1 Description and results of each testing path

The results for each test path evidence that the localization algorithm performances are good, since the speed and the position estimation errors are always much smaller than the speed and position ETCS requirement thresholds.

Path #1

ID	Adhesion	Maneuver	WSP Anti-Skid	Curves	Altimetry	Irregularities
1	Degraded	Traction (0-200 km/h)	On	Straight	Uphill (3 %)	Regular
2	Degraded	Coasting (200 km/h)	On	Straight	Level	Regular
3	Degraded	Braking (200-100 km/h)	On	Straight	Uphill (3 %)	Regular
4	Degraded	Coasting (100 km/h)	On	Straight	Level	Regular
5	Degraded	Traction (100-200 km/h)	On	Straight	Uphill (3 %)	Regular
6	Degraded	Coasting (200 km/h)	On	Straight	Level	Regular
7	Degraded	Braking (200-100 km/h)	On	Straight	Downhill (3 %)	Regular
8	Degraded	Coasting (100 km/h)	On	Straight	Level	Regular
9	Degraded	Traction (100-200 km/h)	On	Straight	Level	Regular
10	Degraded	Coasting (200 km/h)	On	Straight	Level	Regular
11	Degraded	Braking (200-0 km/h)	On	Straight	Downhill (3 %)	Regular

Table 3.9: Features of the test runs of Path #1

To be short, only for path # 1 is reported the graph with the comparison between the true speed of the train and the speed estimated by SCMT and INS/ODO algorithms (Fig. 3.6), with a zoom on the traction phase and on the braking phase (Fig. 3.7) which highlights the accuracy improvement of the innovative solution.

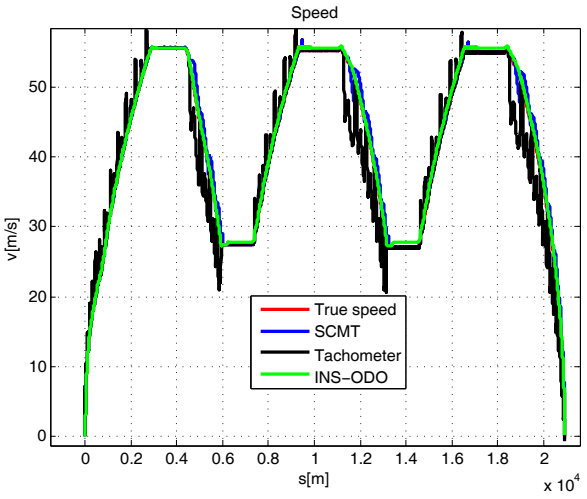

Figure 3.6: Comparison between true and estimated speed

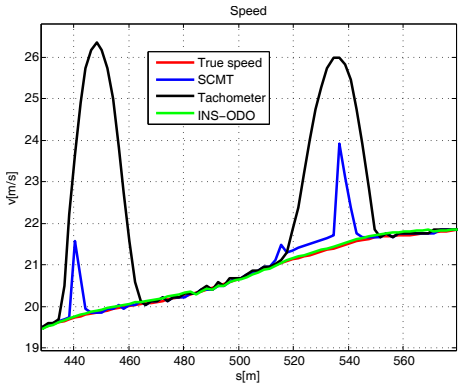

(a) Traction phase

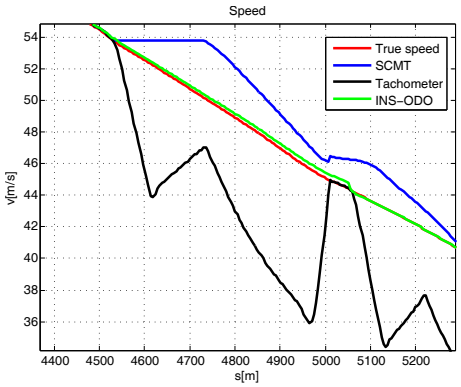

(b) Braking phase

Figure 3.7: Comparison between true and estimated speed - particulars

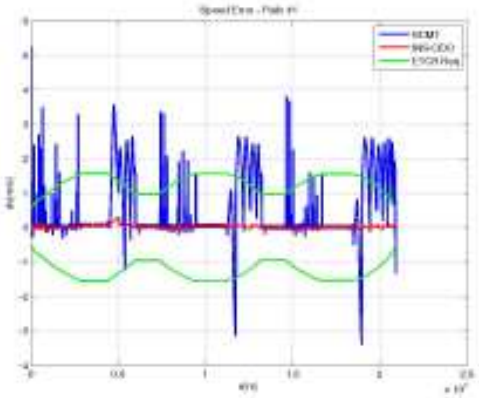

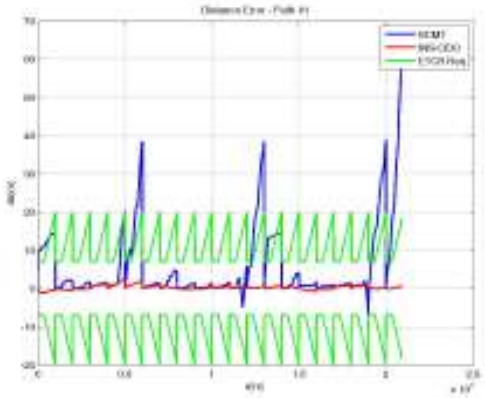

Figure 3.8: Simulated results for Path #1

Path #2

ID	Adhesion	Maneuver	WSP Anti-Skid	Curves	Altimetry	Irregularities
1	Degraded	Traction (0-200 km/h)	On	Curve	Level	Regular
2	Degraded	Coasting (200 km/h)	On	Curve	Level	Regular
3	Degraded	Braking (200-100 km/h)	On	Curve	Level	Regular
4	Degraded	Coasting (100 km/h)	On	Straight	Level	Regular
5	Degraded	Traction (100-200 km/h)	On	Straight	Level	Regular
6	Degraded	Coasting (200 km/h)	On	Curve	Level	Regular
7	Degraded	Braking (200-100 km/h)	On	Curve	Level	Regular
8	Degraded	Coasting (100 km/h)	On	Straight	Level	Regular
9	Degraded	Traction (100-200 km/h)	On	Straight	Level	Regular
10	Degraded	Coasting (200 km/h)	On	Curve	Level	Regular
11	Degraded	Braking (200-0 km/h)	On	Curve	Level	Regular

Table 3.10: Features of the test runs of Path #2

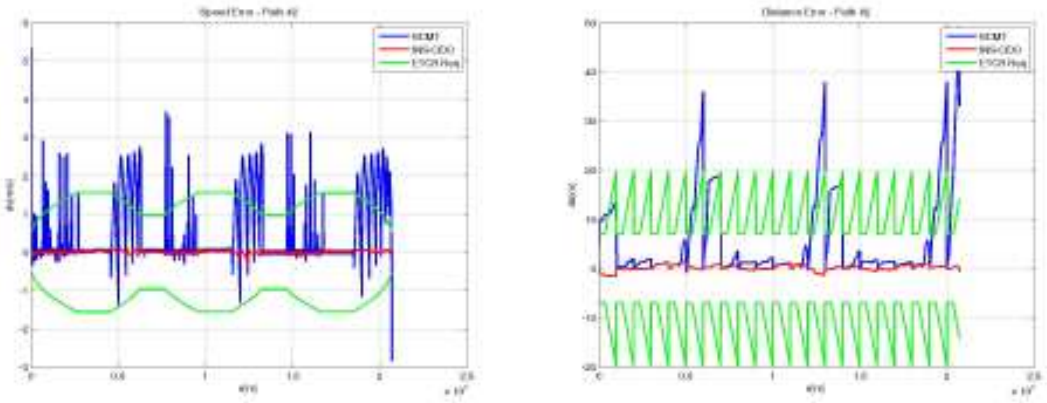

Figure 3.9: Simulated results for Path #2

Path #3

ID	Adhesion	Maneuver	WSP Anti-Skid	Curves	Altimetry	Irregularities
1	Degraded	Traction (0-200 km/h)	On	Curve	Downhill (3 %)	Regular
2	Degraded	Coasting (200 km/h)	On	Curve	Level	Regular
3	Degraded	Braking (200-100 km/h)	On	Curve	Uphill (3 %)	Regular
4	Degraded	Coasting (100 km/h)	On	Straight	Level	Regular
5	Degraded	Traction (100-200 km/h)	On	Straight	Downhill (3 %)	Regular
6	Degraded	Coasting (200 km/h)	On	Curve	Level	Regular
7	Degraded	Braking (200-100 km/h)	On	Curve	Downhill (3 %)	Regular
8	Degraded	Coasting (100 km/h)	On	Straight	Level	Regular
9	Degraded	Traction (100-200 km/h)	On	Straight	Uphill (3 %)	Regular
10	Degraded	Coasting (200 km/h)	On	Curve	Level	Regular
11	Degraded	Braking (200-0 km/h)	On	Curve	Downhill (3 %)	Regular

Table 3.11: Features of the test runs of Path #3

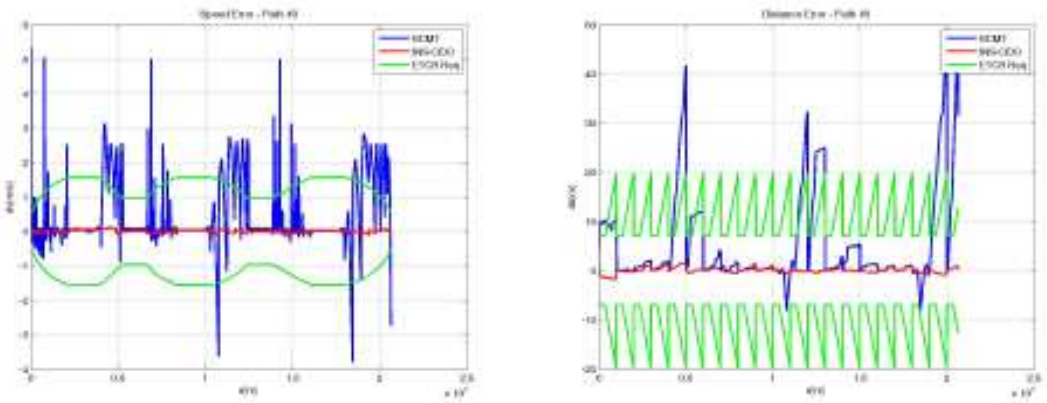

Figure 3.10: Simulated results for Path #3

Path #4

ID	Adhesion	Maneuver	WSP Anti-Skid	Curves	Altimetry	Irregularities
1	Degraded	Traction (0-200 km/h)	On	Straight	Uphill (2 %)	Regular
2	Degraded	Coasting (200 km/h)	On	Curve	Level	Regular
3	Degraded	Braking (200-100 km/h)	On	Curve	Downhill (3 %)	Regular
4	Degraded	Coasting (100 km/h)	On	Straight	Level	Regular
5	Degraded	Traction (100-200 km/h)	On	Straight	Uphill (3 %)	Regular
6	Degraded	Coasting (200 km/h)	On	Curve	Level	Regular
7	Degraded	Braking (200-100 km/h)	On	Straight	Downhill (1 %)	Regular
8	Degraded	Coasting (100 km/h)	On	Curve	Level	Regular
9	Degraded	Traction (100-200 km/h)	On	Straight	Level	Regular
10	Degraded	Coasting (200 km/h)	On	Curve	Level	Regular
11	Degraded	Braking (200-0 km/h)	On	Curve	Downhill (3 %)	Regular

Table 3.12: Features of the test runs of Path #4

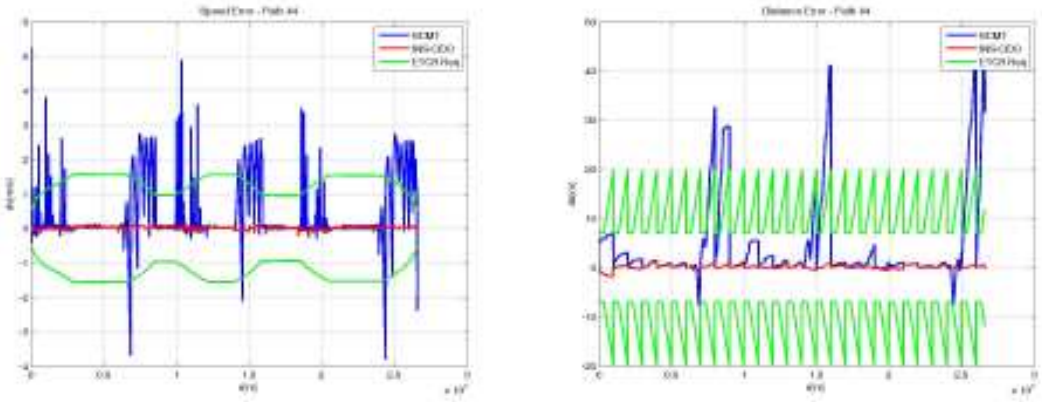

Figure 3.11: Simulated results for Path #4

Path #5

ID	Adhesion	Maneuver	WSP Anti-Skid	Curves	Altimetry	Irregularities
1	Degraded	Traction (0-200 km/h)	On	Straight	Uphill (3 %)	Regular
2	Degraded	Coasting (200 km/h)	On	Curve	Level	Regular
3	Degraded	Braking (200-100 km/h)	On	Straight	Downhill (1 %)	Regular
4	Degraded	Coasting (100 km/h)	On	Curve	Level	Regular
5	Degraded	Traction (100-200 km/h)	On	Straight	Uphill (1 %)	Regular
6	Degraded	Coasting (200 km/h)	On	Curve	Level	Regular
7	Degraded	Braking (200-100 km/h)	On	Curve	Downhill (3 %)	Regular

Table 3.13: Features of the test runs of Path #5

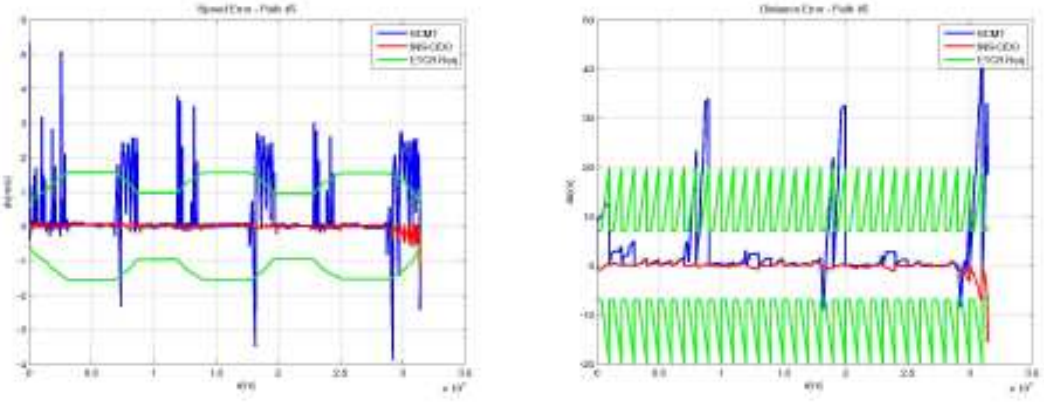

Figure 3.12: Simulated results for Path #5

Path #6

ID	Adhesion	Maneuver	WSP Anti-Skid	Curves	Altimetry	Irregularities
1	Degraded	Traction (0-200 km/h)	On	Curve	Uphill (3 %)	Regular
2	Degraded	Coasting (200 km/h)	On	Curve	Level	Regular
3	Degraded	Coasting (200 km/h)	On	Curve	Uphill (1 %)	Regular
4	Degraded	Braking (200-100 km/h)	On	Straight	Level	Regular
5	Degraded	Coasting (100 km/h)	On	Straight	Level	Regular
6	Degraded	Coasting (100 km/h)	On	Curve	Downhill (2 %)	Regular
7	Degraded	Traction (100-200 km/h)	On	Straight	Level	Regular
8	Degraded	Coasting (200 km/h)	On	Curve	Level	Regular
9	Degraded	Braking (200-0 km/h)	On	Curve	Downhill (3 %)	Regular

Table 3.14: Features of the test runs of Path #6

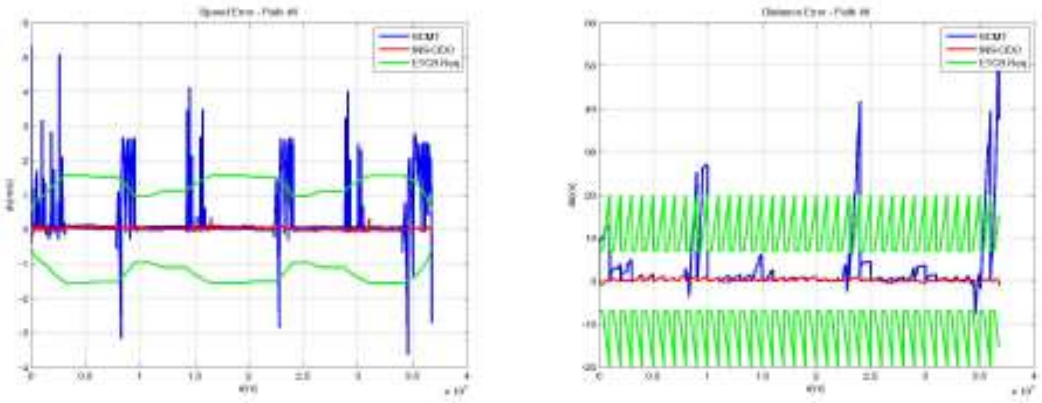

Figure 3.13: Simulated results for Path #6

Path #7

ID	Adhesion	Maneuver	WSP Anti-Skid	Curves	Altimetry	Irregularities
1	Degraded	Traction (0-200 km/h)	On	Straight	Uphill (3 %)	Regular
2	Degraded	Coasting (200 km/h)	On	Straight	Level	Regular
3	Degraded	Braking (200-100 km/h)	On	Straight	Uphill (3 %)	Regular
4	Degraded	Coasting (100 km/h)	On	Straight	Level	Regular
5	Degraded	Traction (100-200 km/h)	On	Straight	Level	Regular
6	Degraded	Coasting (200 km/h)	On	Straight	Level	Regular
7	Degraded	Braking (200-100 km/h)	On	Straight	Downhill (3 %)	Regular
8	Degraded	Coasting (100 km/h)	On	Straight	Level	Regular
9	Degraded	Traction (100-200 km/h)	On	Straight	Level	Regular
10	Degraded	Coasting (200 km/h)	On	Straight	Level	Regular
11	Degraded	Braking (200-0 km/h)	On	Straight	Downhill (3 %)	Regular

Table 3.15: Features of the test runs of Path #7

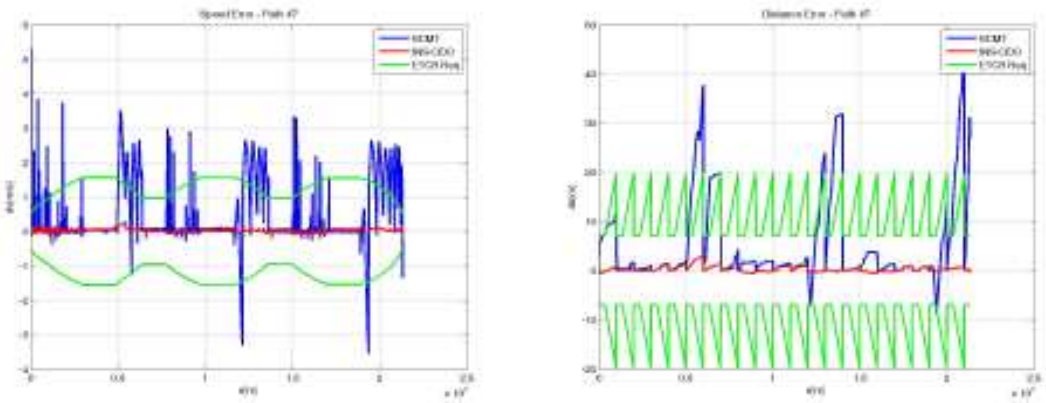

Figure 3.14: Simulated results for Path #7

Path #8

ID	Adhesion	Maneuver	WSP Anti-Skid	Curves	Altimetry	Irregularities
1	Degraded	Traction (0-200 km/h)	On	Straight	Uphill (1 %)	Regular
2	Degraded	Coasting (200 km/h)	On	Straight	Level	Regular
3	Degraded	Braking (200-100 km/h)	On	Straight	Uphill (3 %)	Regular
4	Degraded	Coasting (100 km/h)	On	Straight	Level	Regular
5	Degraded	Traction (100-200 km/h)	On	Straight	Level	Regular
6	Degraded	Coasting (200 km/h)	On	Straight	Level	Regular
7	Degraded	Braking (200-100 km/h)	On	Straight	Downhill (3 %)	Regular
8	Degraded	Coasting (100 km/h)	On	Straight	Level	Regular
9	Degraded	Traction (100-200 km/h)	On	Straight	Level	Regular
10	Degraded	Coasting (200 km/h)	On	Straight	Level	Regular
11	Degraded	Braking (200-0 km/h)	On	Straight	Downhill (3 %)	Regular

Table 3.16: Features of the test runs of Path #8

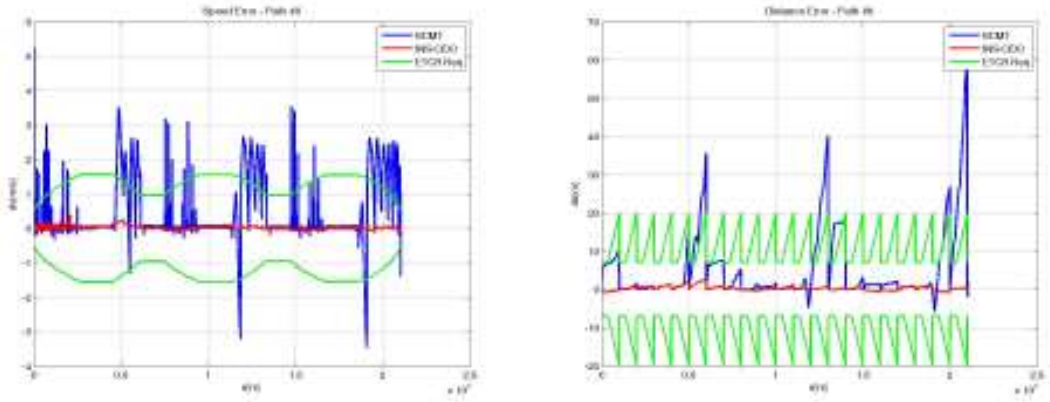

Figure 3.15: Simulated results for Path #8

Path #9

ID	Adhesion	Maneuver	WSP Anti-Skid	Curves	Altimetry	Irregularities
1	Degraded	Traction (0-200 km/h)	On	Straight	Uphill (3 %)	Regular
2	Degraded	Coasting (200 km/h)	On	Straight	Level	Regular
3	Degraded	Braking (200-100 km/h)	On	Straight	Uphill (3 %)	Regular
4	Degraded	Coasting (100 km/h)	On	Straight	Level	Regular
5	Degraded	Traction (100-200 km/h)	On	Straight	Level	Regular
6	Degraded	Coasting (200 km/h)	On	Straight	Level	Regular
7	Degraded	Braking (200-100 km/h)	On	Straight	Downhill (3 %)	Regular
8	Degraded	Coasting (100 km/h)	On	Straight	Level	Regular
9	Degraded	Traction (100-200 km/h)	On	Straight	Level	Regular
10	Degraded	Coasting (200 km/h)	On	Straight	Level	Regular
11	Degraded	Braking (200-0 km/h)	On	Straight	Downhill (3 %)	Regular

Table 3.17: Features of the test runs of Path #9

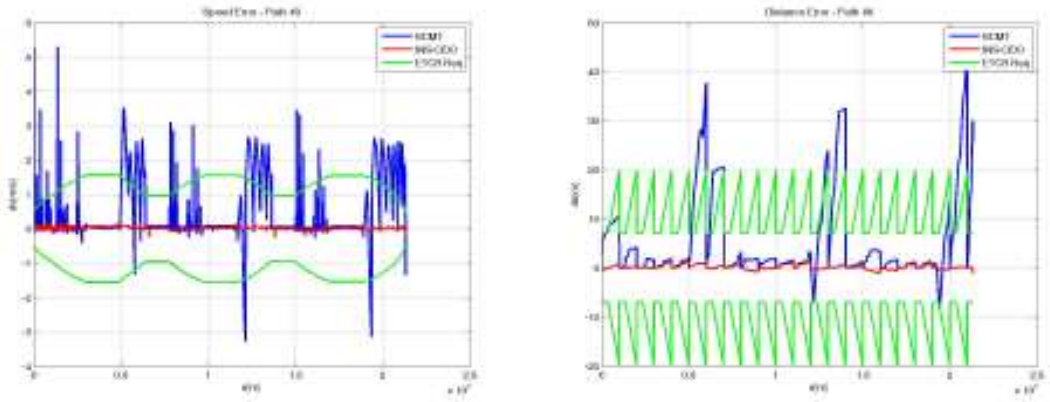

Figure 3.16: Simulated results for Path #9

Path #10

ID	Adhesion	Maneuver	WSP Anti-Skid	Curves	Altimetry	Irregularities
1	Degraded	Traction (0-200 km/h)	On	Curve	Level	Regular
2	Degraded	Coasting (200 km/h)	On	Curve	Level	Regular
3	Degraded	Braking (200-100 km/h)	On	Curve	Uphill (3 %)	Regular
4	Degraded	Coasting (100 km/h)	On	Straight	Level	Regular
5	Degraded	Traction (100-200 km/h)	On	Straight	Downhill (3 %)	Regular
6	Degraded	Coasting (200 km/h)	On	Curve	Level	Regular
7	Degraded	Braking (200-100 km/h)	On	Curve	Downhill (3 %)	Regular
8	Degraded	Coasting (100 km/h)	On	Straight	Level	Regular
9	Degraded	Traction (100-200 km/h)	On	Straight	Uphill (3 %)	Regular
10	Degraded	Coasting (200 km/h)	On	Curve	Level	Regular
11	Degraded	Braking (200-0 km/h)	On	Curve	Downhill (3 %)	Regular

Table 3.18: Features of the test runs of Path #10

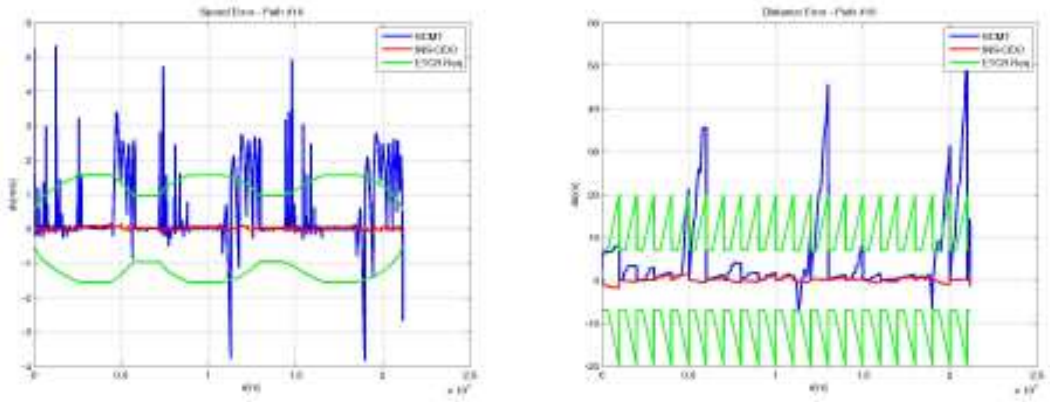

Figure 3.17: Simulated results for Path #10

Chapter 4

Design of a Dynamic Simulator for the testing of inertial sensors

Dynamic simulators are very powerful devices which allow inducing the dynamic effects of a system, creating the feelings of being in a moving vehicle: through flight or drive simulators, for example, a pilot can interact with the vehicle in realistic scenarios.

Motion simulators have been experiencing a strong growth since 60s and 70s with application for a large number of vehicles, including cars, motorcycles and trains.

A dynamic simulator (see Fig. 4.1) is essentially composed of a mathematical Dynamic Model (DM) which is simulated (usually in real-time), software components, called Washout Filters (WF) [35, 19, 20, 16, 43], with the aim of making the simulation realistic, and hardware devices such as parallel robots (Stewart Platforms) or serial manipulators, aimed to reproduce the motion in a limited workspace.

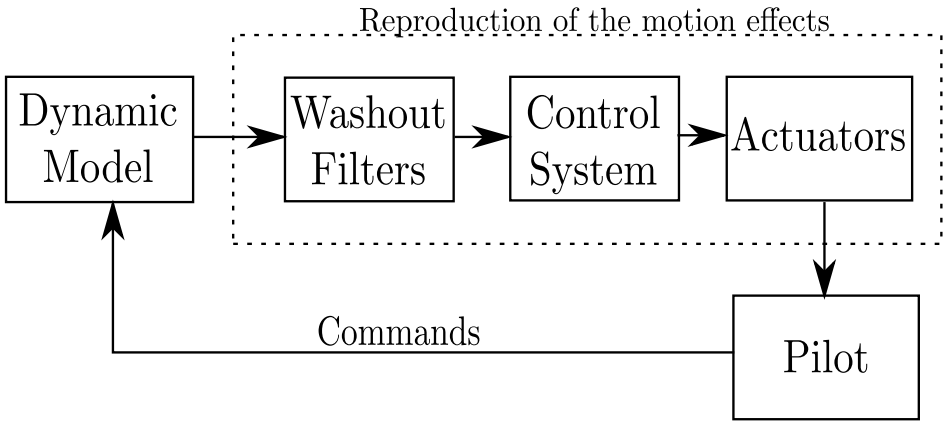

Figure 4.1: Dynamic simulator

A different application of dynamic simulators is described in this thesis, regarding the reproduction of the motion dynamic effects of a railway vehicle on inertial sensors for the testing of the innovative localization system based on the integration of odometers and an IMU, described in Sect. 2.2. The result of the project will be an industrial product to be used in Automatic Train Protection and Control (ATP/ATC) systems: in fact the IMU has been expressly designed and realized to comply with the project requirements (see Sect. 6.2). Thus the experimental testing of this device has been necessary.

The opportunity to set up a testing simulator being able to replicate in a realistic way the motion dynamic effects of a railway vehicle on inertial sensors allows avoiding expensive on board acquisitions.

This section describes the algorithms which are part of the software components of the developed Hardware-In-the-Loop test rig. Since the implementation will involve the use of an anthropomorphic industrial manipulator as actuator, the simulated results, aimed to a preliminary validation of the proposed method, have been performed in Matlab-Simulink^{TM} environment with a kinematic model of a six-Degree of Freedom (DOF) serial robot.

It is worth to pointing out that the procedure has a general applicability in all fields dealing with inertial sensors.

4.1 Washout Filters

The aim of Washout Filters is not to reproduce the movements of the vehicle but that the simulator induces the same dynamic effects (accelerations and angular rates) the pilot would experience in the real scenario.

The classical WF strategy splits the reproduction of high and low frequency acceleration components:

- High frequency accelerations need a limited space so the simulator reproduces directly the same movement of the vehicle (Direct Linear Motion Strategy);
- Low frequency accelerations, which should need large movements, can be reproduced tilting the simulator: in this way the gravity vector is used in order that the pilot could feel the same accelerations he would experience in real conditions (Tilting Strategy).

The same for the angular rates:

- High frequency components need small rotations so the simulator reproduces them directly (Direct Angular Motion Strategy);
- Low frequency components, which lead to continuous rotations, are not reproduced since they would alter the perception of linear accelerations.

WFs, through high pass and low pass filters, treat separately high and low frequency components of the movement to be reproduced.

In both cases it is necessary that the bandwidths of the low-pass and the high-pass filters have non-zero intersection. The algorithm used to implement Washout Filters on the computer is called *Classical Washout Algorithm* (CWA) [19, 20], the first to be studied and, nowadays, the most common for industrial simulators. This is the simplest mathematically and the cheapest computationally.

For a detailed description of the CWA refer to [35].

4.1.1 Adaptation of Washout Filters to the inertial sensors case

The design of a simulator used for the testing of sensors is substantially different to driving simulators and, for same aspects, it is easier. As first instance there are not real-time needs: DM can calculate accelerations and angular rates and then they can be used as input data for the WF in a second moment.

The main problem, met in the transition, is linked to the higher sensitivity of the sensors compared to the vestibular apparatus. In driving simulators, an upper bound, equal to the sensitivity threshold of the human vestibular apparatus (3°/s), is imposed to ensure that angular variations, determined by the Tilting Strategy for the simulation of low frequency accelerations, do not affect the perception of angular rates.

In the case of simulators for sensors, the bound is the sensitivity of the gyroscopes, that is much less ($0.0125 \div 0.05$°/s/LSB). The consequence is an unacceptable increase of the time necessary to achieve the orientation determined by the Tilting Strategy (e.g. a tilt angle of 1,8°, necessary to simulate an acceleration of $0.3 m/s^2$, needs a time of $36 \div 144$s).

The problem can be overcome by testing separately for accelerometers and gyroscopes. In fact, whereas in driving simulators the pilot has to be simultaneously subjected to accelerations and angular rates, in the case of WFs for sensors, the data, collected at different times, can be post-processed together.

Further advantage linked to this solution is the possibility to reproduce all components of frequency for the gyroscope, with no need to filter out low frequency components.

4.1.2 Design of Washout Filters

The design of the Washout Filter is based on the definition of three frames:

- the absolute frame, A, related to the base of the manipulator;
- the relative frame, R, related to the vehicle in motion;
- the frame, S, related to the IMU, mounted on the end-effector of the manipulator;

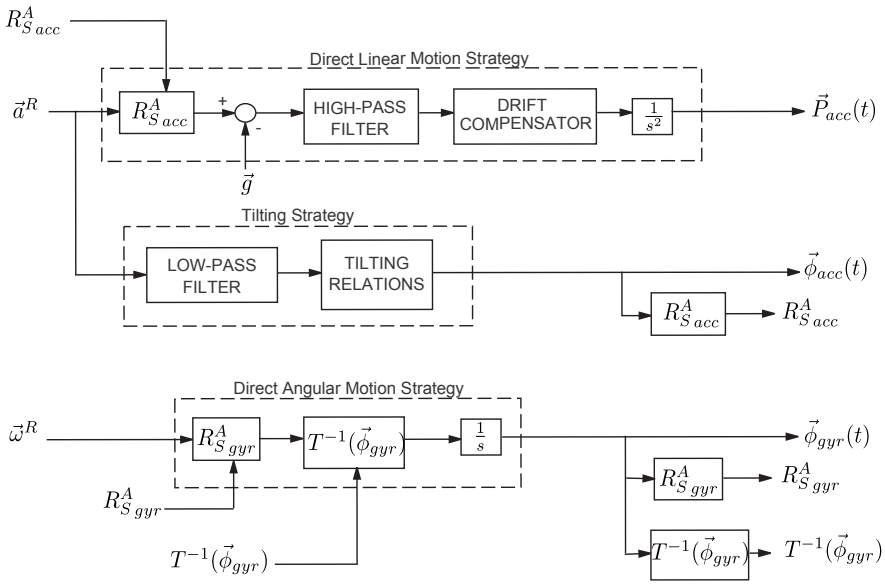

Figure 4.2: Design of Washout Algorithm Adapted for Inertial Sensors

Through the mathematical model of the vehicle (DM), dynamic effects ($\vec{a}^R$, $\vec{\omega}^R$), to which the sensors would be subjected if they were positioned on board, are calculated.

The scheme of the designed WF is shown in Fig. 4.2. In the scheme, it is possible to see clearly the two independent chains of the accelerometers and of the gyroscopes. Given the inputs $\vec{a}^R$ and $\vec{\omega}^R$, the WF provides the reference trajectory (position $\vec{P}$ and orientation $\vec{\phi}$) for the sensors mounted on the end-effector of the industrial manipulator, both for the accelerometer test ($\vec{P}_{acc}(t)$ and $\vec{\phi}_{acc}(t)$) and the gyroscope test ($\vec{\phi}_{gyr}(t)$).

The reference position $\vec{P}_{gyr}(t)$ is always equal to the initial position $\vec{P}(0)$ because the angular rates measurements are independent from the translational components of motion.

The references are generated such that the accelerations and angular rates ($\vec{a}^S_{mis}$ and $\vec{\omega}^S_{mis}$), measured by inertial sensors on the end-effector, are equal to those which would be measured on the vehicle.

$$\vec{a}^S_{mis} = \vec{a}^R \quad \vec{\omega}^S_{mis} = \vec{\omega}^R \tag{4.1}$$

$\vec{\phi}_{acc}(t)$ allows calculating $R^A_{S\,acc}$, to be used in the next step of the algorithm to rotate accelerations from sensor frame (*S–frame*) to absolute frame (*A–frame*).

Similarly for the gyroscopes' chain. $\vec{\phi}_{gyr}(t)$ is also used to calculate $T(\vec{\phi}_{gyr})$, the matrix which allows calculating the derivatives of the Euler angles from the angular rates.

The block *Drift Compensator*, after the high-pass filter (implemented as a first order filter), is most of all a second-order high-pass filter that allows avoiding drift of the position, with a reset for step and ramp inputs to the initial position of the platform.

The block *Tilt relations* calculates the roll and pitch angles (ψ_d and θd)* to replicate lateral and longitudinal accelerations, tilting the sensor from the horizontal plane.

$$\begin{cases} \theta = -\sin^{-1}\left(\dfrac{a^R_x}{g}\right) \approx -\dfrac{a^R_x}{g} \\ \\ \psi = \sin^{-1}\left(\dfrac{a^R_y}{c_\theta g}\right) \approx \dfrac{a^R_y}{g} \end{cases} \tag{4.2}$$

The yaw component ϕ has no effects on accelerometer measures because it does not change the orientation of $\vec{g}$ with respect to z_s axis. Thus, for accelerometers tests, ϕ is imposed to be constantly equal to its initial value $\phi = \phi(0)$.

4.2 Kinematic Control of Robot

The control algorithm for the robot is based on a Closed Loop Iterative Kinematic (CLIK) strategy [51, 5, 29]. Two different control algorithms are shown: the first based on the quaternion and the other with the optimization of the manipulability index.

4.2.1 Quaternion-based control

The position error $\vec{e}_p$ is defined as the difference between the reference obtained with WF and the effective position of the end-effector ($\vec{P}_d - \vec{P}_e$); the error

*The subscript *d* means that the angle will be the orientation reference to be tracked by the end-effector of the robot. These are obviously different from the ones defined in the Sect. 2.1

of orientation, $\vec{e}_o$, instead, is based on the quaternion representation as:

$$\vec{e}_o = \eta_e \vec{\epsilon}_d - \eta_d \vec{\epsilon}_e - S(\vec{\epsilon}_d)\vec{\epsilon}_e \tag{4.3}$$

where η_d and $\vec{\epsilon}_d$ are, respectively the scalar and vectorial components of the desired quaternion-based orientation of the end-effector provided by WF; η_e and $\vec{\epsilon}_e$ are, instead, the scalar and vectorial components of the effective quaternion-based orientation of the end-effector.

The CLIK algorithm is implemented in joint space. The 6 independent joint coordinates $q_i(t)$ are collected in the vector $\vec{q}(t)$.

The control law is based on the damped pseudoinverse matrix of the geometric Jacobian $J^\dagger = J^T(JJ^T + k^2 I)^{-1}$:

$$\dot{\vec{q}} = J^\dagger \begin{bmatrix} \dot{\vec{P}}_d + K_p \vec{e}_p \\ \vec{\omega}_d + K_o \vec{e}_o \end{bmatrix} \tag{4.4}$$

where K_p and K_o are square gain matrices, k is the damping factor, defined different from zero only when the manipulator is near a singular configuration (i.e. $\det(JJ^T)$=0), to ensure the inversion.

The evolution of position error has a first order dynamic:

$$\dot{\vec{e}}_p + K_p \vec{e}_p = 0 \tag{4.5}$$

Thus, the convergence of the real position to the reference one is ensured, when the damping of $J^\dagger$ is null (far from singularity configuration), if the gain matrix K_p is positive-definite.

The convergence of the orientation can be demonstrated, if the gain matrix K_o is positive-definite and $k = 0$, by means the Lyapunov's direct method.

The algorithm has good performances only when the robot is far from kinematic singularities. In this case, in fact, the stability proof is not valid anymore and the tracking error diverges.

4.2.2 Iterative Control with optimization of the manipulability index

Since the version of CWA adapted for the testing of accelerometers needs five DOFs, the robot has one DOF redundant (the yaw angle) which can be used to keep the robot far from kinematic singularities.

So, the controller algorithm is modified to maximize locally an objective function, that is the *index of manipulability* [51, 29].

In this case the orientation is described by Euler angles RPY. The reference vector has only five elements: the yaw coordinate is eliminated.

$$\vec{x}_d(t) = \left[\vec{P}_d(t), \phi(t), \theta(t)\right] \tag{4.6}$$

$$\dot{\vec{x}}_d(t) = \left[\dot{\vec{P}}_d(t), \dot{\phi}(t), \dot{\theta}(t)\right] \tag{4.7}$$

The analytic Jacobian J_A is a 5×6 matrix, thus it has a nontrivial kernel, $\mathcal{N}(J_A) \neq \{\vec{0}\}$. An element of the Jacobian's kernel can be added to the "pseudoinverse" solution, without modifying its stability properties.

$$\dot{\vec{q}} = J_A^*(\dot{\vec{x}}_d + K\vec{e}) + P\dot{\vec{q}}_A \tag{4.8}$$

P is a projector in the kernel. A possible choice is $P = I_{6\times 6} - J_A^{\dagger} J_A$. The new term, although it has no effects on the pose of the end-effector, changes the configuration of the manipulator, producing some eigenmotions.

The objective is to design $\dot{\vec{q}}_A$ in order to locally maximize the index of manipulability:

$$g(\vec{q}) = \sqrt{\det(J_A(\vec{q}) J_A^T(\vec{q}))} \tag{4.9}$$

The choice of $\dot{\vec{q}}_A$ proportional to the gradient of the manipulability index allows to achieve the objective:

$$\dot{\vec{q}}_A = k\left(\frac{\partial g(\vec{q})}{\partial \vec{q}}\right)^T \tag{4.10}$$

The gradient of $g(\vec{q})$ has to be calculated numerically. Thus, fixing a virtual increment Δq of the independent variable, it is possible to calculate the i-th element of the discrete gradient as:

$$\left(\frac{\partial g(\vec{q})}{\partial \vec{q}}\right)_i \approx \frac{g\left(\vec{q} + \Delta q\, \vec{e}_i\right) - g(\vec{q})}{\Delta q} \tag{4.11}$$

where $\vec{e}_i$ is a six element vector of zeros, with the i-th element equal to 1.

Concerning the gyroscope tests, even in this case, the six available DOFs are redundant. In fact, the translational components do not affect the gyroscope measures.

Thus the necessary DOFs are only three. Similarly to the above algorithm, one of the remaining three DOFs can be used to keep the robot far from kinematic singularities.

4.3 Simulation results of the dynamic simulator

In order to test the efficiency of the WF algorithm, the following tasks have been simulated in the Matlab-Simulink^{TM} environment with a kinematic model of a six-DOFs serial robot:

- import of kinematics data from the Dynamic Simulator;
- implementation of the CWA;
- implementation of the CLIK;
- direct kinematics of the manipulator;
- derivation of accelerations and angular rates.

The 3D multibody model of the railway vehicle described in Sect. 3.1 can be used as the Dynamic Simulator which provides the inputs to the CWA.

The definition of the kinematic model of the manipulator is based on the characteristics of the anthropomorphic industrial robot which will be included in the architecture of the HIL test rig as hardware device: the Comau SMART-SiX 6-1.4.

4.3.1 Comau Smart Six

The anthropomorphic manipulator Comau SMART SiX (Fig. 4.3), belongs to the family of the Comau robots used for the light handling and arc welding. Its structure is an open kinematic chain as is formed by links connected in series. The robot has six DOFs and is fixed to the ground by a steel structure.

The base of the robot is fixed; the column on which is placed the motoreducer for the axis #2, rotates about the vertical axis #1. The latter is connected to the forearm by means of an arm on which there are the geared motors of the axes #3, #4, #5 and #6. The robot wrist is positioned on the end of the forearm.

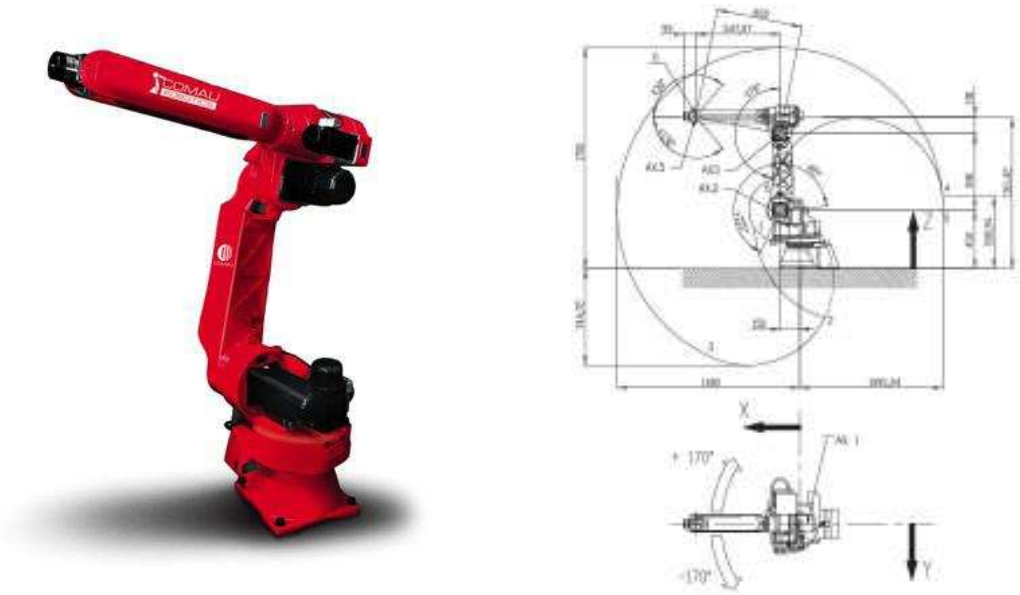

Figure 4.3: Robot Comau Smart Six

The axes previously mentioned are equipped with programmable limit switches and/or mechanical shock absorbers. The brushless AC motors are provided of a brake and an encoder for the measurements of position and velocity of each joint. The motors control the movement of the axes #1, #2, #3 and #4 of the robot, transmitting motion either directly by mechanical gear reducers. The axes #5 and #6 move using a belt transmission to a Harmonic Drive reducer. The technical characteristics of this manipulator are shown in the Tab. 4.1.

4.3.2 Kinematic model of the Smart Six

The modelling of the kinematics of the robot Smart Six arises from the implementation of the Denavit-Hartemberg (DH) convention and the definition of the four DH parameters for each link (a_i, d_i, α_i, θ_i) [50].

The first step of the DH convention is the "attachment" of a reference frame to each link.

First, as shown in Fig. 4.4, z_0 is defined on the direction of the first joint axis; the origin O_0 and x_0 axis for the base frame are free choice (axes y_i will not be mentioned, since they complete a right-handed reference frame based on z_i and x_i). The axis z_1 is placed on the direction of the joint 2 axis, pointing into the sheet; z_0 and z_1 are perpendicular to each other, so x_1 is accordingly defined as parallel the common normal to the two axes, passing through the origins O_0 and O_1.

It is worth to pointing out that an offset between the origins O_0 and O_1 is present and corresponds to the DH parameter a_1. Since O_1' matches O_0, then d_1=0. As regards the angles, θ_1 is variable and turning counterclockwise (CCW) around z_0.

Parameters of Robot COMAU Smart SiX	
PAYLOAD:	6 kg
ADDITIONAL LOAD ON FOREARM:	10 kg
TORQUE OF AXIS 4	11,7 Nm
TORQUE OF AXIS 5	11,7 Nm
TORQUE OF AXIS 6	5,8 Nm
STROKE OF AXIS 1	$\mp 170°$
STROKE OF AXIS 2	$-85° \div +155°$
STROKE OF AXIS 3	$-170° \div 0°$
STROKE OF AXIS 4	$\mp 210°$
STROKE OF AXIS 5	$\mp 130°$
STROKE OF AXIS 6	$\mp 270°$
SPEED OF AXIS 1	140° / s
SPEED OF AXIS 2	160° / s
SPEED OF AXIS 3	170° / s
SPEED OF AXIS 4	450° / s
SPEED OF AXIS 5	375° / s
SPEED OF AXIS 6	550° / s
MAXIMUM HORIZONTAL REACH	1400 mm
REPEATIBILITY	± 0,05 mm
MOTORS	AC Brushless
POSITION MEASURING SYSTEM	encoder
TOTAL INSTALLED POWER	3 kVA / 4,5 A

Table 4.1: Technical features Robot COMAU Smart SiX

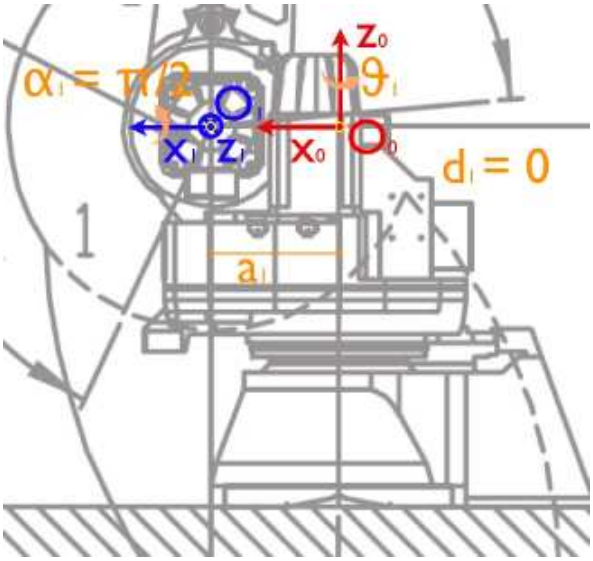

Figure 4.4: Reference frames for links 0 and 1

Since α_1 is the angle which allows superimposing z_0 on z_1, turning around x_1, $\alpha_1=\frac{\pi}{2}$.

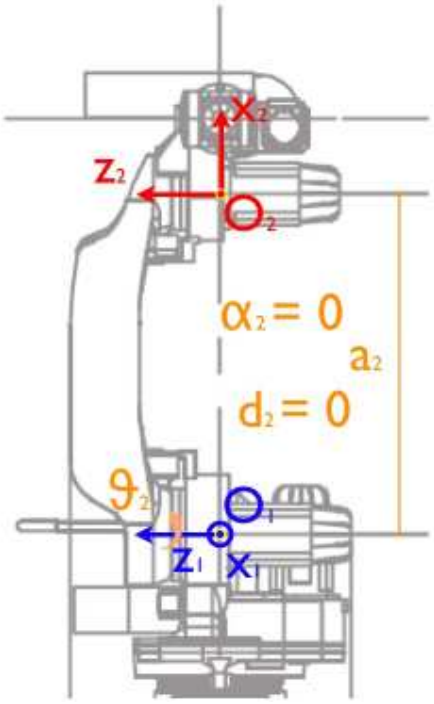

Figure 4.5: Reference frames for links 1 and 2

The axis z_2 is parallel to z_1 with the same direction (see Fig. 4.5), since it is placed on the axis of actuation for the third joint. The axis x_2 is collinear the perpendicular direction w.r.t. both the axes z and it is chosen in order to have d_2=0. a_2 is instead equal to the distance between O_2 and O_1. The angle θ_2 is variable while it turns around z_1. The parallelism of axes z implies that α_2=0.

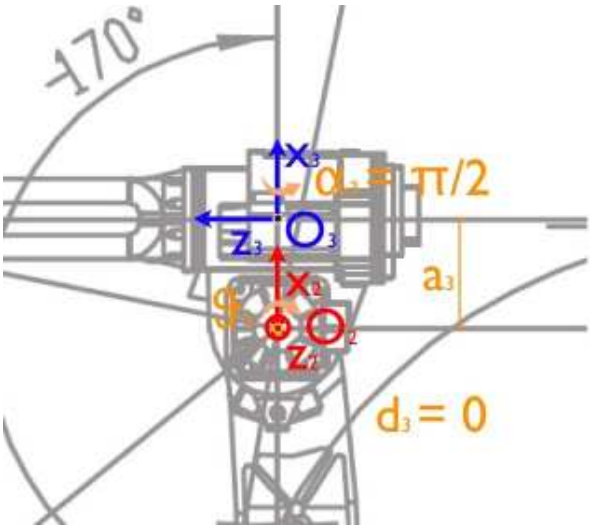

Figure 4.6: Reference frames for links 2 and 3

As shown in Fig. 4.6 the axis z_3 is defined parallel to the direction of the fourth joint axis. The origin 0_3 is located at the intersection of the common normal to z_2

and z_3. Since O_3'=O_2, trivially d_3=0. An offset between the joints 3 and 4 reoccurs: in fact the distance between O_2 and O_3 is equal to a_3. The angle θ_3 turns in a CCW direction around the axis z_2. In order to bring z_2 parallel to z_3, the first one must rotate 90 ° CCW around x_3; so α_3=$\frac{\pi}{2}$.

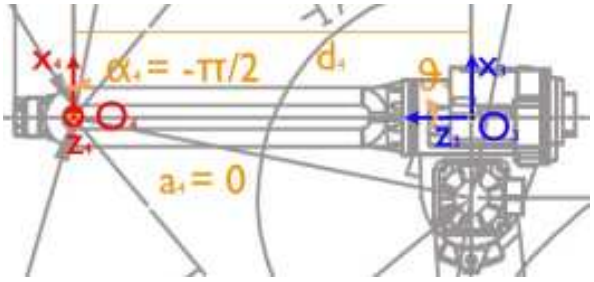

Figure 4.7: Reference frames for links 3 and 4

Fig. 4.7 shows that the axis z_4 is placed on the direction of the joint 5 axis, pointing into the sheet; z_3 and z_4 intersect at O_4, so it follows that a_4=0. d_4 is, instead, the distance between the centers (coordinated on z_3 of O_4). The angle of the joint 4, θ_4 is the rotating one around z_3. x_4 is taken on the normal common to both the axes z. In order to bring z_3 parallel to z_4, z_3 must turn 90° clockwise (CW) around x_4, so that α_4=-$\frac{\pi}{2}$.

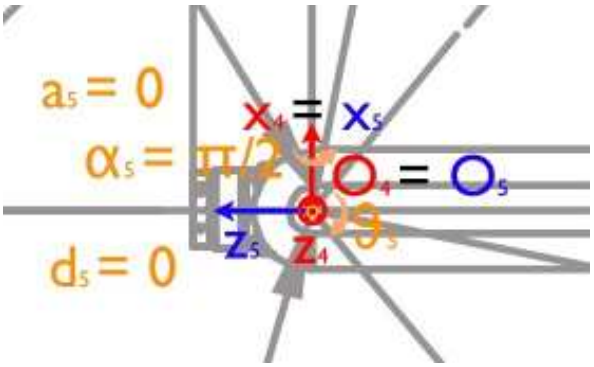

Figure 4.8: Reference frames for links 4 and 5

As depicted in Fig. 4.8, the axis z_5 is parallel to the direction of the sixth joint axis. In this case, z_4 intersects z_5 and, for the sake of simplicity, the origins are taken in the intersection point (O_4=O_5). So, trivially, a_6=0 and d_6=0. The angle θ_5 is taken variable turning about axis z_4; x_5 is perpendicular to both z_4 and z_5, so it can be placed coinciding with x_4. In this way z_4 must be rotated by 90° CCW along the x_5 to be coincident with z_5 (α_5=$\frac{\pi}{2}$).

For DH parameters with index 6, the reference frame depends on the end effector. In this paragraph the standard approach for a generic handling tool is reported (refer to Fig. 4.9): z_6 is the *approaching* direction, x_6 is the *sliding* direction, y_6 completes a right-handed reference frame. The result is that z_5 and z_6 are coaxial, so

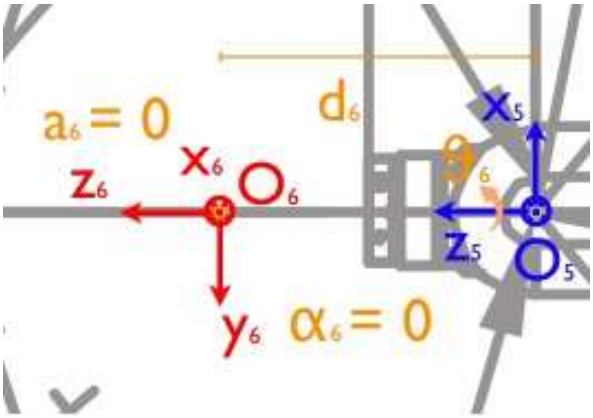

Figure 4.9: Reference frames for links 5 and 6

that a_6=0 and d_6 equal to the distance between the origins O_5 and O_6. The angle α_6 is trivially null, θ_6 is instead variable according to the rotation around the axis z_5.

The Tab. 4.2 summarizes the DH parameters, in reference to the technical data get by the data sheet of Comau Smart SIX [54].

Link i	a_i [m]	d_i [m]	α_i [rad/s]	θ_i [rad/s]
1	0.150	0	$\frac{\pi}{2}$	θ_1
2	0.590	0	0	θ_2
3	0.130	0	$\frac{\pi}{2}$	θ_3
4	0	0.647	$-\frac{\pi}{2}$	θ_4
5	0	0	$\frac{\pi}{2}$	θ_3
6	0	0.142	0	θ_5

Table 4.2: D-H parameters for the Comau Smart Six

The following rotation matrix explicits the relationship between the S frame (4.1.2)and the frame of the #6 axis:

$$R_S^6 = \begin{bmatrix} 0 & 0 & 1 \\ 0 & -1 & 0 \\ 1 & 0 & 0 \end{bmatrix}$$

The initial state of the joint variable matches the calibration configuration of the Smart Six, thus:

$$q_0 = [0^\circ\ 90^\circ\ 0^\circ\ 0^\circ\ -90^\circ\ 0^\circ]^T \tag{4.12}$$

4.3.3 Results from simulations

The results of the simulations performed with the system of control CWA+CLIK described in the current Chapter are reported in this section.

The bandwidth of the filters of the *Direct Linear Motion Strategy* and of *Tilting Strategy* has been chosen partially overlapped: for the longitudinal and lateral accelerations the bandwidth of the high-pass filter is $B_{HP} = [5; +\infty)$ Hz, while the one of the low-pass filter is $B_{LP} = [5; 40)$ Hz.

Two relevant test runs provided by the 3D multibody model have been used as input†. Their features are reported in Tab. 4.3. The first (ID 59) is a braking from 200 to 100 km/h with degraded adhesion; the track is curved and uphill. The second (ID 108) is a traction from 0 to 200 km/h with degraded adhesion; the track is curved and downhill.

ID	Adhesion	Maneuver	WSP Anti-Skid	Curves	Altimetry	Irregularities
59	Degraded	Braking	On	Curves	Uphill (3 %)	Regular
108	Degraded	Traction	On	Curves	Downhill (3 %)	Regular

Table 4.3: Features of the test runs

It is worth noticing that, for both runs, the reproduction of the vertical acceleration is affected by error: this is predictable since *Tilting Strategy* does not allow reproducing the components of acceleration along this axis. The fact that high frequency components (over 50 Hz) are not exactly reproduced is not a problem, because the inertia of the joints should cut the frequency at lower values (10 Hz). Since the lack of filters in the test for gyroscopes, there are not any errors in the reproduction of angular rates.

†The ID is related to the set of two-hundred test paths get by the 3D multibody model for the testing of the localization algorithms

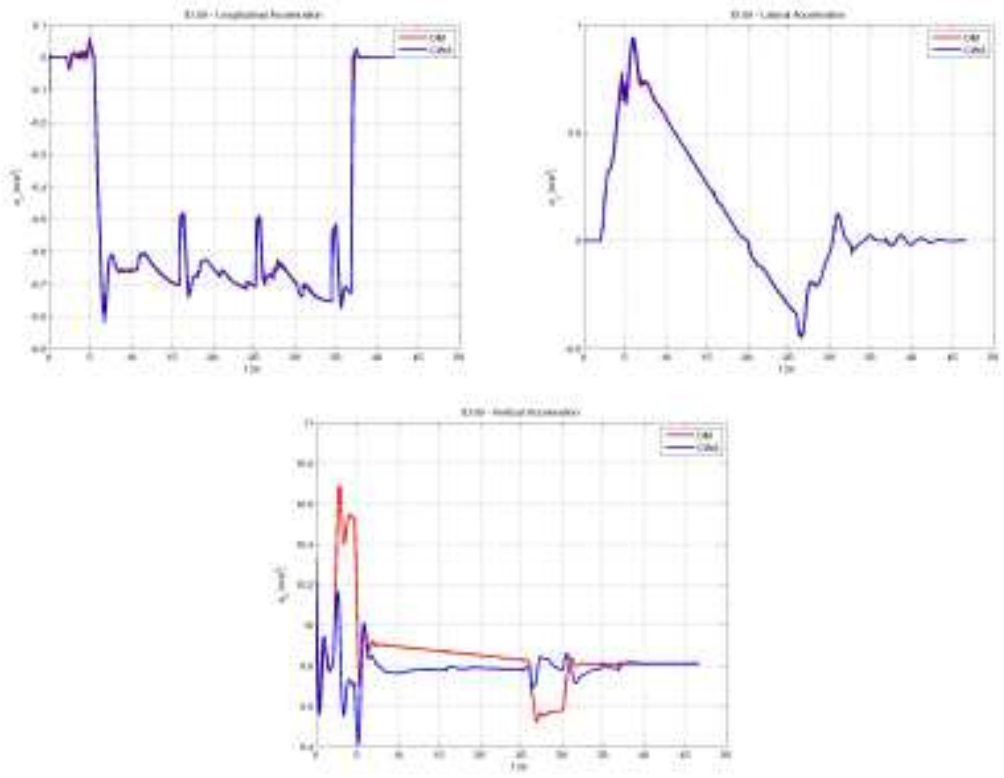

Figure 4.10: Path #59 - Acceleration

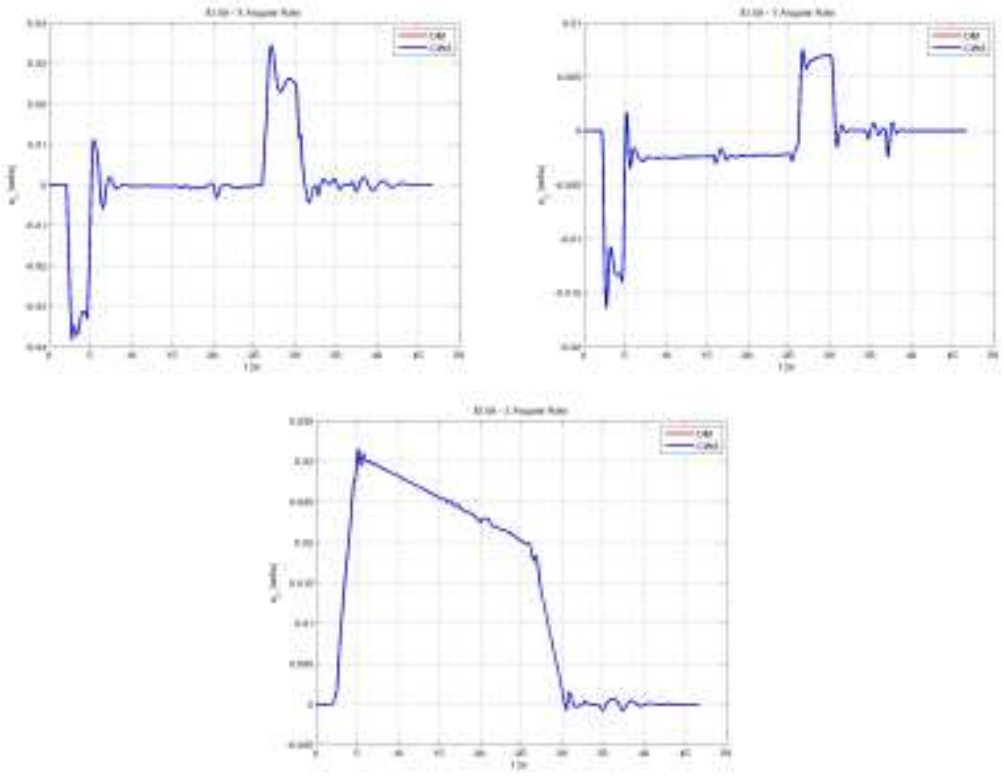

Figure 4.11: Path #59 - Angular Rate

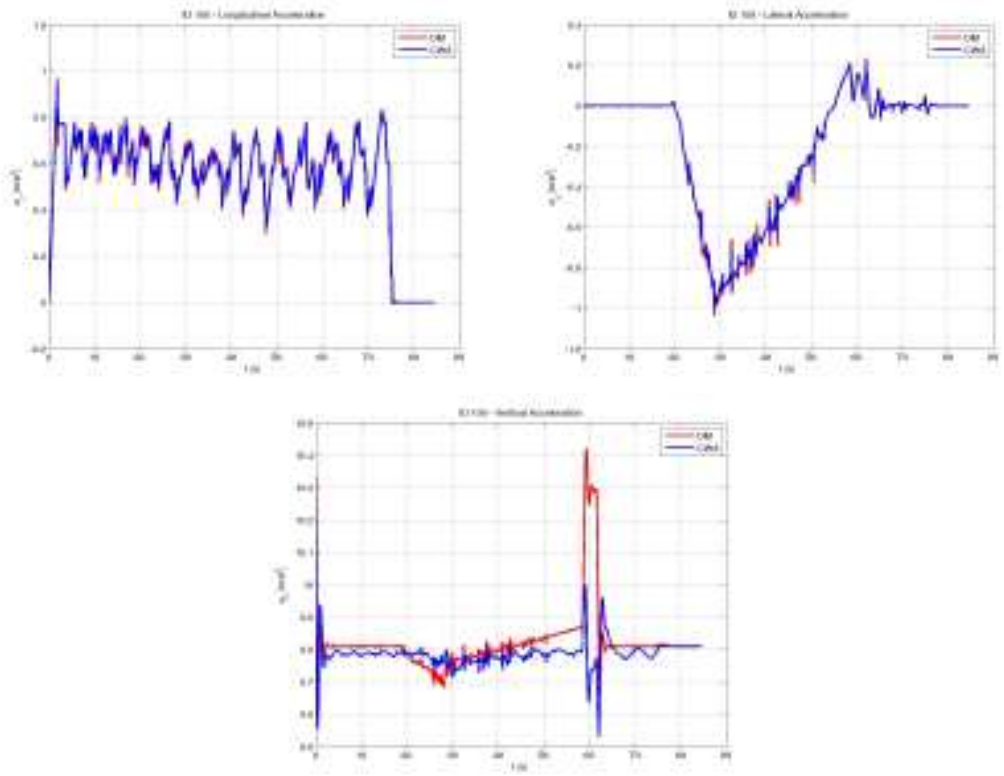

Figure 4.12: Path #108 - Acceleration

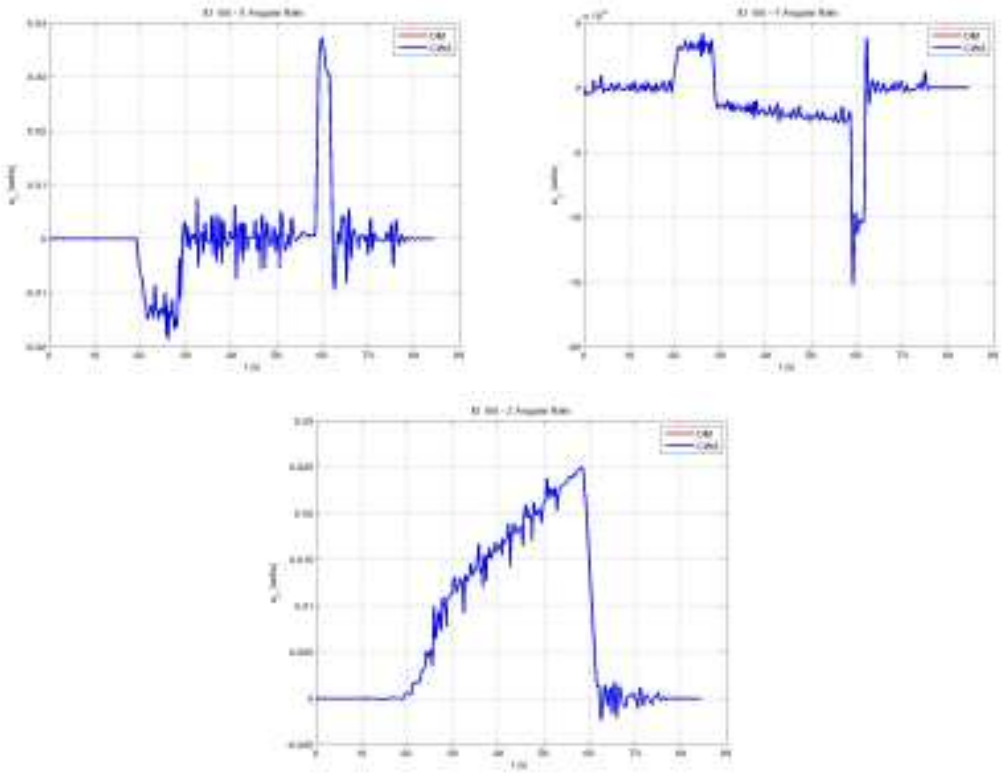

Figure 4.13: Path #108 - Angular Rate

Chapter 5

Implementation of a Dynamic Simulator for the testing of inertial sensors

The preliminary off-line results of the dynamic simulator have encouraged to set up a Hardware-In-The-Loop (HIL) test rig which is able to test the localization algorithm performances through the testing of the inertial sensors. In this section a particular focus is reserved for the hardware and software components which are part of the architecture of whole rig and which up now have not been described yet. Then the results of the testing of the rig have been reported in the final section of the current chapter.

The Figure 5.1 shows the HIL test rig in the Mechatronics and Dynamic Modelling Laboratory (MDMLAB) of the Department of Energy Engineering of the University of Florence, located in Pistoia inside the ITTS "Silvano Fedi".

Figure 5.1: Hardware-In-The-Loop test rig: 1) industrial robot Comau SMART-SiX 6-1.4, 2) C4G control unit, 3) external Linux host, 4) IMU MTi-G by Xsens

5.1 Architecture of the HIL test rig

The HIL test rig, so as represented in Fig. 5.2, is composed of:

- a Windows^{TM} host;
- a GNU/RTAI/RTNET/Linux host;
- the six-DOFs anthropomorphic manipulator with spherical wrist, Comau SMART-SiX;
- the IMU MTi-G by Xsens, placed on a plate assembled on the end-effector of the robot;
- the robot controller, C4G Control Unit.

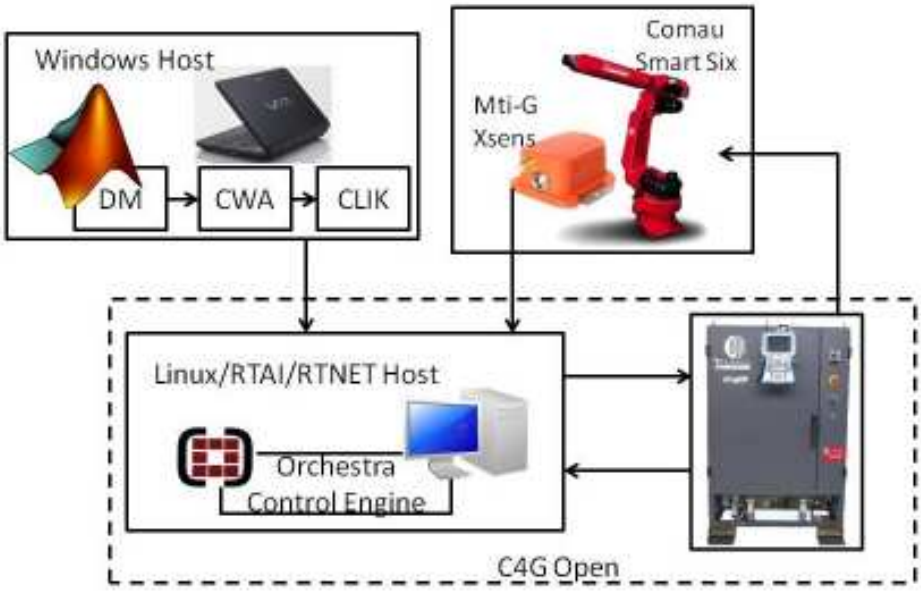

Figure 5.2: Architecture of the HIL test rig

The Windows^{TM} host, thanks to the Matlab-Simulink^{TM} environment, provides the implementation of the 3D multibody model of a railway vehicle (DM) and of the CWA + CLIK system (see Sect. 4.1).

The respect of strict timing constraints for the tracking of the trajectories is possible through a GNU/RTAI/RTNET/Linux host interacting with the standard C4G Control Unit. The whole system constitutes a unique architecture of control, called Comau C4G Open, which permits to overcome the typical constraints of robot controllers closure.

The implementation of the open controller is performed through the suite Orchestra Control Engine which provides the libraries and the softwares to interact with the C4G Control Unit.

The anthropomorphic robot and the IMU placed on its end-effector are the hardware devices of the dynamic simulator. It is worth noticing that the architecture is valid for a generic inertial platform. For the testing activities of the HIL rig, an available on market platform which guaranteed high reliability has been chosen: the MTi-G by Xsens.

In the next sections the components C4G Control Unit, C4G Open, Orchestra Suite and MTi-G are briefly described.

5.1.1 C4G Control Unit

The C4G Control Unit is an industrial apparatus created to manage a cell which a robot Comau is assigned to. It has the following characteristics:

- supply voltages from 400 Vac to 480 Vac;
- Digital Servo Amplifier (DSA) Unit to control motors up to 600V;
- management of robots configured with up to 10 interpolated axes with a maximum power up to 12 kVA, equipped with brushless synchronous motors and high resolution position encoder;
- operators interface Terminal: TFT 6.4" display with 4096 colors "User friendly" graphical interface;
- communication interfaces (USB, Serial and Ethernet);
- options for the management of the most common field-buses (DeviceNet, Profibus-DP, Interbus-S and EtherNet / IP).

C4G Control Unit is composed of the following modules, as shown in Fig. 5.3:

- **DPP (Distribution Power Panel) -** distributes the power supply to the auxiliary circuits (APS) and to the drivers (DSA);
- **APS (Auxiliary Power Supply) -** provides the necessary voltages to the submodules RPU, DSA and to the interface modules of the control;
- **RPU+ (Robot Processing Unit Plus) -** is the main unit of control, consisting of RPS and SMP+. It manages traffic information in the Control Unit, including networks, programs and exchange of information to the driver and to the security modules;
- **DSA (Digital Servo Amplifier) -** provides power to the motors of the robot;

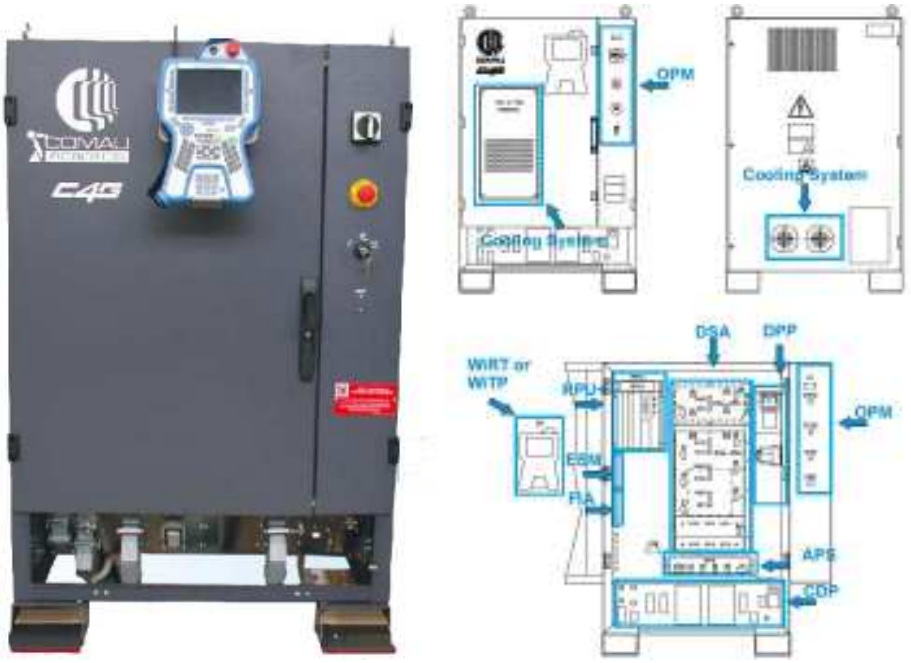

Figure 5.3: C4G Control Unit

- **FIA3 (Field Interface Adapter Rel. 3) -** is an interface board aimed to the internal routing of all the internal connections of Unit of Control;
- **ESM (Electronic Safety Module) -** provides the following functions: selection of the mode of operation, emergency stop, security gates and general stop;
- **Operator Interfaces -** is the set of devices through which the user interacts with the Control Unit including the OPK (Operator Panel Kit), the Terminal of Programming and the program WinC4G;
- **CDP (Cabinet Distribution Panel) -** panel containing all the connectors of the Control Unity.
- **Cooling System**

C4G Control Unit provides specific user interfaces to handle the robot, create, modify and execute the scripts:

- Terminal of Programming (WiTP): manually controls the movements of the robot, allows modifying and running the programs step by step, monitors the system;
- Software for PC (WinC4G): allows viewing the files on the Control Unit, editing and translating them into executable format (.COD) and displaying the errors.

The programs implemented through the WinC4G interface are written in PDL2 [53], a programming language similar to Pascal, but oriented to the programming for robotic applications. It contains instructions of movement, sending and receiving information, controlling the order of execution of the same, error checking, etc.. The PDL2 programs are divided into two categories:

- holdable: permit movement instructions;
- non holdable: for the process control; do not contain movement instructions.

C4G Control Unit provides three modalities of command, selected through the selector key switch in the cabinet:

- Manual (T1): used for handling at low speed, in order to program the trajectory of the robot;
- Local Automatic (AUTO): used for the execution of scripts automatically at the set speed, initiated by the programming terminal;
- Remote Automatic (REMOTE): used for the execution of scripts automatically at the set speed, initiated by external devices.

DRIVE ON e DRIVE OFF represent respectively the commands to switch on and off the motors of the robot.

5.1.2 C4G Open Systems

With reference to [52], C4G Open is an integration of the industrial robot controller: an external PC communicates real-time with the C4G control, interacting at various levels in the control and in the generation of the trajectory. The system architecture is based on the real-time communication over Ethernet, which uses an owner UDP protocol between SMP+ (network client) and the PC (server), as shown in Fig. 5.4.

The communication requirements introduced previously are met through a computer arranged to work in real-time: hard real-time requirements are necessary, since the PC must respond to SMP+ in a predetermined sampling period, up to a minimum of 1 ms.

For the aim of this work, it has been decided to use a Linux with RTAI patch computer in order to meet the real-time requirements, thanks to the protocol RT-NET.

C4G Open is characterized by several types of operation, called Modalities. The Modalities used for the purposes of this thesis, are:

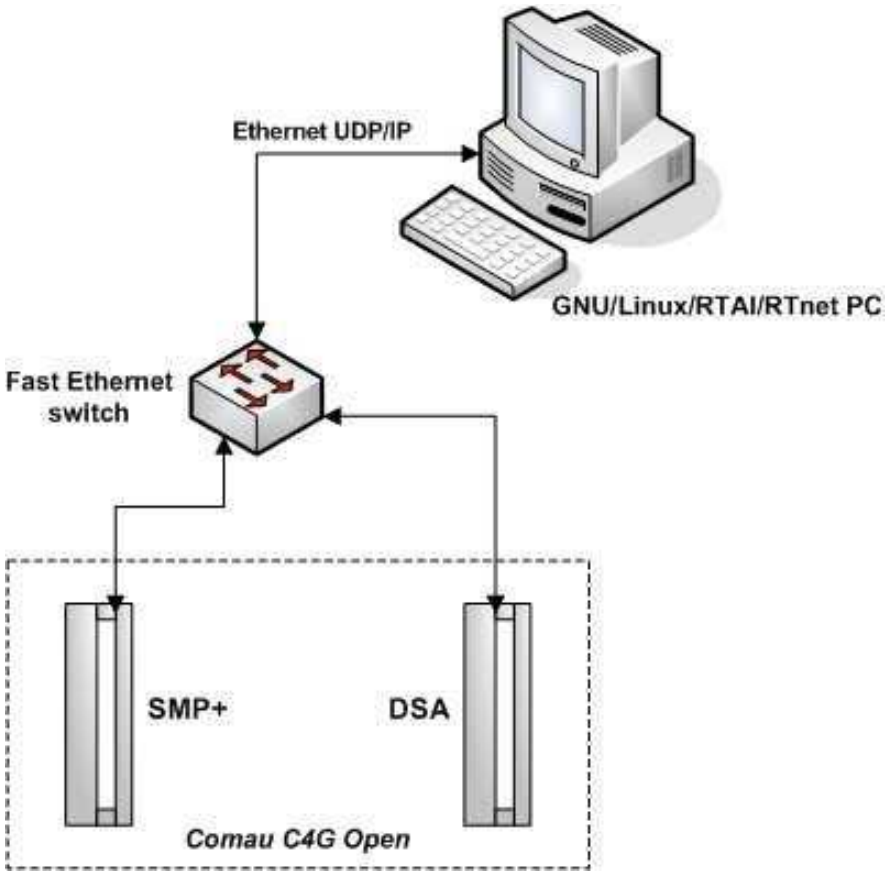

Figure 5.4: Open Controller

- Modality 0: the PC does not participate actively in the movement of the robot, but it must be present and respond to each packet sent by SMP+;
- Modality 5: allows the PC to generate the trajectory in position and speed, in a relative manner purifying it of calibration constants at each instant.

In Figure 5.5 the functional block diagram that realizes the particular configuration of the Modality 5 is reported. It is based on the relative positions provided both by PC and SMP+.

C4G schedules the new reference position pos_i and velocity vel_i from the trajectory generator. The external host computes the new desired position pos_j and velocity vel_j. The overall reference position, pos_k, to be sent to the DSA, are not neither the SMP+ ones and the PC ones, but are calculated according to the total reference positions obtained in the previous step pos_{k-1} and the overall reference speed vel_k. The latter is calculated as the sum of vel_i and vel_j appropriately scaled with the velocity override factor of the machine.

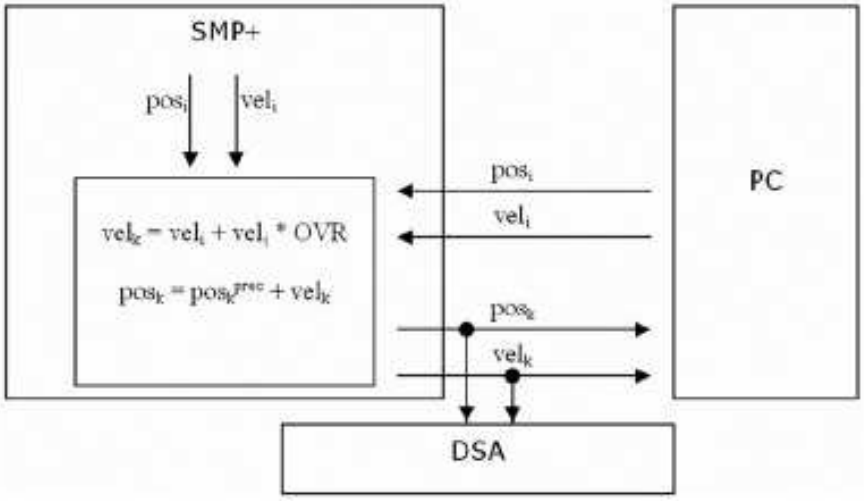

Figure 5.5: Configuration of the Modality 5 of the C4G Open

5.1.3 Orchestra Control Engine

The control of the robot through C4G Open is implemented on the PC through the suite Orchestra Control Engine, a set of software components addressed to develop real-time control applications for machines, robots, cells and industrial plants.

The suite is developed by Sintesi SpA * and includes solutions for PLC, CNC and open controller of robots.

Orchestra for Open Robot Controllers is the solution that allows the rapid prototyping of control algorithms for industrial robots and include the following components:

- OrchestraCore;
- OrchestraDesignerv;
- OrchestraBuilder;
- OrchestaHMI;
- Kinematics Modules;
- C4G Open Library;

OrchestraCore allows implementing control algorithms with a fixed period of execution, by means of the combination of modules predefined by the user. Each

*Sintesi develops high-performance components and solutions for sophisticated motion and position control of mechatronics systems - www.sintesi-am.eu

module is defined by a number of inputs and/or outputs, by internal states and by a set of parameters. Each module can be associated with three separate files:

- DLC, a binary file obtained after compiling a cpp file of actions to do;
- XMI, a configuration file that defines the structure of the module;
- XMP, an optional file that contains the declaration of any parameters.

C4G Open Library, Orchestra Designer and Orchestra HMI are the most relevant components of the Orchestra Control Engine.

The C4G Open Library is a C++ library that interfaces the external Linux PC to the C4G controller. The interface is achieved by the exploitation of the API (Application Programming Interface) of the C4G Open Library [48, 44, 45].

A typical application of control is composed of two modules (*C4G Sensor* and *C4G Actuator*) which must always be present. These two elements respectively send and receive packets from/to C4G Open, using the appropriate classes of C4G Open Library. The additional modules are defined by the user in order to get the desired strategy of control. As shown in Fig. 5.6 the interaction between the remaining modules of the control loop and the controller C4G is always guaranteed by the modules *C4G Sensor* and *C4G Actuator*.

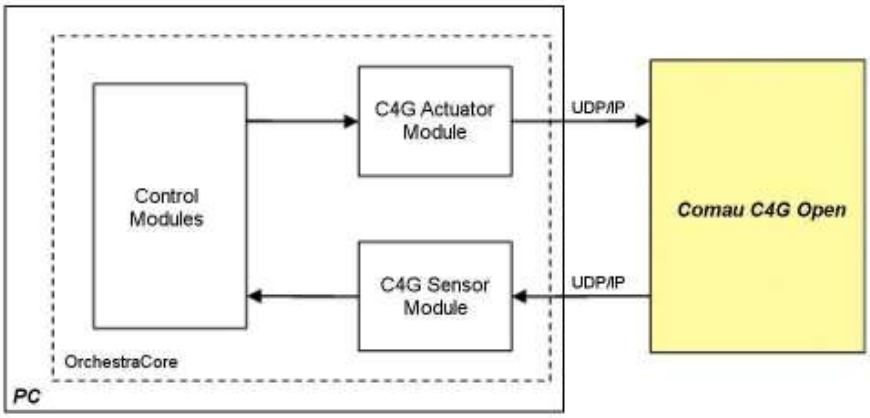

Figure 5.6: Cycle of control in Orchestra

Orchestra Designer [46] is a tool of the suite Orchestra aimed to design a control cycle in a simple and immediate way. It consists of a GUI (Graphic User Interface), shown in Fig. 5.7, which graphically depicts the topology of the control scheme to be implemented. It can be used to create or change the settings interface module (.xmi) and its parameters (.xmp). It also includes a file editor to compile and generate the binary code (.dlc). Orchestra Designer creates the project file (.xpr) and the executable one (.xcl).

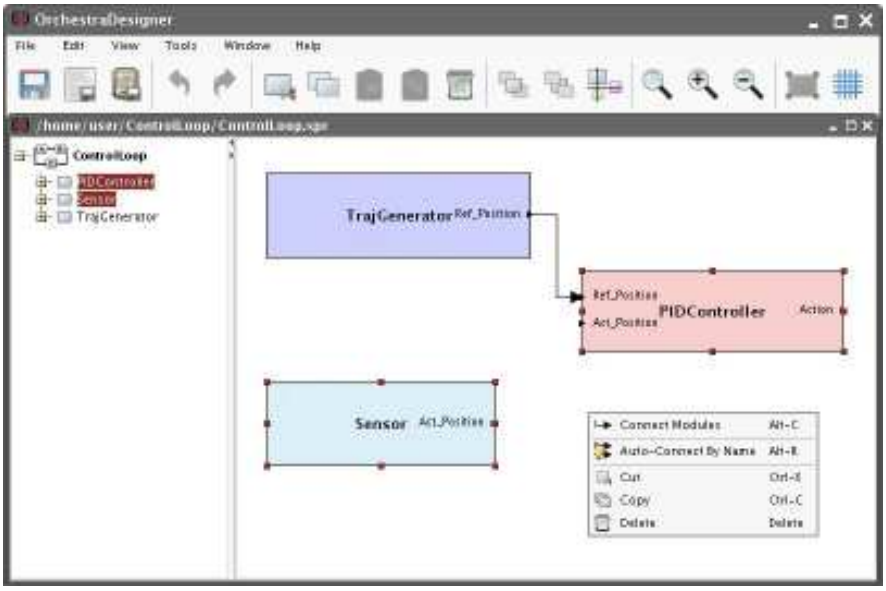

Figure 5.7: Screenshot of Orchestra Designer

Orchestra HMI (Human Machine Interface) [47] is an application that monitors a set of control tasks performed in real-time. This tool is essential to save the output data from the module C4G Sensor (i.e. position and speed of each axis).

5.1.4 The inertial platform MTI-G Xsens

The device MTI-G ([58]) shown in Figure 5.8, is an IMU (Inertial Measurement Unit),an excellent unit of measurement used in controlling and navigation of vehicles and other objects. It is an electronic device that includes MEMS inertial sensors, a triaxial accelerometer and a triaxial gyroscopes, a GPS receiver in a smaller scale and other additional sensors as a 3D magnetometer and a static pressure sensor.

Orientation, velocity and position are estimated using an Extended Kalman Filter (EKF). In the step of prediction of the Kalman filter the inertial sensors are integrated over time. These estimates are not precise due to small deviations which characterize the accelerometers and gyroscopes. This error will increase in time. In the correction step, however, the movement is corrected using data from the GPS receiver and the signal of the static pressure sensor (barometer). The aforementioned correction provides the mounting of GPS antenna on the device itself.

The data provided by the device depend on the type of reference system used for the coordinates. Three types of reference systems are available:

- **Default MTi-G body fixed coordinate system (S_{xyz}):** the right-handed coordinate system, aligned to the housing of the MTi-G. By default, this system is used to express the calibrated data in (3D rate of turn, 3D acceleration, 3D

Figure 5.8: MTi-G Xsens - NWU reference

magnetic field) and corresponds to the NWU convention. It is possible to use a NED convention coordinate system for calibrated data;

- **Ellipsoidal Earth coordinate system:** Longitude, Latitude, Altitude (LLA), according to WGS-84[†]. The MTi-G's position output is expressed in LLA;
- **Local Tangent Plane (LTP):** the coordinate system that is a local linearization of the LLA. In the MTi-G, LTP can be expressed in North-West-Up (NWU) convention (default) or North-East-Down (NED). NWU is the default frame for the expression of the 3D velocity in the MTi-G.

As regards the data, three default formats of output are available and depend on the type of reference system used:

- *Orientation:* is the orientation between the sensor-fixed coordinate system **S**, and the Local tangent plane (LTP) coordinate system, **G**;
- *Position:* is expressed in Ellipsoidal Coordinates (Latitude, Longitude, Altitude (LLA)) in the WGS-84 Ellipsoid;
- *Velocity:* is expressed in the LTP **G**;
- *Calibrated data:* including accelerations, rate of turn, magnetic field, are in the right handed Cartesian coordinate system, corresponding to a North-West-Up (NWU) convention coordinate system **S**.

[†]latest review of the World Geodetic System

The three different formats can be easily combined by customizing the choice of data that will form the information packet. The result is a customized package containing information about the orientation, the position, the velocity, the calibrated inertial data and the time stamp. For the purposes of this work the output format with the calibrated (see Tab. 5.1) data has been selected.

Xsens MTi-G			
Parameters [unit]	**Angular rate** [deg/s]	**Acceleration** [m/ s^2]	**Magnetic Field** [mGauss]
Dimensions	3 axes	3 axes	3 axes
Range [units]	+/- 300	+/- 50	+/- 750
Linearity [% of FS]	0.1	0.2	0.2
Stability error [units 1σ]	1	0.02	0.1
Stability scale factor [% $1\ \sigma$]	-	0.03	0.5
Noise density [units/$\sqrt{Hz}$]	0.05	0.002	$0.5(1\sigma)$
Alignment error [deg]	0.1	0.1	0.1
Bandwidth [Hz]	40	30	10
Resolution A/D [bit]	16	16	16

Table 5.1: Technical specifications MTi-G

The physical sensors inside the MTi-G are all calibrated according to a physical model of the response of the sensor to various physical quantities, e.g. temperature, acceleration, etc. The basic model is linear and according to the relation 5.1:

$$s = K_T^{-1} \cdot (u - b_T) \tag{5.1}$$

This model is, indeed, more complicated and is continuously being developing further. From factory calibration for each MTi-G a gain matrix K_T and a bias vector b_T have been assigned. The calibration data is used to relate the sampled digital voltage output **u**, from the sensors, to the respective physical quantity **s**.

The gain matrix is split into a gain matrix **G** and a misalignment one **A**. The misalignment specifies the direction of the sensitive axes with respect to the ribs of the body reference system **S** housing. Below, the matrix **A** is shown: the first element of the misalignment $a_{1\ x}$ describes the sensitive direction of the accelerometer on channel 1:

$$A = \begin{bmatrix} a_{1x} & a_{1y} & a_{1z} \\ a_{2x} & a_{2y} & a_{2z} \\ a_{3x} & a_{3y} & a_{3z} \end{bmatrix} \quad G = \begin{bmatrix} G_1 & 0 & 0 \\ 0 & G_2 & 0 \\ 0 & 0 & G_3 \end{bmatrix}$$

from which the matrix K_T is obtained:

$$K_T = \begin{bmatrix} G_1 & 0 & 0 \\ 0 & G_2 & 0 \\ 0 & 0 & G_3 \end{bmatrix} \cdot \begin{bmatrix} a_{1x} & a_{1y} & a_{1z} \\ a_{2x} & a_{2y} & a_{2z} \\ a_{3x} & a_{3y} & a_{3z} \end{bmatrix} + \mathbf{O}$$

where **O** models higher order phenomena, patterns of temperature, g-sensitivity corrections etc..

In the HIL rig the inertial unit MTi-G is connected to the PC-Linux host through an USB cable and protocol RS-232. The data are acquired with a sampling frequency of 100 Hz. It has been necessary to create a software interface to handle the communication between the IMU and the host. The interface has been realized in the programming language C++ and exploits the class *CXbus*, defined in the header file Xbus.h, provided by Xsens. It can be used on both Linux and Windows. Its functions are implemented within the file Xbus.cpp.

The communication protocol is based entirely on messages, both to change configuration and to retrieve the data in the desired format. The configuration can be set by user: input/output synchronization, sampling frequency, baudrate, data format, etc.

The default configuration of MTI-G is shown in the Tab. 5.2.

Xsens MTi-G	
Property	**Value**
Output format	Orientation
Output setting	Orientation expressed through quaternion
Sampling frequency	100 Hz
Baudrate	115k2 bps

Table 5.2: Default configuration of MTi-G communication

5.2 Experimentation of the HIL test rig

The testing procedure implemented for the experimentation of the HIL test rig has been reported in this section.

Fig. 5.9 shows the sequence of the most relevant points of the procedure, starting from the preliminary tasks in green (Configuration of the system and the Course Alignment).

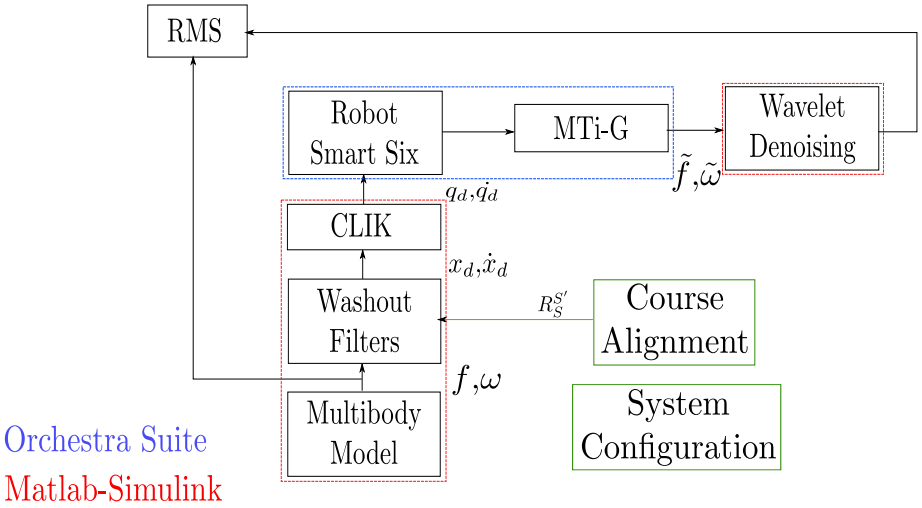

Figure 5.9: Testing procedure

The Configuration of the system includes all the tasks to make the hardware and software components ready to implement their functionalities.

- connection of USB cable of the MTi-G to the Linux host;
- launch of the software for the background storage of the MTi-G data;
- configuration of the real-time functionalities of the Linux host;
- configuration of the Orchestra HMI for the real-time monitoring of the data;
- loading of the *non-holdable* PDL2 scripts which are devoted to handle the C4G Open configuration.

The Course Alignment is a tricky task and will be described more in detail in the next section.

The sequence of tasks of the procedure of experimentation is linear and provides:

- through the 3D multibody model in Matlab-Simulink^{TM}, a test path with the desired features is generated;
- Washout Filters, taking into account the matrix of misalignment $R_S^{S'}$, calculates the desired trajectory of the end-effector, even in Matlab-Simulink^{TM};
- the CLIK algorithm provides the joint and the speed joint trajectories, which are automatically set to be suitable to compiled by the Orchestra Core;

- the robot motion is provided by the synergy of the Orchestra tools and of C4G functionalities;
- the acquisition of the MTi-G is synchronized to the start of the robot motion. The IMU sends the data to the Linux host;
- in the post process phase, data read by the IMU are filtered, exploiting the Wavelet decomposition property of de-noising, and compared to the reference ones;
- the RMS between measured and reference data provides an index of the performances of the HIL test rig.

More details about the Orchestra control loop and the post process task are given in the further sections.

5.2.1 Course alignment

This section explains the performed calibration procedure, called *Course Alignment* of the axes, for the compensation of the misalignment due to the assembly error.

As just said in 3.2.1 these procedures exploit the accelerometer leveling and are very important since avoids that the assembly error affects the estimates of the railway vehicle.

As regard the procedure of experimentation of the HI test rig, in order to avoid that the user should be forced to remove by hand the misalignment error due to gravity in the post-process phase for each acquisition, a preliminary procedure to be executed each time a sensor is placed on the end-effector of robot has been defined.

This procedure allows the CWA+CLIK system to generate joint and joint speed trajectories which already take into account the assembly errors.

In practice the IMU is fixed with respect to a reference frame, called *S'-frame*, which is different from the ideal one (*S-frame*) described in (see Fig. 5.10). The rotation matrix between *S-frame* and *S'-frame*, $R_S^{S'}$ can be estimated, starting from the detection of each angle error (roll, pitch, yaw) through the acceleration measurements.

In particular, from the static configuration it is possible to get the roll ($\delta\psi$) and pitch ($\delta\theta$) error values:

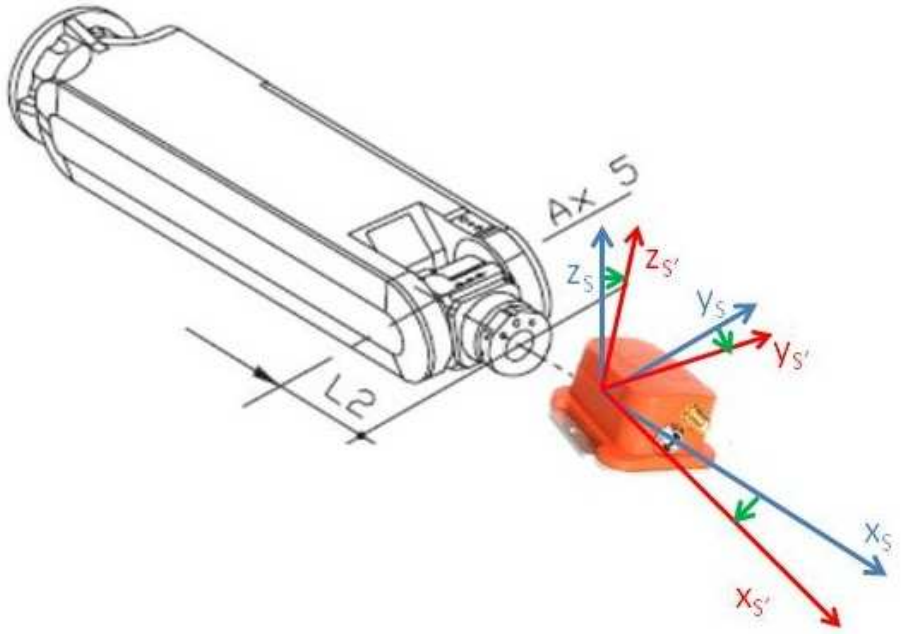

Figure 5.10: Misalignment of IMU sensor w.r.t. the body frame

$$\delta\psi = \text{atan}\left(\frac{f_y^S}{f_z^S}\right)$$
$$\delta\theta = \text{asin}\left(-\frac{f_x^S}{9.81}\right) \tag{5.2}$$

A temporary rotation matrix based only on roll and pitch errors is calculated and applied to the sensor, so that z_S=$z_{S'}$ and $x_{S'}$, $y_{S'}$ rely on x_S,y_S plane.

For the estimation of the yaw error ($\delta\phi$) value, it is necessary to rotate the end-effector of the robot in order that the third axis of the IMU is in gravity. Through an acquisition on this second static configuration, it is possible to estimate the yaw error value:

$$\delta\phi = \text{atan}\left(\frac{f_x^S}{f_y^S}\right) \tag{5.3}$$

At this point it is possible to calculate the definitive rotation matrix $R_S^{S'}$. This matrix intervenes pre-multiplying the acceleration and angular rates input from the dynamical model.

5.2.2 Orchestra control loop

As previously mentioned, the joint and joint speed trajectories are the output of the CWA+CLIK system.

It was then thought an efficient way to transfer data from the Matlab-Simulink^{TM} environment to the Orchestra Suite. It has been possible through the implementation of a Matlab function which would be able to generate automatically the .cpp file, in order to be ready to be compiled by Orchestra.

The function is also responsible for the resampling of the data, since, in Matlab the simulation sample time is T_s=0.01 s, while the working period of the robot is T_s=0.002 s. In particular, a technique whereby the position and speed references are passed after 5 cycles of work, is implemented.

The result of the compilation of the automatically generated .cpp file, is the *Module* block which has the aim to "feed" the C4G Actuator block with the joint and joint speed trajectories.

In fact, as can be seen in Fig. 5.6, a typical application in Orchestra Core is always composed of two modules (C4G Sensor and C4G Actuator) which, respectively, receive and send packets from/to C4G Open.

These blocks have been also provided of the functionality to convert the desired joint variables from the DH convention to the COMAU convention[‡] and to take into account the calibration offsets (q^0_{mC}) and the kinematic gains (K_r) which relate the variables on the motors side q_{mC} with those on the link side q_C, according to:

$$q_{mC} = K_r \frac{q_C}{360} + q^0_{mC} \tag{5.4}$$

More details can be found in [58].

The fourth module implemented in the Orchestra Control Loop, see Fig. 5.11, allows retrieving the measurements from the MTi-G, through the functionality of the mailboxes. The mailboxes are instances of the class CoreMbxModule: it allows one or more modules in a control loop to interact with other external programs.

The module *Xsens acc* (or *Xsens gyr*) interact with a backgroung external software based on the class CXbus (and launched in the preliminary phase of configuration of the system). Since the acquisition of the IMU takes place when the robot starts to move, its calibrated data are acquired by the host in real time.

[‡]the direction of rotation for the axes #1, #2, #4, #5, #6 is inverted in the convention implemented by the C4G controller

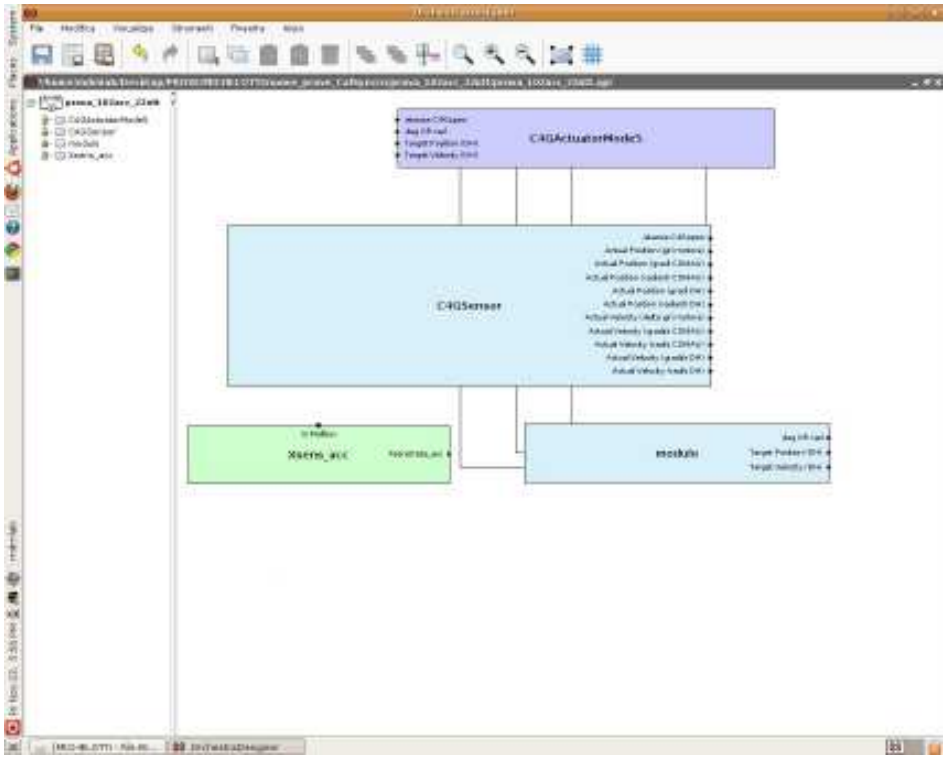

Figure 5.11: Orchestra Control Loop

5.2.3 Data Post-processing

The performance analysis of the HIL test rig is based on the comparison between the dynamic effects calculated by DM and the corresponding measures of the inertial sensors.

The frequency analysis of DM's output signals, by means of FFT, highlights that the vehicle dynamics involves only the frequencies less than 3 Hz. In Fig. 5.12 the FFT of the longitudinal and lateral accelerations of one of the simulated test are shown.

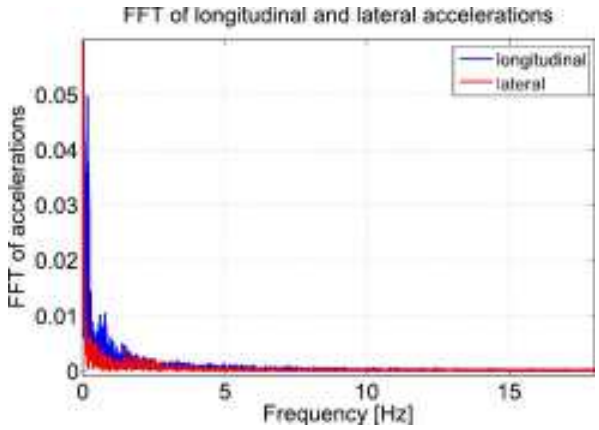

Figure 5.12: FFT of DM accelerations

Considering the same test, the FFT of the acceleration signals measured by IMU

shows a similar frequency content with an additional component around 10 Hz (Fig. 5.13): this is due to the dynamic properties of the sensor support, made through 3D printing in ABS material, assembles on the end-effector of the manipulator.

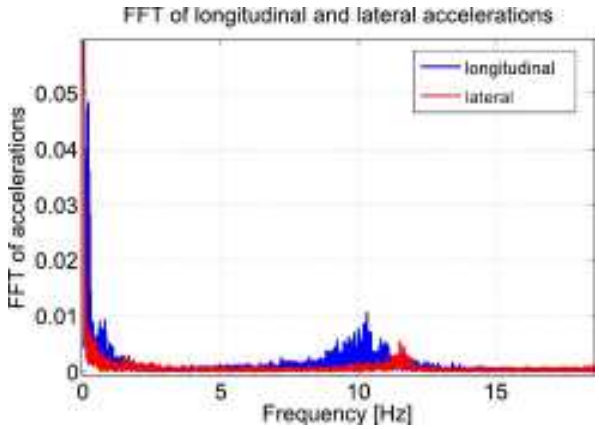

Figure 5.13: FFT of measured accelerations

In order to remove all the contributions of noise and of out-of-bandwidth vibrations, a Wavelet multi-resolution analysis has been applied to the gyro and acceleration measurements. The wavelet decomposition method [56] allows analyzing the measures in different frequency bands and, despite their spectra overlap, to separate noise from signal (*denoising*).

The first step of this procedure is to determine: a) the level of decomposition through a suitable criterion related to the nature of the signal, b) the specified mother wavelet (Haar, Daubechies, Coiflets, Symlet, Biorthogonal and etc.).

The second step is to use a threshold at each level to decide which coefficients should be passed through.

Finally the signal is reconstructed using the wavelet coefficients that have been passed through at each level.

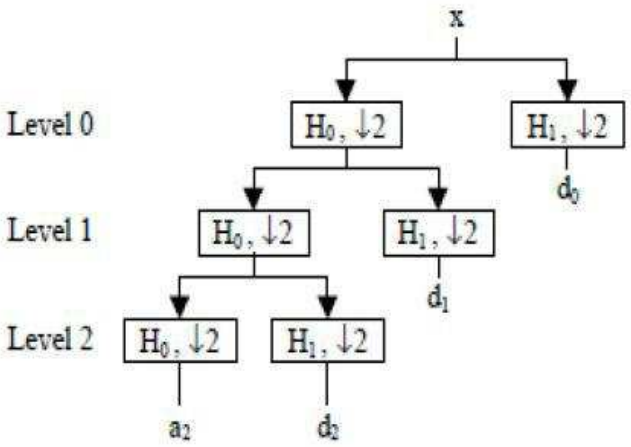

Figure 5.14: Wavelet decomposition

5.3 Results

A subset of ten paths obtained through the 3D multibody model explained in Sect. 3.1 have been used to perform the experimentation of the HIL test rig. The features of each path are described in the Tab. 5.3.

ID	Adhesion	Maneuver	WSP Anti-Skid	Curves	Altimetry	Irregularities
6	Good	Traction	Off	Straight	Level	Regular
42	Degraded	Braking	On	Straight	Level	Regular
45	Degraded	Braking	On	Straight	Level	Regular
59	Degraded	Braking	On	Curves	Uphill (3 %)	Regular
96	Degraded	Coasting	On	Curves	Level	Regular
102	Degraded	Traction	On	Straight	Level	Irregular
107	Degraded	Traction	On	Curves	Uphill (3 %)	Regular
108	Degraded	Traction	On	Curves	Downhill (3 %)	Regular
152	Good	Braking	On	Straight	Downhill (3 %)	Regular
156	Degraded	Traction	On	Straight	Uphill (2 %)	Regular

Table 5.3: Features of the testing paths

5.3.1 Accelerometers

In this section, for each path, the graphs of the longitudinal and lateral accelerations measured by the MTi-G compared to the reference signals are reported. Vertical components are not considered, according to the considerations in Sect. 4.3.3.

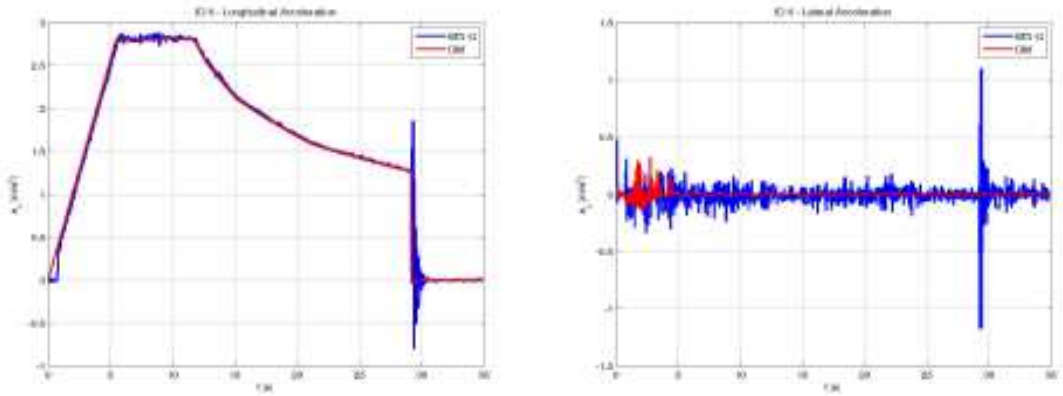

Figure 5.15: Path #6

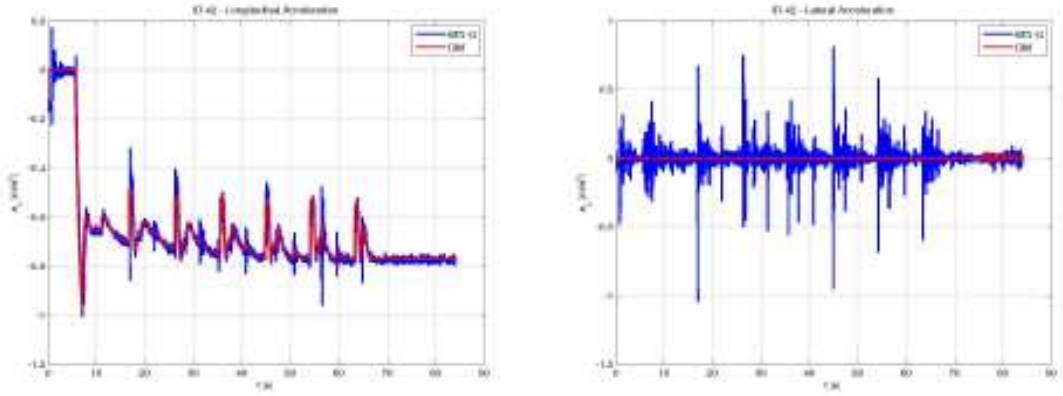

Figure 5.16: Path #42

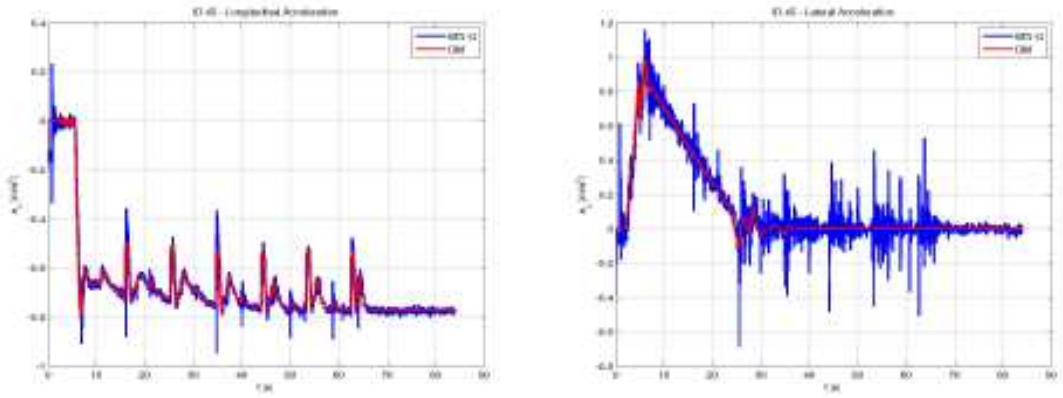

Figure 5.17: Path #45

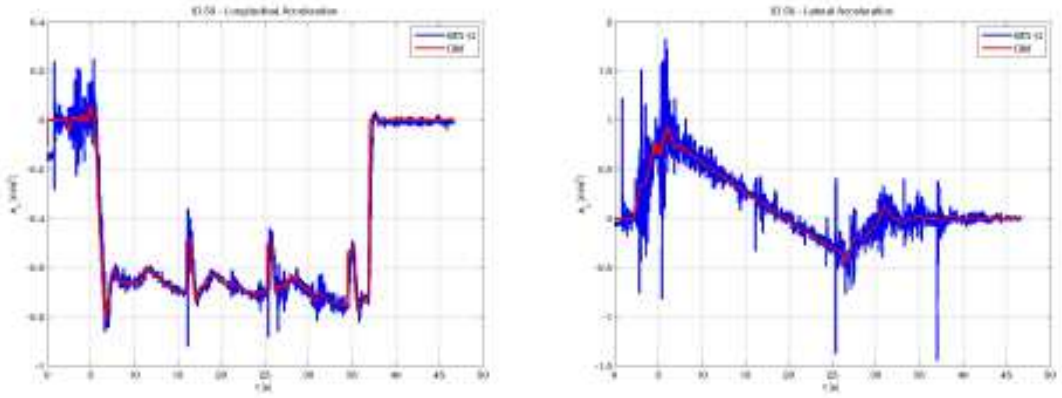

Figure 5.18: Path #59

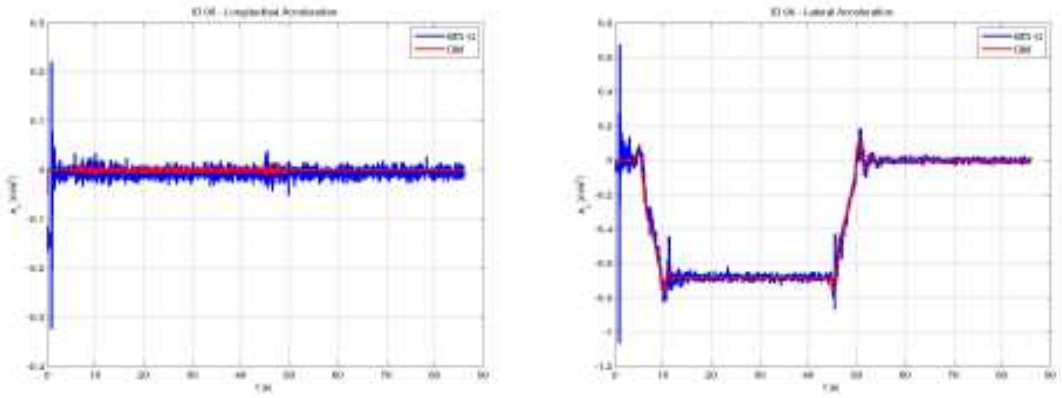

Figure 5.19: Path #96

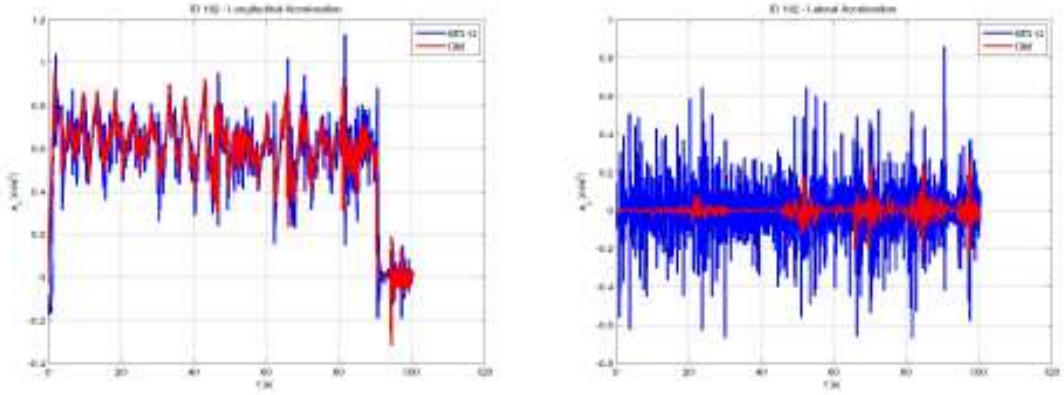

Figure 5.20: Path #102

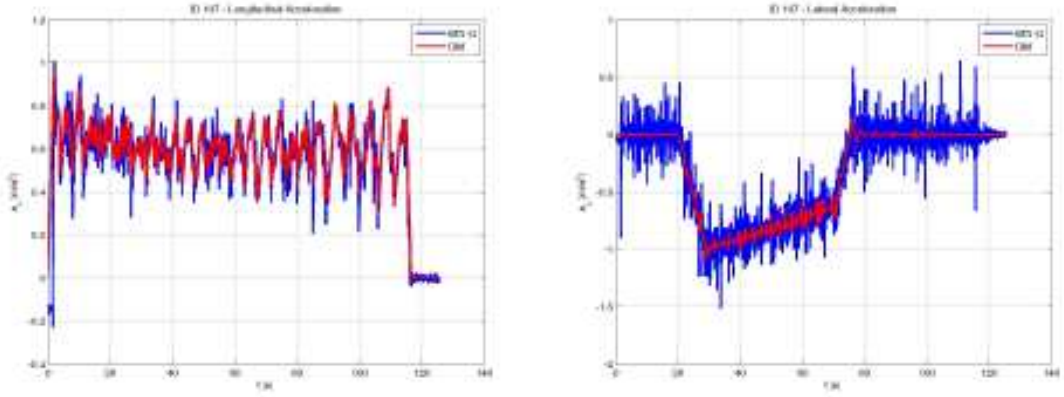

Figure 5.21: Path #107

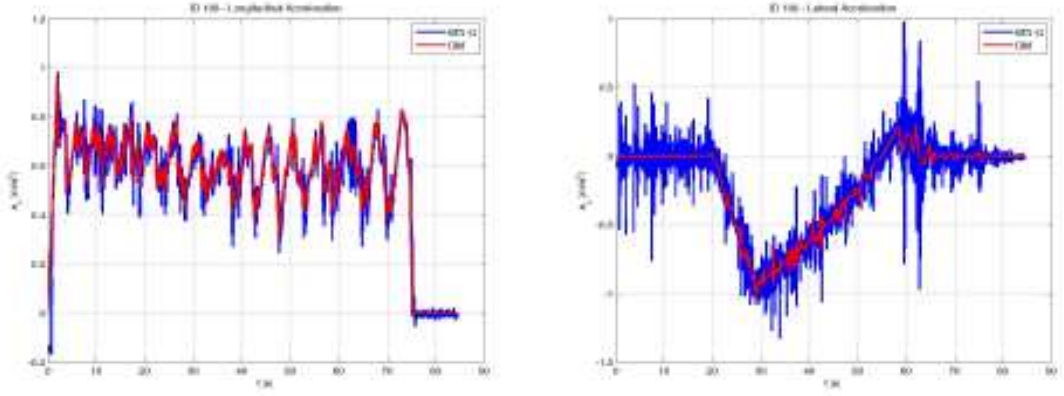

Figure 5.22: Path #108

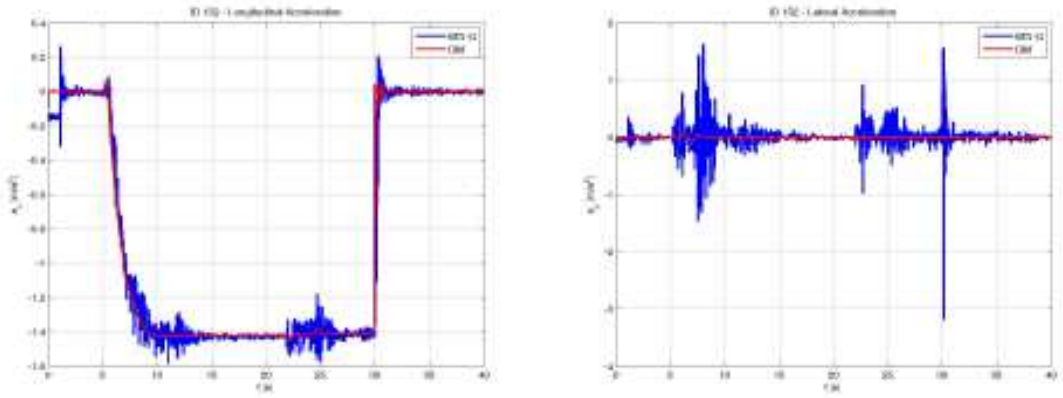

Figure 5.23: Path #152

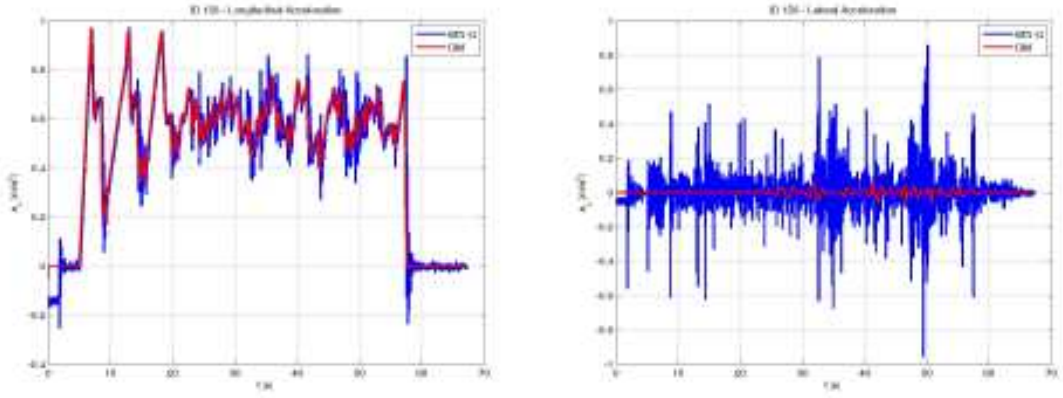

Figure 5.24: Path #156

Path	coord.	Lev.	Ord.	RMS
6	x	7	3	0.038
6	y	7	2	0.013
42	x	7	2	0.010
42	y	7	4	0.010
45	x	7	2	0.009
45	y	7	5	0.011
59	x	7	2	0.012
59	y	7	3	0.020
96	x	7	2	0.011
96	y	7	2	0.005
102	x	7	3	0.025
102	y	7	3	0.015
107	x	7	4	0.047
107	y	7	5	0.016
108	x	7	2	0.014
108	y	7	2	0.019
152	x	7	2	0.023
152	y	7	10	0.036
156	x	7	4	0.022
156	y	7	4	0.019

Table 5.4: RMS of the error time evolution - accelerometer

The Tab. 5.4, for each channel of each path, summarizes the level and the order of the wavelet decomposition and the RMS value of the time evolution of the error, defined as the difference between the acceleration reference signals and the post-processed analogous quantities measured by the MTi-G.

The RMS values are then shown in the histograms of Fig. 5.25 where it is possible to appreciate that the error for each component of acceleration is much less than the magnitude of the corresponding reference signal.

The achieved results confirm the validity of the proposed procedure as a method to reproduce the motion dynamic effects of a railway vehicle on inertial sensors, without introducing significant error sources that could make the system unsuitable for the proposed aim.

Same encouraging results have been performed for the gyroscopes as reported in Sect. 5.3.2.

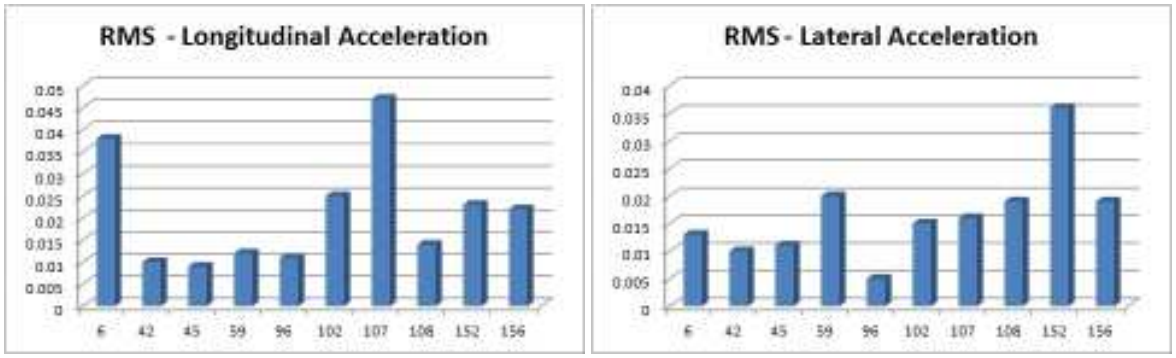

Figure 5.25: Histograms of RMS of the error time evolution - accelerometer

5.3.2 Gyroscopes

In the section, for each path, the graphs of the triaxial angular rates measured by the MTi-G compared to the reference signals are reported.

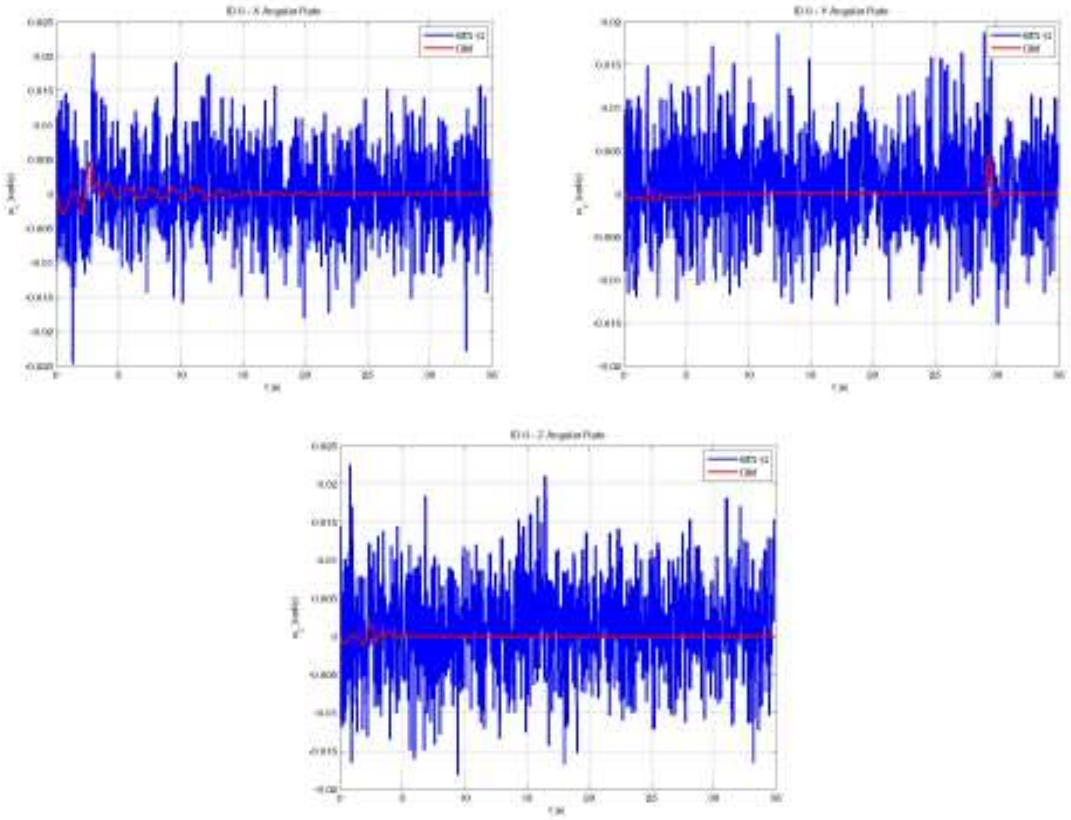

Figure 5.26: Path #6

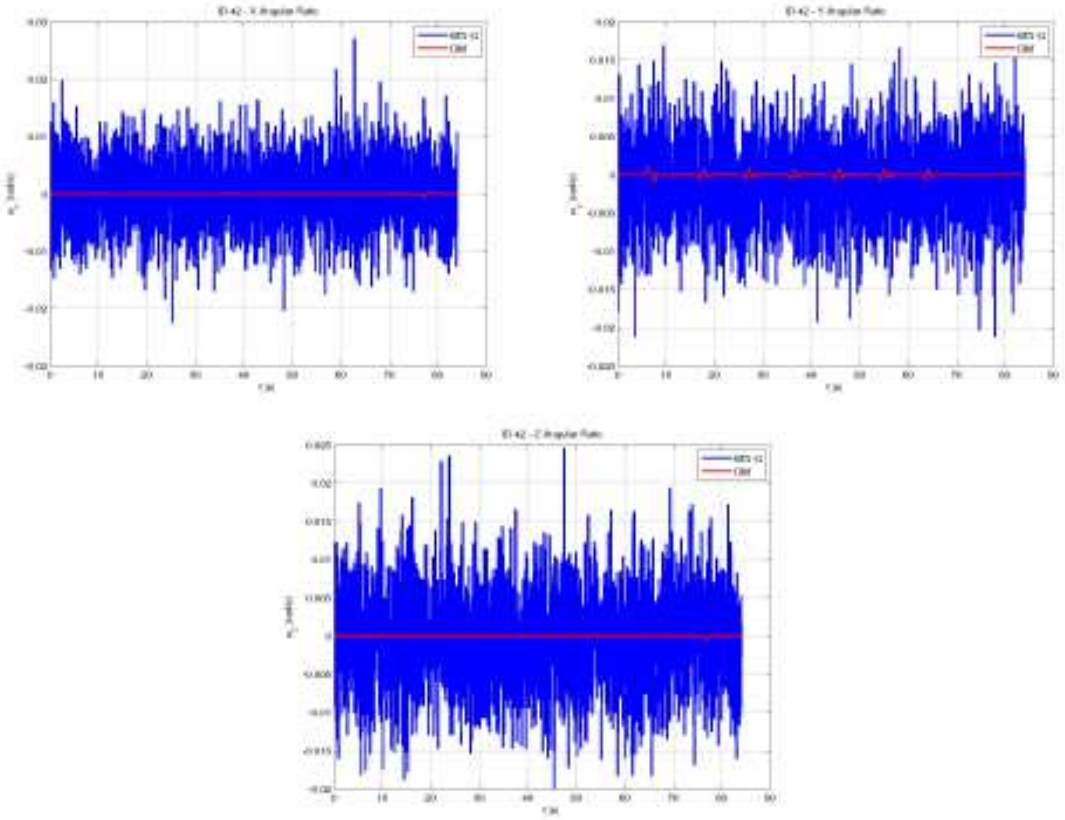

Figure 5.27: Path #42

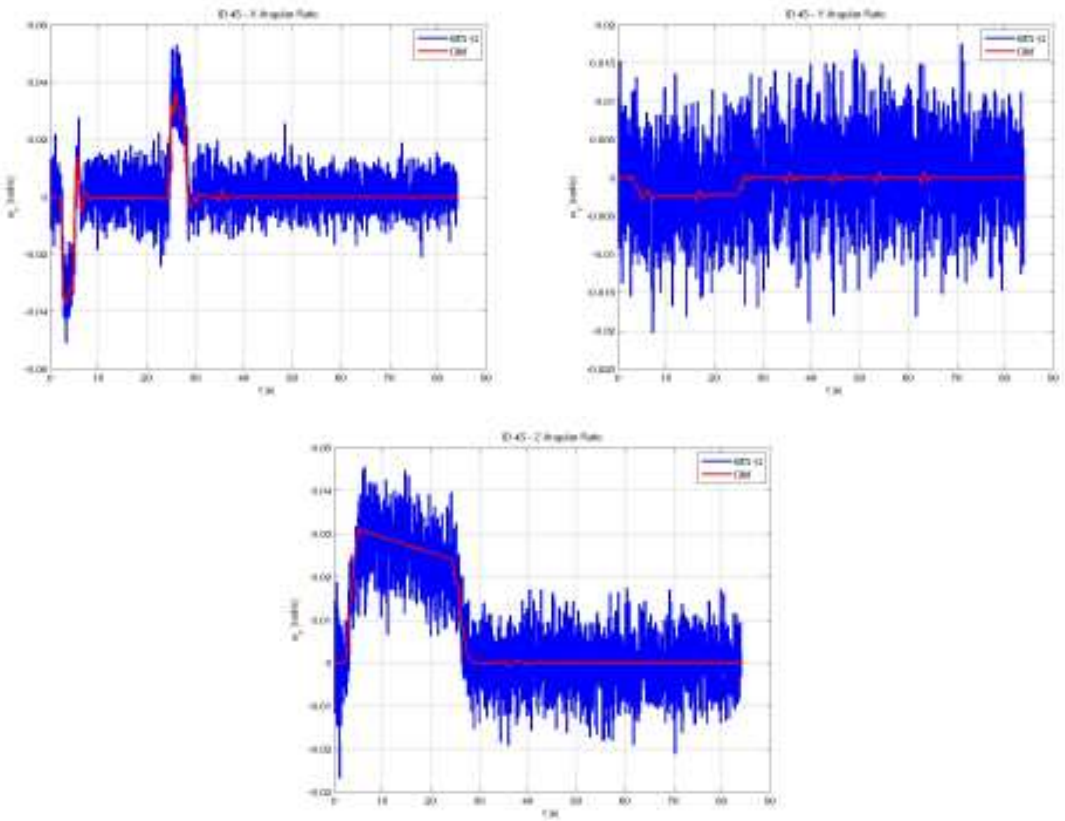

Figure 5.28: Path #45

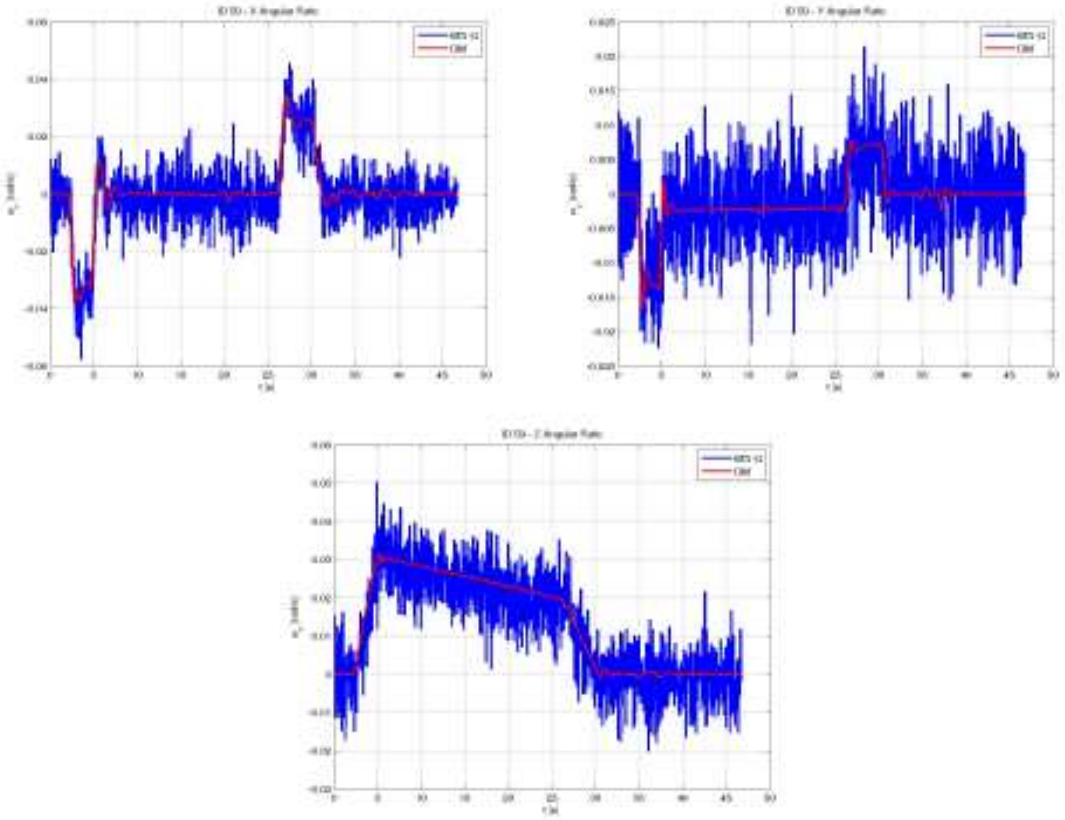

Figure 5.29: Path #59

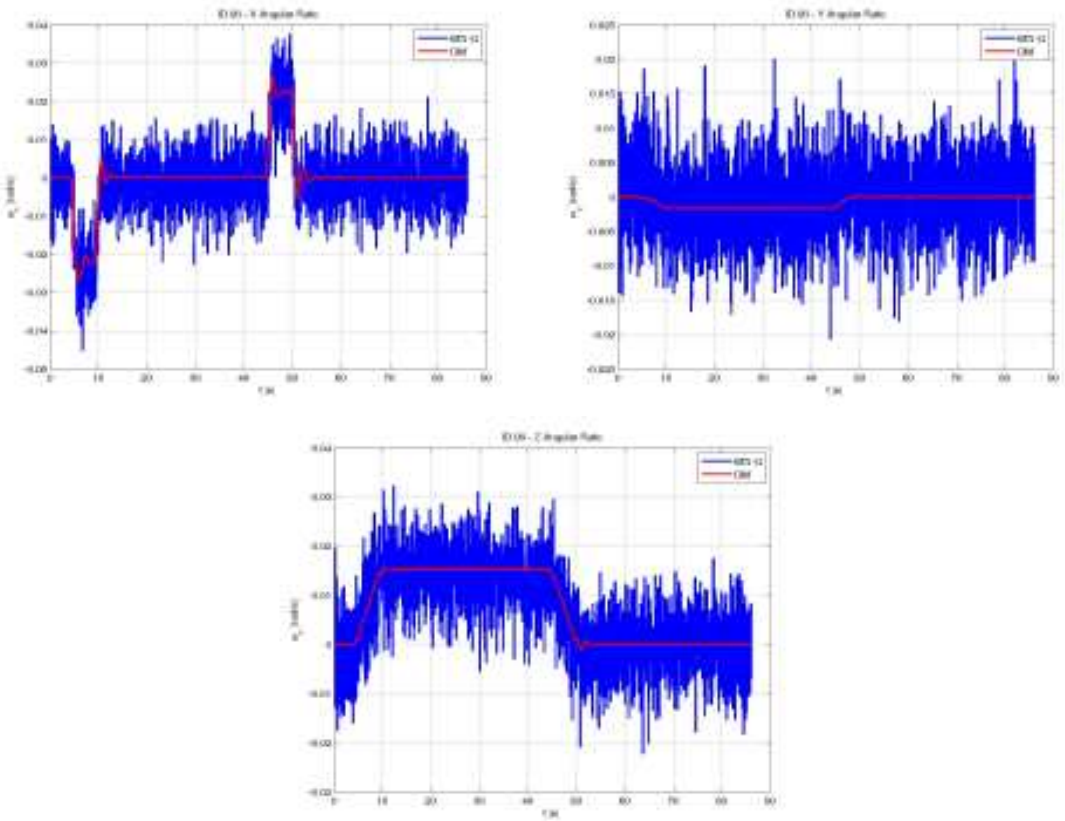

Figure 5.30: Path #96

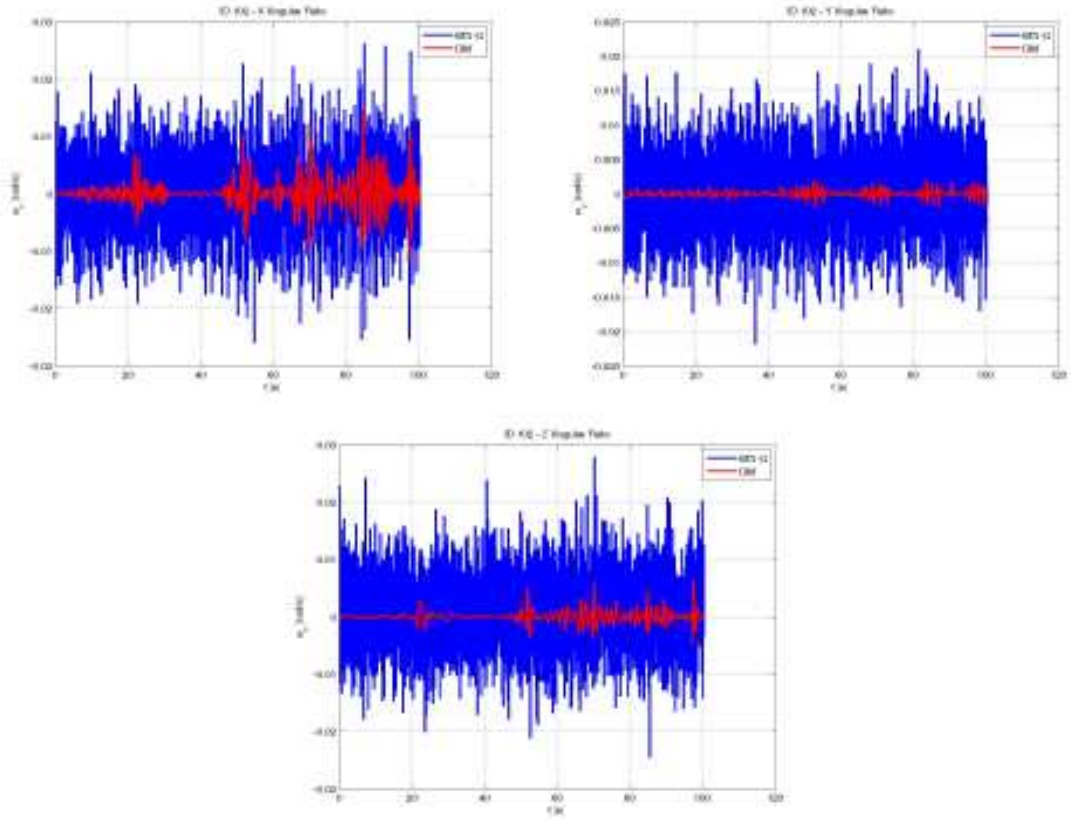

Figure 5.31: Path #102

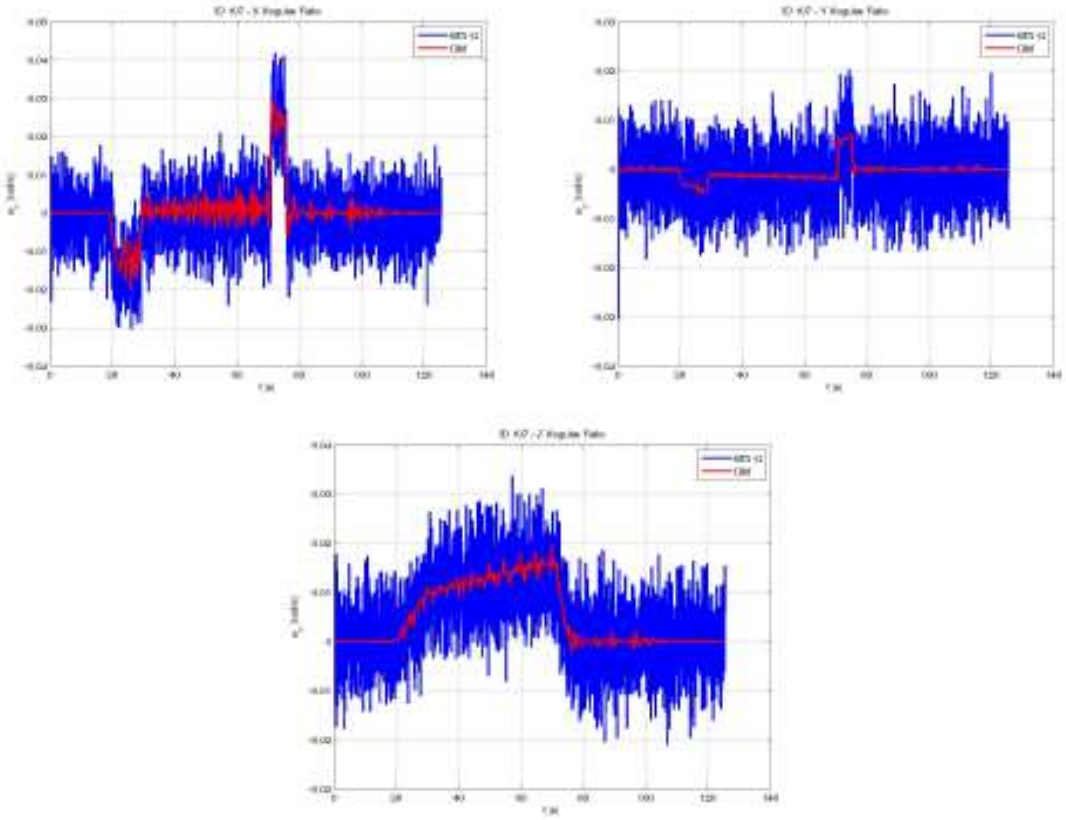

Figure 5.32: Path #107

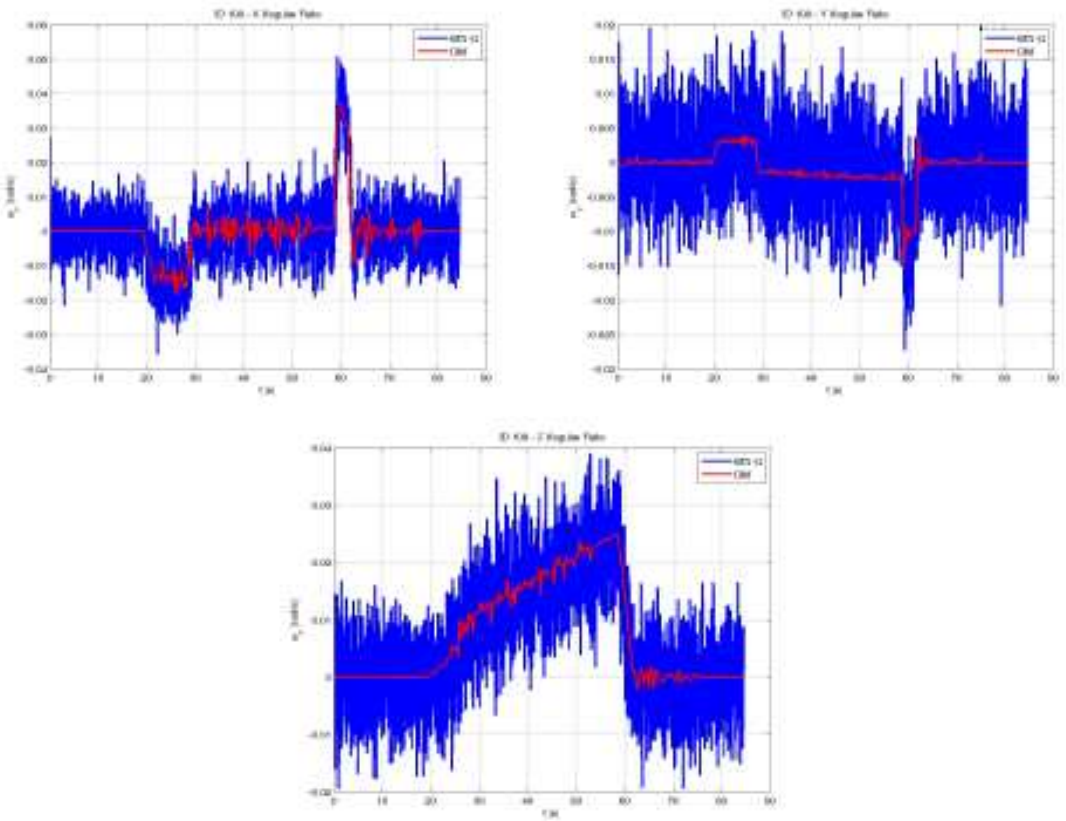

Figure 5.33: Path #108

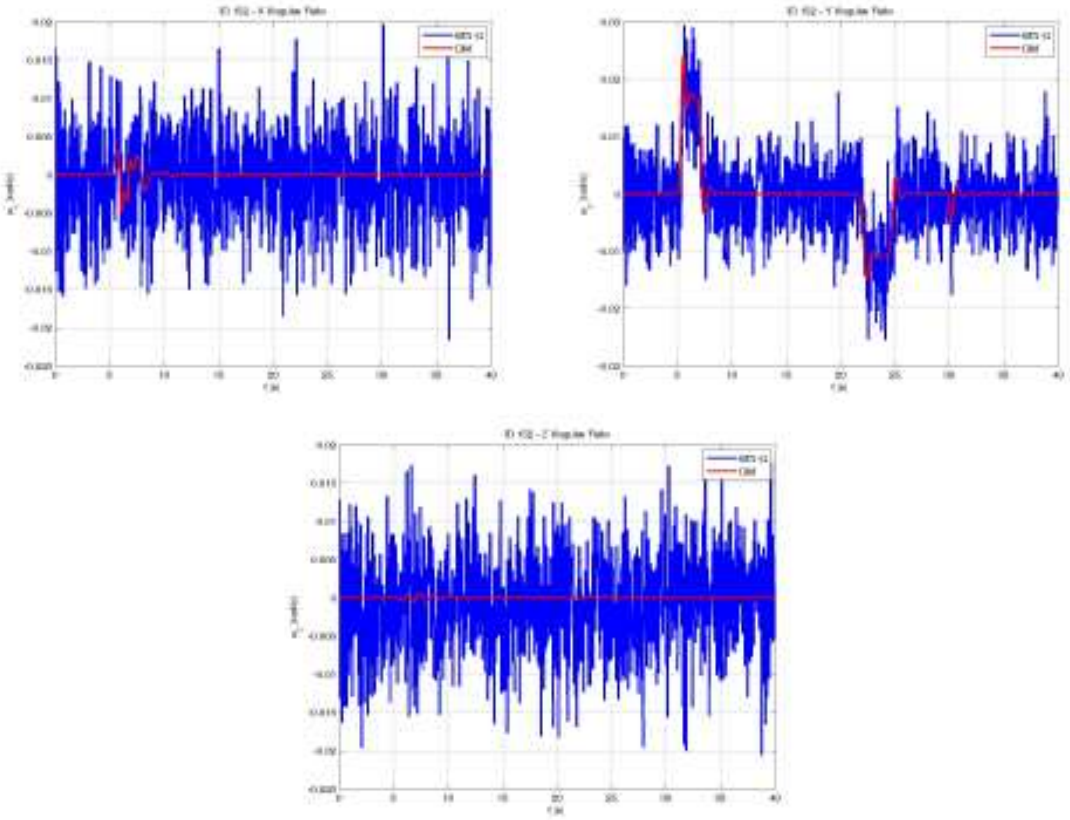

Figure 5.34: Path #152

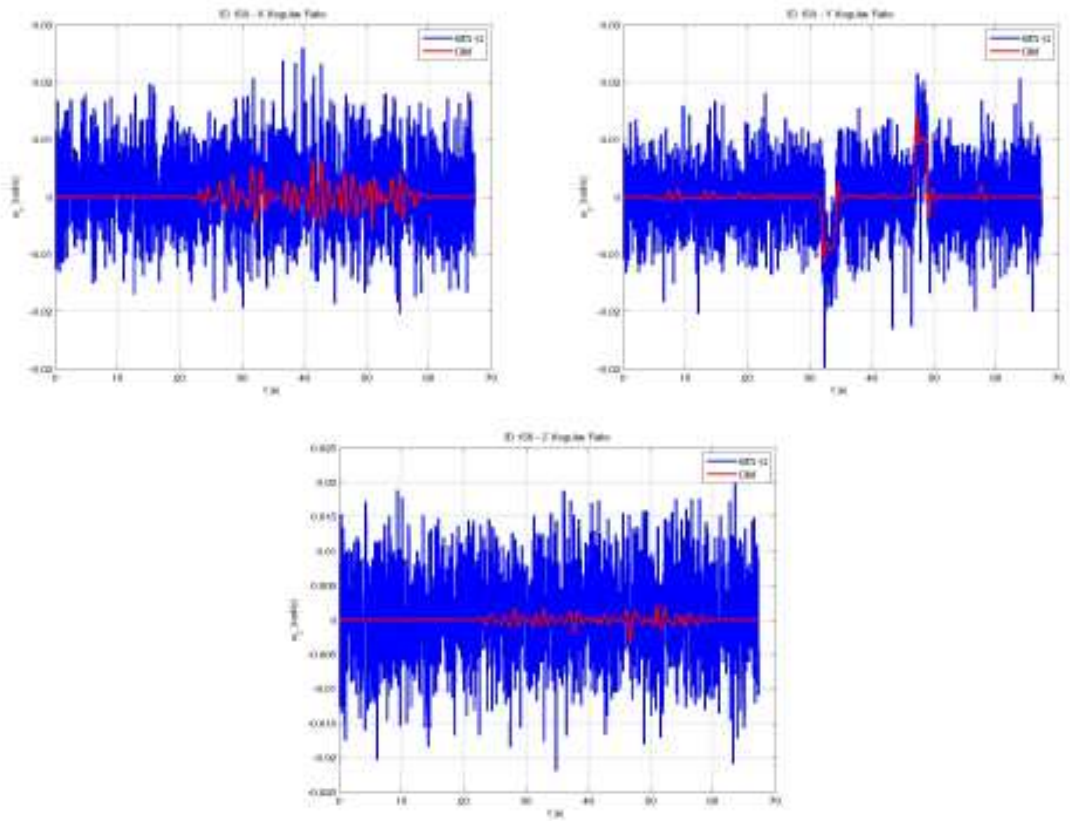

Figure 5.35: Path #156

Path	coord.	Lev.	Ord.	RMS
6	x	10	9	0.00055
6	y	11	4	0.00048
6	z	12	7	0.00026
42	x	12	4	0.00035
42	y	12	8	0.00129
42	z	12	10	0.00083
45	x	12	3	0.00128
45	y	12	5	0.00038
45	z	12	2	0.00090
59	x	12	7	0.0015
59	y	11	4	0.0004
59	z	9	10	0.0017
96	x	11	3	0.00138
96	y	12	7	0.00038
96	z	12	4	0.00129
102	x	12	3	0.00026
102	y	12	8	0.00019
102	z	11	5	0.00094
107	x	11	9	0.00160
107	y	12	6	0.00081
107	z	12	8	0.00065
108	x	11	10	0.00063
108	y	12	6	0.00050
108	z	12	10	0.00096
152	x	12	10	0.00096
152	y	12	3	0.00024
152	z	9	4	0.00166
156	x	9	2	0.00116
156	y	12	4	0.00056
156	z	12	8	0.00085

Table 5.5: RMS of the error time evolution - gyroscope

The Tab. 5.5, for each channel of each path, summarizes the level and the order of the wavelet decomposition and the RMS value of the time evolution of the error,

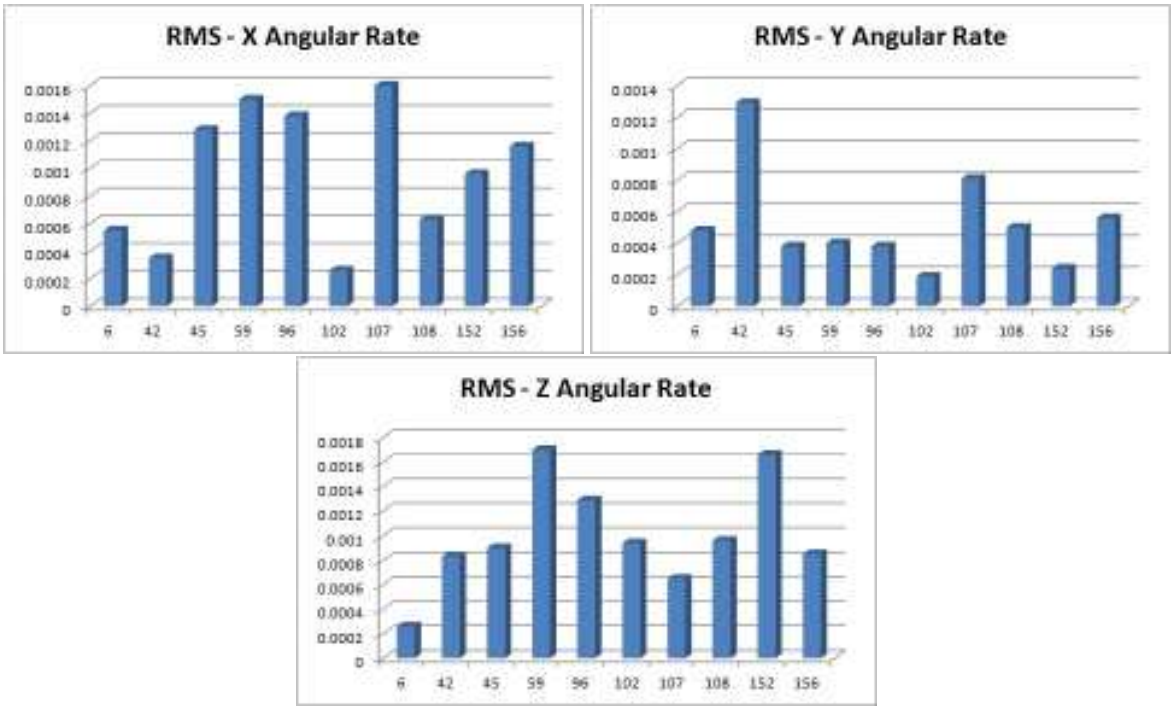

Figure 5.36: Histrogram of the RMS of the error time evolution - gyroscope

defined as the difference between the angular rate reference signals and the post-processed analogous quantities measured by the MTi-G.

The RMS values are then shown in the histograms of Fig. 5.36 where it is possible to appreciate that the error for each component of angular rate is much less than the magnitude of the corresponding reference signal.

As for the accelerometer, the achieved results confirm the validity of the proposed procedure and allow to say that the HIL test rig is well-functioning.

So the HIL dynamic simulator can be exploited as a method with general applicability for the testing of custom IMU boards, too.

Chapter 6

Testing of the innovative localization algorithm through the Dynamic Simulator

This chapter is focused on the activity of testing of the innovative localization algorithm designed as in Sect. 2.2. The first task is the project of a custom IMU which could fit both the technical and the business requirements: in fact the preliminary off-line simulations have proved that the performance requested by the inertial sensors (in particular by the gyroscope), in terms of noise and resolution, are high. On the other hand, ECM spa has driven a low-cost custom solution which could be integrated with the subsisting SCMT odometry module.

For these reasons a big effort has been spent in the marketing research of the most suitable devices and in the electronic project of a custom IMU. The design and the low level software project have been performed by ECM spa, so no deep details are provided in this dissertation.

The availability of a tested and well-functioning HIL test rig as dynamic simulator of the inertial sensors, and the availability of a custom IMU board have allowed to perform the testing of the innovative localization algorithm. In the last section of the current chapter the results are shown and commented.

6.1 Marketing research

In order to select the sensors that best suit the given requirements, a preliminary analysis must be carried out.

The characteristics which influence the choice of the sensor are:

- the amplitude of the measured signal;
- the bandwidth;
- the sensitivity;
- the operating conditions in terms of temperature;
- the cost.

Focusing initially on the choice of the accelerometer, it is essential to understand the kind of physical phenomenon that we want to measure: in fact, this instrument must be able to assess a longitudinal acceleration which, during acceleration and braking, do not exceed ±0.3g, and a lateral accelerations that, in curve, do not exceed the value of ±0.1g.

The third component depends on the slope of the track which can not ever be higher than 50 ‰: the value of the gravity (±g) could be a valid upper limit for the vertical acceleration, considering also that the contribution of pitch is negligible for this axis.

Since the measurements of the static accelerations is crucial for the application and, by the contrary, the high frequency vibrations are both relevant, the bandwidth of the sensor must be as small as possible and also must include the DC component.

About the other characteristics the choice must be to achieve and maximize sensitivity and operational conditions of use (particularly regarding the temperature range) and, above all, the cost of the component must be competitive for industrial purposes.

With regard to the gyroscope, the choice of the sensor is subject to the rate of change of the vehicle attitude: as regards the yaw rate, on a curved path the estimated maximum value is about ±5 °/s, while, about the roll rate, in consequence of the tilting on a overhead path, a maximum value of ±7 °/s.

The pitch angular velocity is supposed to have a maximum value of ±5 °/s, too. Even the gyro, as the accelerometer, must guarantee a bandwidth concentrated on low frequencies (from DC to a few Hz), high sensitivity and a good working for a wide range of temperatures.

6.1.1 Preliminary analysis for accelerometers

On the basis of the characteristics required, a marketing research was undertaken, in order to verify the requirements above describe matched with the items available on the market.

The marketing research has focused on the MEMS technologies that, in theory, provide cheaper costs and smaller sizes. To this purpose some catalogues of manufacturers of electronic components have been screened, such as Analog Devices and STMicroelectronics. The Tab. 6.1 shows a list of interesting models and their main characteristics.

Analog Devices opens up a wide range of MEMS accelerometers: both triaxial, both biaxial and uniaxial solutions. Essentially two series of models which differ both in cost and in size are available: the series ADXL includes analog and digital accelerometers with high performance, low power and small size; the series ADIS also provides a settable interface which allows a high precision working.

All accelerometers are of low-g type, i.e. they are suited for applications where small accelerations have to be measured. The analogue accelerometers provide a modulated voltage signal as output: it is manifest that a shorter range of measurement corresponds to a larger sensitivity. Being equal the range of measurement, a larger sensitivity is related to higher costs. On the other side, digital accelerometers provide I^2C or SPI bus communication systems as output format.

The supply current is another relevant parameter, since it is related to the power absorbed by the component. About the temperature range, it is quite large for every component.

Some of the models ADIS (ADIS16201, ADIS16203, ADIS16209) have the functionality of inclinometers: in fact the specification of the requirements is provided in degrees.

MEMS accelerometers provided by STMicroelectronics are both analogue and digital, both biaxial and triaxial. Most of the models gives the chance to set the value of the measuring range (e.g. the model LIS202DL between the values ±2g and ±8g). This tuning implies also a variation of the bandwidth values (e.g. for the model LIS202DL it could vary from 50 Hz to 200 Hz) and of the sensitivity of the instrument (as higher as smaller the measuring range).

All the models, however, guarantee the measurement of the static accelerations. The supply current ranges lie from 300 μA to 700 μA. The temperature range is uniform for all models. The average cost is approximately less than 10€. It is, however, worth to note that STMicroelectronics's products are more expensive than Analog Devices's, although the cost is related to the purchase of 1000 samples. The price difference arises from the larger sensitivity provided by STMicroelectronics's models, both analogue and digital.

It is worth to note that, only in the design phase of the electronic board, the hardware options involving the size, the electrical and communication interfaces, could be addressed.

Model	Manufacturer	# Axes	Range	Output Type	Bandwidth	Sensitivity
ADXL325	Analog Devices	3	±5g	Analog	5e-4 to 1.6[a] kHz	174 mV/g
ADXL326	Analog Devices	3	±16g	Analog	5e-4 to 1.6[a] kHz	57 mV/g
ADXL327	Analog Devices	3	±2g	Analog	5e-4 to 1.6[a] kHz	420 mV/g
ADXL335	Analog Devices	3	±3g	Analog	5e-4 to 1.6[a] kHz	300 mV/g
ADXL345	Analog Devices	3	±2/4/8/16g	Digital	5e-4 to 1.6[a] kHz	up to 256 LSB/g
ADXL346	Analog Devices	3	±2/4/8/16g	Digital	5e-4 to 1.6[a] kHz	up to 256 LSB/g
ADXL321	Analog Devices	2	±18g	Analog	5e-4 to 2.5[a] kHz	57 mV/g
ADXL103	Analog Devices	1	±1.7g	Analog	5e-4 to 2.5[a] kHz	1000 mV/g
ADXL203	Analog Devices	2	±1,7g	Analog	5e-4 to 2.5[a] kHz	1000 mV/g
ADIS16003	Analog Devices	2	±1.7g	Digital	1e-3 to 2.5[a] kHz	1.22 mg/LSB
ADIS16006	Analog Devices	2	±5g	Digital	1e-3 to 2.5[a] kHz	3.91 mg/LSB
ADIS16201	Analog Devices	2	±1.7g	Digital	1e-3 to 2.5 kHz	2.162 LSB/mg
ADIS16203	Analog Devices	1	±180°	Digital	1e-3 to 2.5[a] kHz	0.025 °/LSB
ADIS16209	Analog Devices	2	±90°/±180°	Digital	0.5 kHz	0.025 °/LSB
ADIS16240	Analog Devices	3	±18g	Digital	1.6(X,Y) 0.55(Z) kHz	51.4 mg/LSB
LIS202DL	STMicroelectronics	2	±2g/±8g	Digital	50 Hz/200 Hz	18-72 mg/digit
LIS244AL	STMicroelectronics	2	±2g	Analog	1e-3 to 2[a] kHz	420 mV/g
LIS244ALH	STMicroelectronics	2	±2g/±6g	Analog	1e-3 to 2[a] kHz	660-220 mV/g
LIS302DL	STMicroelectronics	3	±2g/±8g	Digital	50 Hz/200 Hz	18-72 mg/digit
LIS302SG	STMicroelectronics	3	±2g	Analog	1e-3 to 2[a] kHz	478 mV/g
LIS331AL	STMicroelectronics	3	±2g	Analog	1e-3 to 2[a] kHz	478 mV/g
LIS331DL	STMicroelectronics	3	±2g/±8g	Digital	50 Hz/200 Hz	18-72 mg/digit
LIS344AL	STMicroelectronics	3	±3.5g	Analog	1e-3 to 2[a] kHz	300 mV/g
LIS344ALH	STMicroelectronics	3	±2g/±6g	Analog	1e-3 to 2[a] kHz	660-220 mV/g
LIS3LV02DQ	STMicroelectronics	3	±2g/±6g	Digital	10/40/160/640 Hz	1024-340 LSB/g
LIS3LV02DL	STMicroelectronics	3	±2g/±6g	Digital	10/40/160/640 Hz	1024-340 LSB/g

[a]Adjustable band with variable capacity

Table 6.1: Marketing research for accelerometers

Model	Voltage Supply (V)	Current Supply (mA)	Noise Density	Temp Range	Sizes	Price
ADXL325	1.8 to 3,6	0.35	250 μ g/$\sqrt{\text{Hz}}$	-40 to 85°	4x4x1.45 mm	\$2.38[a]
ADXL326	1.8 to 3,6	0.35	250 μ g/$\sqrt{\text{Hz}}$	-40 to 85°	4x4x1.45 mm	\$2.38[a]
ADXL327	1.8 to 3,6	0.35	250 μ g/$\sqrt{\text{Hz}}$	-40 to 85°	4x4x1.45 mm	\$2.38[a]
ADXL335	1.8 to 3,6	0.35	300 μ g/$\sqrt{\text{Hz}}$	-40 to 85°	4x4x1.45 mm	\$2.38[a]
ADXL345	2 to 3,6	0.145	-	-40 to 85°	3x5x1 mm	\$3.04[a]
ADXL346	1.7 to 2.75	0.145	-	-40 to 85°	3x5x0.95 mm	N/A
ADXL321	2.4 to 6	0.49	320 μ g/$\sqrt{\text{Hz}}$	-20 to 70°	4x4x1.45 mm	\$8.13[a]
ADXL103	3 to 6	0.7	110 μ g/$\sqrt{\text{Hz}}$	-40 to 125°	5x5x2 mm	\$8.19[a]
ADXL203	3 to 6	0.7	110 μ g/$\sqrt{\text{Hz}}$	-40 to 125°	5x5x2 mm	\$9.85[a]
ADIS16003	3 to 5,25	1.5	-	-40 to 125°	7.2x7.2x1.7 mm	\$17.96[a]
ADIS16006	3 to 5,25	1.5	-	-40 to 125°	7.2x7.2x3.6 mm	\$17.96[a]
ADIS16201	3 to 3.6	11	-	-40 to 125°	9.2x9.2x3.9 mm	\$24.04[a]
ADIS16203	3 to 3.6	11	-	-40 to 125°	9.2x9.2x3.9 mm	\$24.04[a]
ADIS16209	3 to 3.6	11	-	-40 to 125°	9.2x9.2x3.9 mm	\$34.81[a]
ADIS16240	2.4 to 3.6	1	-	-40 to 105°	12x10x2.9 mm	\$26.58[a]
LIS202DL	2.5 to 3.3	0.4	-	-40 to 85°	5x3x0.92 mm	€6.32[b]
LIS244AL	2.4 to 3.6	0.65	220 μ g/$\sqrt{\text{Hz}}$	-40 to 85°	4x4x1.5 mm	€5.90[b]
LIS244ALH	2.4 to 3.6	0.68	50 μ g/$\sqrt{\text{Hz}}$	-40 to 85°	4x4x1.5 mm	€4.05[b]
LIS302DL	2.16 to 3.6	0.3	-	-40 to 85°	3x5x0.92 mm	€8.84[b]
LIS302SG	3 to 3.6	0.65	200 μ g/$\sqrt{\text{Hz}}$	-40 to 85°	3x5x0.9 mm	N/A
LIS331AL	3 to 3.6	0.65	300 μ g/$\sqrt{\text{Hz}}$	-40 to 85°	3x3x1 mm	€6.00[b]
LIS331DL	2.16 to 3.6	0.3	-	-40 to 85°	3x3x1 mm	€8.29[b]
LIS344AL	2.7 to 3.3	0.69	275 μ g/$\sqrt{\text{Hz}}$	-40 to 85°	4x4x1.5 mm	€4.25[b]
LIS344ALH	2.4 to 3.6	0.68	50 μ g/$\sqrt{\text{Hz}}$	-40 to 85°	4x4x1.5 mm	€5.05[b]
LIS3LV02DQ	2.16 to 3.6	0.65	-	-40 to 85°	7x7x1.8 mm	€14.51[b]
LIS3LV02DL	2.16 to 3.6	0.65	-	-40 to 85°	7.5x4.4x1 mm	€14.51[b]

[a] unit price of 1000 pieces
[b] unit price from *Mouser Electronics*

6.1.2 Preliminary analysis for gyroscopes

As regards the gyroscopes (see Tab. 6.2) Analog Devices's one have the same nomenclature as the accelerometers's, i.e. the series ADXL and ADIS.

ADIS sensors provide enhanced performance both in terms of accuracy (ADIS16120 is characterized by a very low noise, ADIS 16130 from a high accuracy) and functionality (ADIS16251, ADIS16260 and ADIS16265 are settable).

Most of the gyroscopes provide the desired performance (small measuring range, high sensitivity, low supply current, low bandwidth), although they are limited by the possibility of measuring only the rate around one axis.

STMicroelectronics provides a wider range of products compared to Analog Devices: in fact also two-axes devices are available and, even, a triaxial model.

For the reasons described in the sect. 6.2, the devices providing the smallest measuring range have been focused on: some models are able to tune the measuring range up to $\pm 30\ ^{\circ}/s$, with a consequent variation of the sensitivity.

The models are not different with each other about the values of supply current, bandwidth and range of temperatures.

Model	Manufacturer	# Axes	Range	Output Type	Bandwidth	Sensitivity
ADXRS610	Analog Devices	1	±300 °/s	Analog	1e-5 to 2.5[a] kHz	6 mV/°/s
ADXRS613	Analog Devices	1	±150 °/s	Analog	1e-3 to 3[a] kHz	12.5 mV/°/s
ADXRS614	Analog Devices	1	±50 °/s	Analog	1e-3 to 3[a] kHz	25 mV/°/s
ADXRS622	Analog Devices	1	±250 °/s	Analog	1e-5 to 2,5[a] kHz	7 mV/°/s
ADIS16060	Analog Devices	1	±80 °/s	Digital	1e-3 to 1[a] kHz	0.0122 °/s/LSB
ADIS16080	Analog Devices	1	±80 °/s	Digital	87e-5 to 0.04[a] kHz	0.098 °/s/LSB
ADIS16100	Analog Devices	1	±300 °/s	Digital	87e-5 to 0.04[a] kHz	0.244 °/s/LSB
ADIS16120	Analog Devices	1	±300 °/s	Analog	96e-4 to 0.32[a] kHz	0.2 °/s/mV
ADIS16130	Analog Devices	1	±250 °/s	Digital	68e-4 to 0.3[a] kHz	0.000042 °/s/LSB
ADIS16251	Analog Devices	1	±20 to ±80 °/s	Digital	Up to 0.05[a] kHz	0.00458 °/s/LSB
ADIS16260	Analog Devices	1	±80 to ±320 °/s	Digital	0.05 to 0.33[a] kHz	0.0183 °/s/LSB
ADIS16265	Analog Devices	1	±80 to ±320 °/s	Digital	0.05 to 0.33[a] kHz	0.0183 °/s/LSB
LYPR540AH	STMicroelectronics	3	±400/±1600 °/s	Analog	Up to 0.14[a] kHz	0.8/3.2 mV/°/s
LY503ALH	STMicroelectronics	1	±30/±120 °/s	Analog	Up to 0.14[a] kHz	33.3/8.3 mV/°/s
LPR403AL	STMicroelectronics	2	±30/±120 °/s	Analog	Up to 0.14[a] kHz	33.3/8.3 mV/°/s
LPR503AL	STMicroelectronics	2	±30/±120 °/s	Analog	Up to 0.14[a] kHz	33.3/8.3 mV/°/s
LPY403AL	STMicroelectronics	2	±30/±120 °/s	Analog	Up to 0.14[a] kHz	33.3/8.3 mV/°/s
LPY503AL	STMicroelectronics	2	±30/±120 °/s	Analog	Up to 0.14[a] kHz	33.3/8.3 mV/°/s

[a]Adjustable band with variable capacity

Table 6.2: Market research for gyroscopes

Model	Voltage Supply (V)	Current Supply (mA)	Noise Density	Temp Range	Sizes	Price
ADXRS610	4.75 to 5.25	3.5	0.05 mV/˚/s	-40 to 105˚	7.05x7.05x3.8 mm	$20.98[a]
ADXRS613	4.75 to 5.25	3.5	0.04 mV/˚/s	-40 to 105˚	7.05x7.05x3.8 mm	$20.98[a]
ADXRS614	4.75 to 5.25	3.5	0.04 mV/˚/s	-40 to 105˚	7.05x7.05x3.8 mm	$20.98[a]
ADXRS622	4.75 to 5.25	3.5	0.06 mV/˚/s	-40 to 105˚	7.05x7.05x3.8 mm	$20.98[a]
ADIS16060	4.75 to 5.25	6.5	0.04 ˚/s/$\sqrt{\text{Hz}}$	-40 to 105˚	8.2x8.2x5.2 mm	$35.37[a]
ADIS16080	4.75 to 5.25	7	0.05 ˚/s/$\sqrt{\text{Hz}}$	-40 to 85˚	8.2x8.2x5.2 mm	$35.37[a]
ADIS16100	4.75 to 5.25	7	0.1 ˚/s/$\sqrt{\text{Hz}}$	-20 to 85˚	8.2x8.2x5.2 mm	$35.37[a]
ADIS16120	4.75 to 5.25	95	0.015 ˚/s/$\sqrt{\text{Hz}}$	-40 to 85˚	36x42x14 mm	$636.55[a]
ADIS16130	4.75 to 5.25	73	0.0125 ˚/s/$\sqrt{\text{Hz}}$	-40 to 85˚	36x42x14 mm	$504.99[a]
ADIS16251	4.75 to 5.25	44	0.05 ˚/s/$\sqrt{\text{Hz}}$	-40 to 85˚	11.1x11.1x5.5 mm	$42.48[a]
ADIS16260	4.75 to 5.25	41	0.44 ˚/s/$\sqrt{\text{Hz}}$	-	11.1x11.1x5.5 mm	$42.48[a]
ADIS16265	4.75 to 5.25	41	0.44 ˚/s/$\sqrt{\text{Hz}}$	-40 to 125˚	11.1x11.1x5.5 mm	$56.57[a]
LYPR540AH	2.7 to 3.6	10.8	0.02 ˚/s/$\sqrt{\text{Hz}}$	-40 to 85˚	4.4x7.5x1.1 mm	N/A
LY503ALH	2.7 to 3.6	5	0.014 ˚/s/$\sqrt{\text{Hz}}$	-40 to 85˚	5x5x1.5 mm	€5.77[b]
LPR403AL	2.7 to 3.6	6.8	0.01 ˚/s/$\sqrt{\text{Hz}}$	-40 to 85˚	4x5x1 mm	€9.51[b]
LPR503AL	2.7 to 3.6	6.8	0.014 ˚/s/$\sqrt{\text{Hz}}$	-40 to 85˚	5x5x1.5 mm	€5.77[b]
LPY403AL	2.7 to 3.6	6.8	0.01 ˚/s/$\sqrt{\text{Hz}}$	-40 to 85˚	4x5x1 mm	€9.51[b]
LPY503AL	2.7 to 3.6	6.8	0.014 ˚/s/$\sqrt{\text{Hz}}$	-40 to 85˚	5x5x1.5 mm	€5.77[b]

[a] unit price of 1000 pieces
[b] unit price from *Mouser*

In order to identify the available on market sensors which better suite the odometry application in terms of quality/price ratio, a simulation of the performances of the algorithm is performed, according to the variation of the parameters of noise and sensitivity both for accelerometer and for gyroscopes.

At first, as regards the gyroscope, the index of performance is the time average of the estimation error of the angle of pitch (angle of main interest for the compensation of gravity).

According to the Tab. 6.2 only few sensors, which have passed a preliminary screening, have been included in the test.

The path used for this test is the #4 of the Tab. 3.5. The index of performance parameter is averaged on 10 tests.

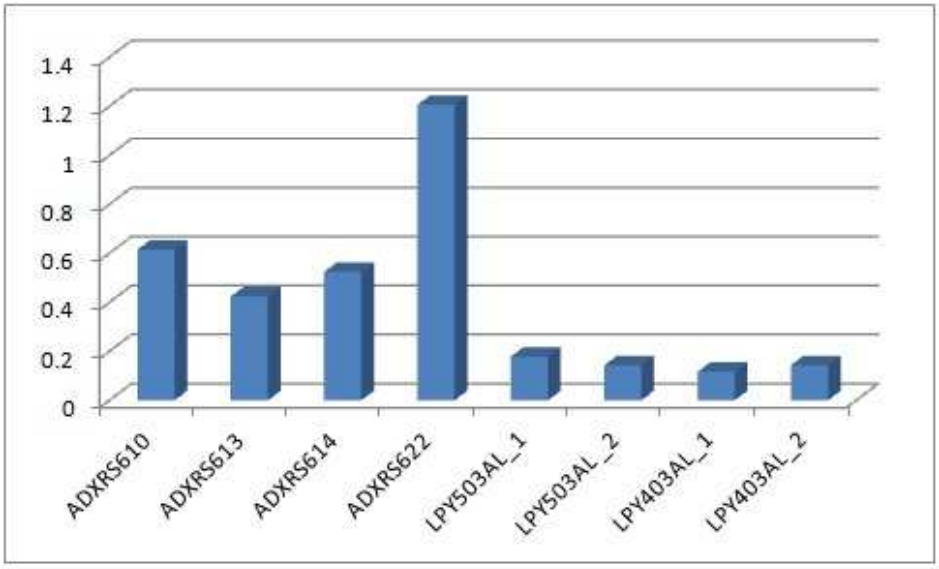

Figure 6.1: Trend of the performance parameter w.r.t. the model of the gyro

From Fig. 6.1 it is manifest that the best performance gyroscope is the model LPY403AL provided by STMicroelectronics.

With regard to the accelerometer, the assessment methodology of the best model is as the same as for the gyroscopes.

The parameter which is used to evaluate the performance of the sensors is the average over 10 tests of the time average of the train speed estimation.

The testing path used is yet the#4 of the Tab. 3.5; in order to decouple the speed estimation from the performance of the gyroscopes, the gravitational compensation is performed through the real pitch angle value and not exploiting the estimated one.

From Fig. 6.2 the model of accelerometer which shows best performance is the model LIS344ALH by STMicroelectronics.

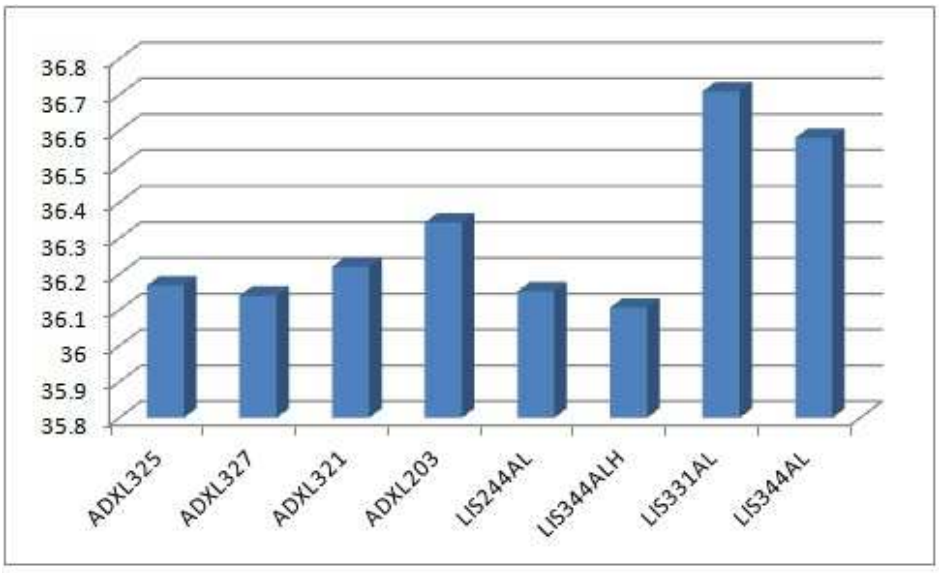

Figure 6.2: Trend of the performance parameter w.r.t. the model of the accelerometer

6.2 Electronic design

The IMU board supplied by ECM, as illustrated in Fig. 6.3, has been designed as a piggyback board to be assembled into the subsisting SCMT odometry module already included in the ECM's SSB*.

The piggyback is divided into two perfectly reflecting sections, in order to meet the reliability requirements which impose the redundancy of all the hardware and software structure.

In each section the following components lie:

- a triaxial accelerometer LIS344ALH by STMicroelectronics;
- two dual-axis gyroscopes LPY403AL by STMicroelectronics;
- a temperature sensor;
- three amplifiers (one for each inertial sensor);
- a μController.

The gyroscopes have been placed so that all the rates around the principal axes can be measured. The consequence of this arrangement is that the y-axis angular rate measurement (which affects the angle of pitch and so the slope of the line) is redundant. This choice is due to the lack on the market of low cost MEMS triaxial

*The motherboard handles the acquisition channel of the tachometers.

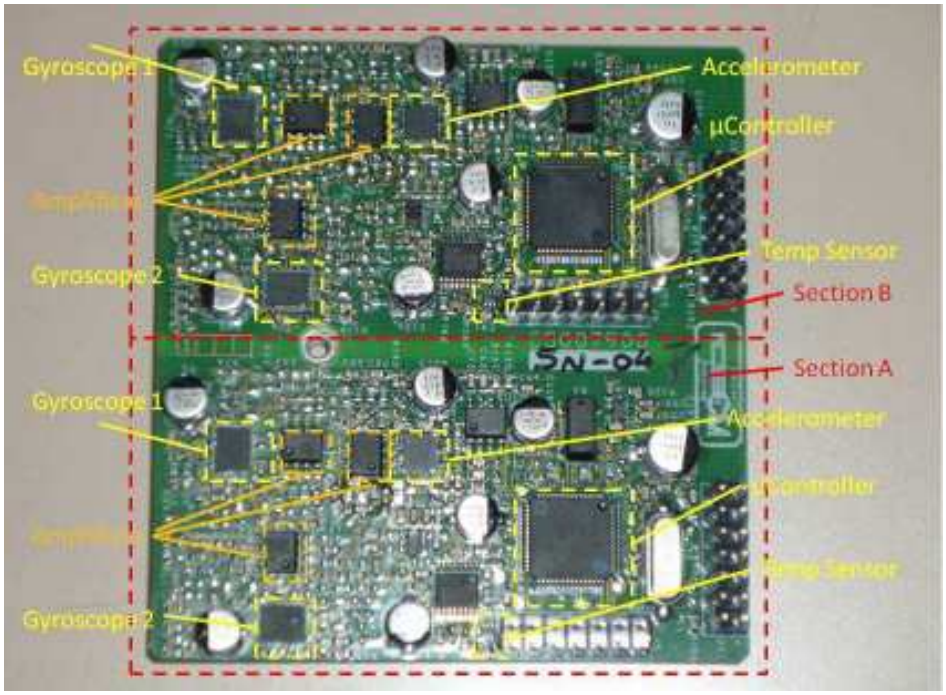

Figure 6.3: Layout of the piggyback design by ECM

gyro sensors able to meet the given requirements, in terms of density of noise, as identified in the previous section.

An aluminum plate has been designed (Fig. 6.4 and Fig. 6.5) for the accommodation of the whole odometry module (motherboard+piggyback). The plate has the specific purpose to be attached to the flange of the robot: in fact it is characterized by high stiffness, so as any vibrations cannot overlap the acceleration signal.

Figure 6.4: Design of the aluminum plate - front

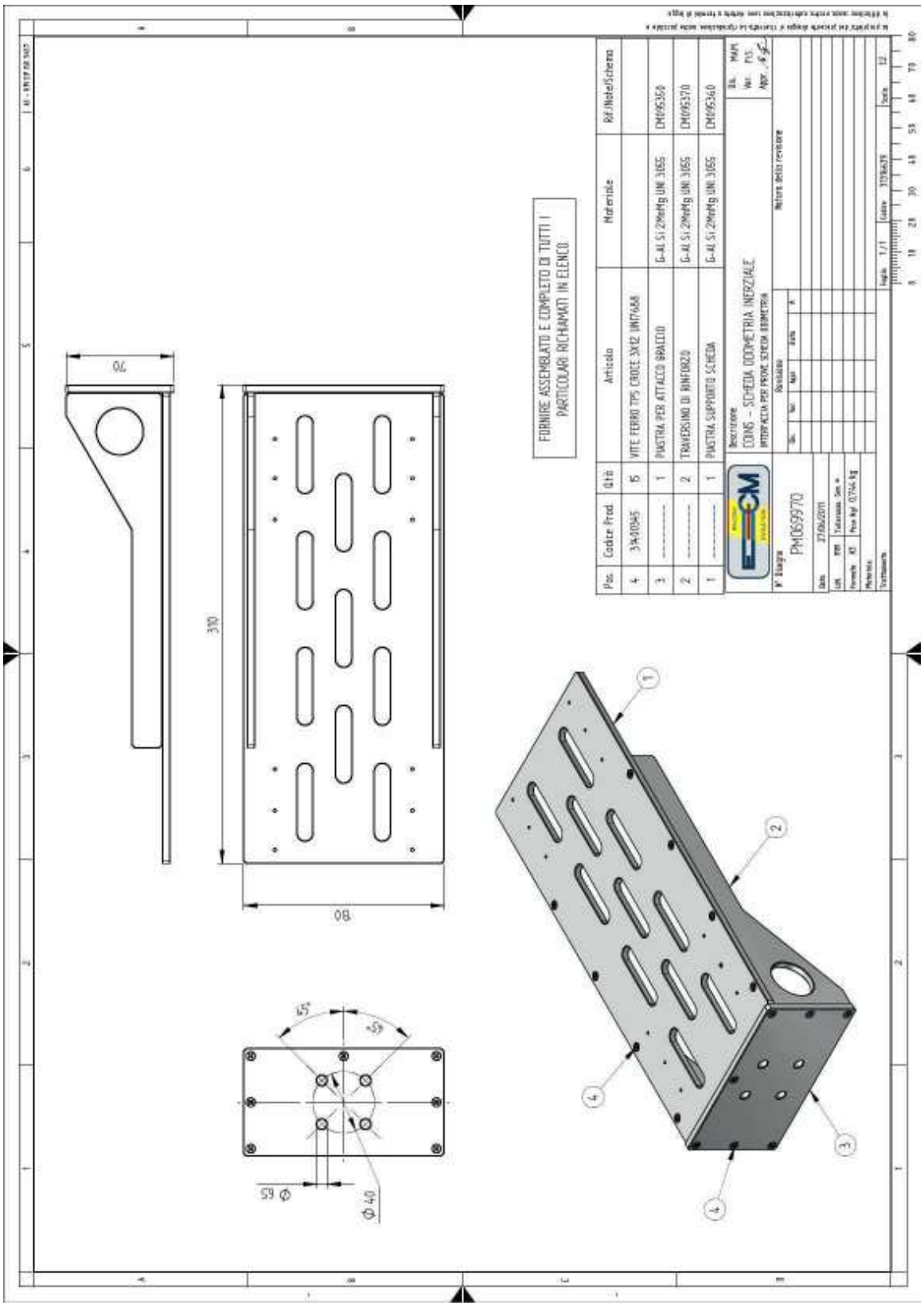

Figure 6.5: Design of the aluminum plate - rear

The assembling of the module on the robot is such that its orientation is the same as in the train cabinet (Fig. 6.6).

Figure 6.6: Custom odometry module assembled on the robot

The sensors are supplied at 3 V. The amplifier is aimed to the preamplification of the analog output of the sensors. Moreover the board houses a 12 bit AD converter for the digitalization of the signal. So, the measuring range could no longer correspond to the nominal one described in the datasheets of the sensors, but it could be adapted to a range of interest (see Sect. 6.1).

6.2.1 Study of the preamplification impact

The following analysis is aimed to evaluate the impact of a preamplification in terms of Signal-Noise Ratio (SNR) of the sensor outputs.

Starting from the accelerometer, the following features are pointed out:

- range ± 2g
- Vdd=3V
- Uncertainty on 0g level Vdd/2 ± 5% (1.425 ÷ 1.575 V)
- 0g level change Vs Temperature (Delta from +25 ˚C) ± 0.4 mg/˚C
- Sensitivity change Vs Temperature (Delta from +25 ˚C) ±0.01 %/˚C
- Operating temperature range -25˚C ÷ +55˚C
- Noise spectral density 50 μg/$\sqrt{\text{Hz}}$

	No gain	**gain 8V/V**
0g level change (@-25°C ÷ @ 55°C)	-12 mV ÷ 7.2 mV	-96 mV ÷ 57.6 mV
Total 0g level change	**19.2 mV**	**153.6 mV**
Sensitivity (S0) Vdd/5	0.6 V/g	4.8V/g
S0 (@-25°C ÷ @ 55°C)	597 ÷ 601.8 mV/g	4.776 ÷ 4.8144 V/g
ΔS0 (Delta from +25 °C)	-3 ÷ +1.8054 mV/g	-24 ÷ +14.4 mV/g
ΔS0 (@ ±0.3g)	-0.9 mV ÷ +0.54162 mV	-7.2mV ÷ +4.32 mV
Total ΔS0 (@ ±0.3g)	**1.44162 mV**	**11.52 mV**
Noise spectral density	83 $\mu g/\sqrt{Hz}$	240 $\mu g/\sqrt{Hz}$
Noise RMS (@ 10 Hz)	95 μVrms 158 μg	760 μVrms 158 μg
LSB	976 μg	152 μg

Table 6.3: Effect of the preamplification on the accelerometer

Considering the digitalized output signal in counts (1 count = 1 LSB), two considerations arises from the data in the table:

1. the influence of the sensitivity and 0g errors compared to the signal is lower in the "gain 8V/V" case (a=0.3g):

$$\begin{aligned} \frac{\Delta S0a + \Delta 0g}{S0a} &= \\ &= \frac{2+32}{307} = 11.4\% \qquad \text{(no gain)} \\ &= \frac{15+210}{1973} = 11.7\% \qquad \text{(gain 8V/V)} \end{aligned} \tag{6.1}$$

2. the "gain 8V/V" SNR is significantly greater than "no gain":

$$\begin{aligned} \frac{S0a}{\text{RMSnoise}} &= \\ &= \frac{307}{1} = 307 \qquad \text{(no gain)} \\ &= \frac{1973}{5} = 394 \qquad \text{(gain 8V/V)} \end{aligned} \tag{6.2}$$

As regards the gyroscopes, the features are:

- range ± 120 ˚/s
- Vdd=3V
- 0-rate level change Vs Temperature (Delta from +25 ˚C) 0.02 ˚/s/˚C
- Sensitivity change Vs Temperature (Delta from +25 ˚C) 0.07 %/˚C
- Operating temperature range -25˚C ÷ +55˚C
- Noise spectral density 0.01 ˚/s/$\sqrt{\text{Hz}}$

	No gain	**gain 36V/V**
0-rate level change (@-25˚C ÷ @ 55˚C)	-12.8152 mV ÷ 13.55888 mV	-298.8mV mV ÷ 179.28 mV
Total 0-rate level change	**13.28 mV**	**478.08 mV**
Sensitivity (S0) Vdd/5	8.3 mV/˚/s	298.8 mV/˚/s
S0 (@-25˚C ÷ @ 55˚C)	8.0095 ÷ 8.4743 mV/˚/s	288.342 ÷ 305.0748 mV/˚/s
ΔS0 (Delta from +25 ˚C)	-0.2905 ÷ +0.1743 mV/˚/s	-10.458 ÷ 6.2748 mV/˚/s
ΔS0 (@ ±5 ˚/s)	-1.4525 mV ÷ +0.8715 mV	-52.29 mV ÷ +31.374
Total ΔS0 (@ ±5 ˚/s)	**2.324 mV**	**83.664 mV**
Noise spectral density	83 μV/$\sqrt{\text{Hz}}$	298.8 μV/$\sqrt{\text{Hz}}$
Noise RMS (@ 10 Hz)	262 μVrms	9.448 mVrms
LSB	0.058 ˚/s	0.0025 ˚/s

Table 6.4: Effect of the preamplification on the gyroscope

Performing the same analysis as for the accelerometers, the same considerations arise, too:

1. the influence of the sensitivity and 0-rate errors compared to the signal is lower in the “gain 36V/V” case (ω=0.5 ˚/s):

$$\begin{aligned} \frac{\Delta S0\omega + \Delta 0 - \text{rate}}{S0\omega} &= \\ &= \frac{27+11}{86} = 44\% \qquad \text{(no gain)} \\ &= \frac{640+112}{2000} = 37.6\% \qquad \text{(gain 36V/V)} \end{aligned} \tag{6.3}$$

2. the “gain 3V/V” SNR is significantly grater than “no gain”:

$$\begin{aligned} \frac{S0\omega}{\text{RMSnoise}} &= \\ &= \frac{86}{1} = 86 \qquad \text{(no gain)} \\ &= \frac{2000}{12} = 166 \qquad \text{(gain 36V/V)} \end{aligned} \tag{6.4}$$

Both analysis point out the benefits of the preamplification exploiting.

6.2.2 Software Interface

The custom board can transfer the output data through a USB cable, RS-232 protocol. In order to get the data in a general purpose host, ECM has designed a tool based on the MFC-Windows library and on FTDI drivers[†], Fig. 6.7.

Figure 6.7: Screenshot of the tool AccOdo

The tool has a configuration mask where the user can select the COM port and the baudrate. The main window contains a box for each channel of data acquisition where it flows the outputs of both accelerometer and the gyroscope.

In the upper boxes, at left (box "Range") a led reports if the reading is correct or out-of-scale; on its right the box "CRC KO" reports the corruption of the packet of data; then the box "Temperatura" indicates the measured temperature value; in

[†]http://www.ftdichip.com/index.html

the end the box “Log File” can enable the logging in a .txt file, in consequence of the tick of the box “Enable Log”.

6.3 Calibration and thermal analysis

This section deals with the procedure for the calibration of the custom IMU board for the removal of the sensor errors. Compared to the MTi-G, no thermal compensation is provided by the components, so it is fundamental to seek the output drift due to a temperature gradient.

At first, it is necessary to define a procedure to decouple the output error of the IMU ($\Delta 0_g{}^{imu}$) in the component due to an assembly misalignment ($\Delta\eta$), the drift based on the temperature $\Delta 0_g(T)$ and other intrinsic biases $\Delta\bar{0}_g$.

$$\Delta 0_g{}^{imu} = \Delta\eta + \Delta 0_g(T) + \Delta\bar{0}_g \tag{6.5}$$

The strategy exploits a MTi Xsens placed at the rear of the board, in the position exposed in Fig. 6.8, as reference for the output measurements.

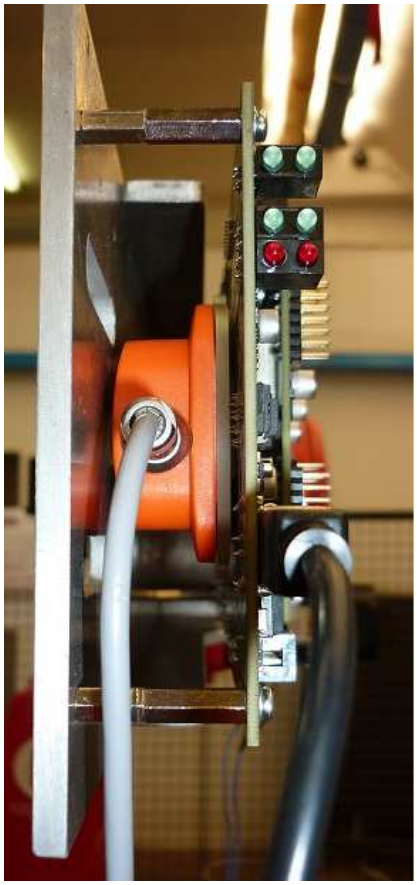

Figure 6.8: MTi Xsens fixed w.r.t. the custom board

The first step is the definition of some frames on the custom board: in Fig. 6.9 the MTi reference frame and the accelerometer reference frame are shown.

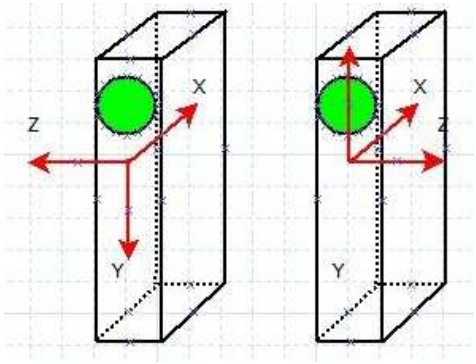

Figure 6.9: Mti (left) and accelerometer (right) reference frame

Since the amplifiers are inverting, if the amplification is active, each axis of the accelerometer reference frame is inverted: the new reference frame is left-hand. so a need of attention is essential to care the right configuration. In fig. 6.10 the latter frame is represented (on the left), while, on the right, the train reference frame is shown.

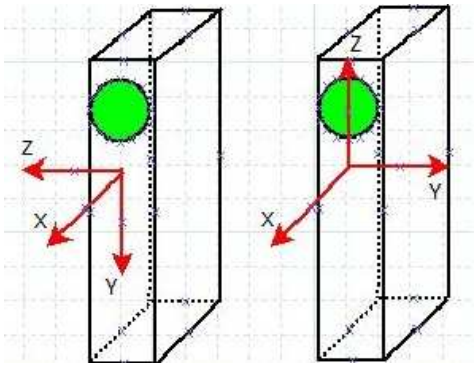

Figure 6.10: Inverted accelerometer (left) and train (right) reference frame

The aim of the Xsens is to provide a reliable measure of acceleration to be used as estimation of the assembly error: in fact it is calibrated in temperature and the assumption in Eq. 6.6 is given for each axis.

$$\Delta\eta = \Delta 0_g{}^{xsens} \tag{6.6}$$

In order to characterize the behaviour of the acceleration in temperature and determinate $\Delta 0_g(T)$ several tests in the climatic chamber inside ECM spa were carried out (see Fig. 6.11). The temperature has been varied from -25 °C to + 55 °C with gradient of 2 °C.

The next assumption is to consider negligible the contribution of the intrinsic error, $\Delta\bar{0}_g$=0. So, by the measurements from the MTi ($\Delta 0_g{}^{xsens}$) and the custom

Figure 6.11: Climate chamber tests

IMU board ($\Delta 0_g{}^{imu}$) it is possible to calculate the output error related to the temperature:

$$\Delta 0_g(T) = \Delta\eta - \Delta 0_g{}^{imu} \tag{6.7}$$

The following graphs report the trend of the $\Delta 0_g(T)$ for longitudinal and lateral components of the accelerometer (Fig. 6.12) and for the three components of the gyroscope (Fig. 6.13).

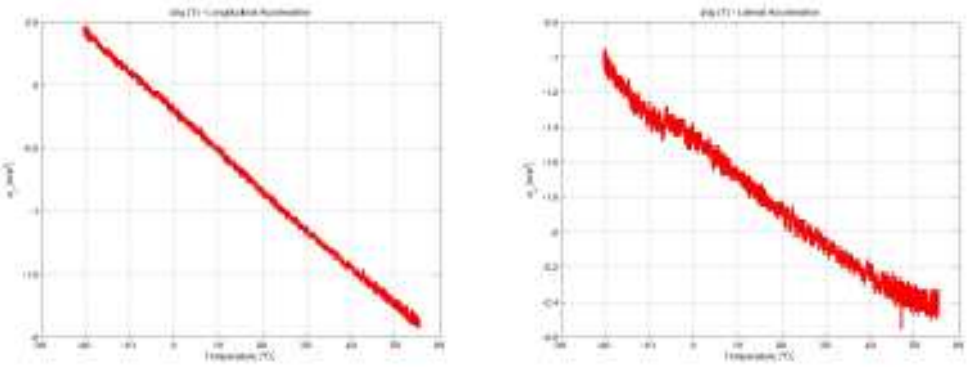

Figure 6.12: Trend of the accelerometer offset w.r.t. temperature

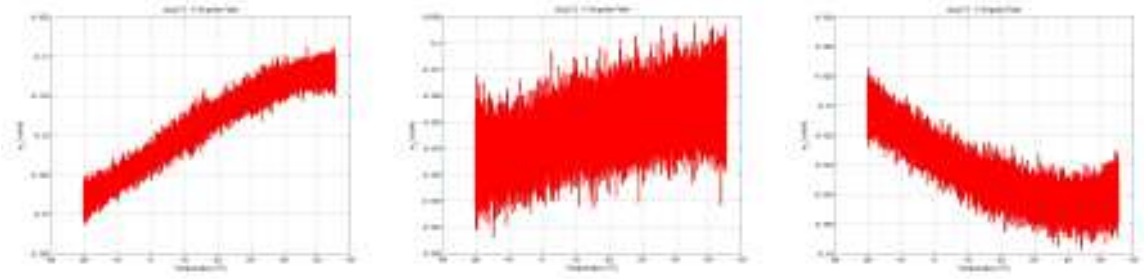

Figure 6.13: Trend of the gyroscope offset w.r.t. temperature

The validation of the assumption about the intrinsic error is verified in the IMU custom testing phase, described in the next section.

6.4 Testing of the custom IMU

6.4.1 Accelerometers

In this section the graphs of the longitudinal and lateral accelerations measured by the custom IMU board are compared to the reference signals, i.e. the ten paths described in the Tab. 5.3.

For each figure the following signals have been reported:

- the reference signal generated by the DM (3D multibody model) - red line;
- the raw measurement of the custom IMU board - black line;
- the calibrated measurement of the custom IMU board, i.e. the raw one compensated through the temperature-based offset - blue line;

The lower subplot sketches the error between the reference signal and the calibrated measurement, in order to find the value of the residual offset.

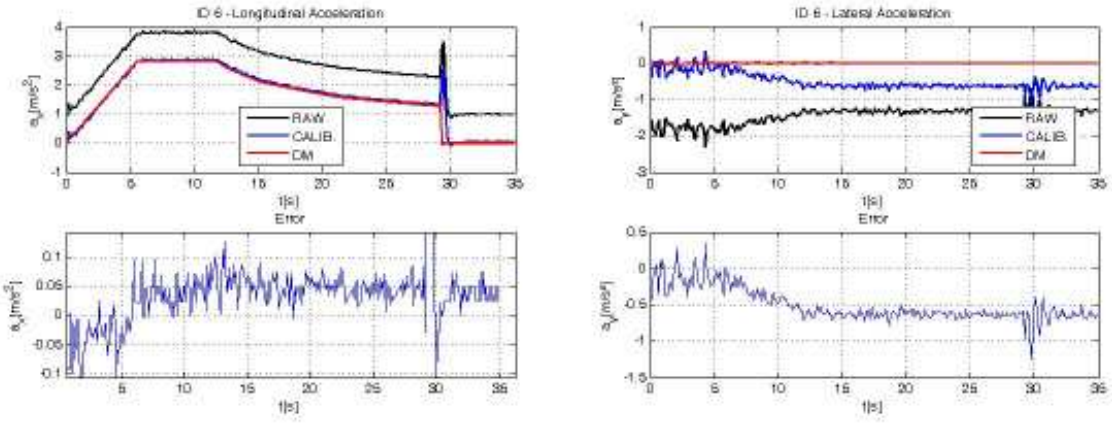

Figure 6.14: Path #6

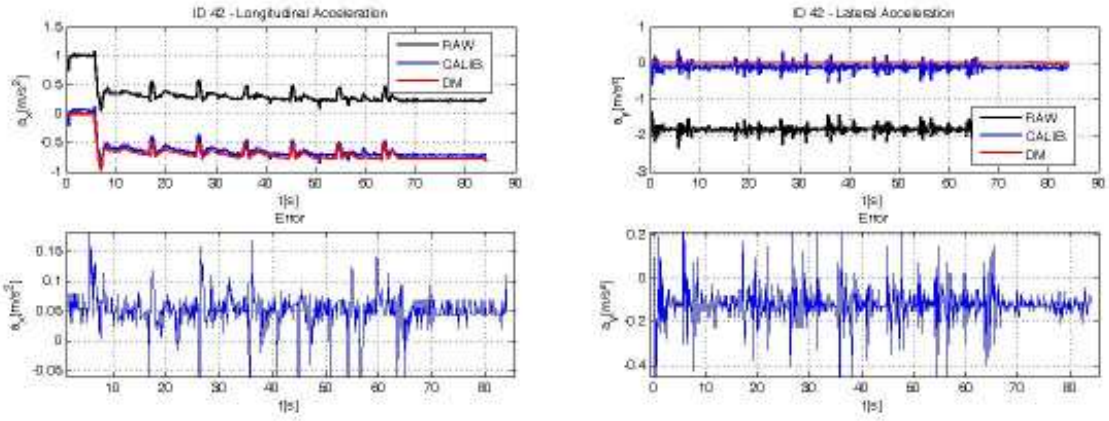

Figure 6.15: Path #42

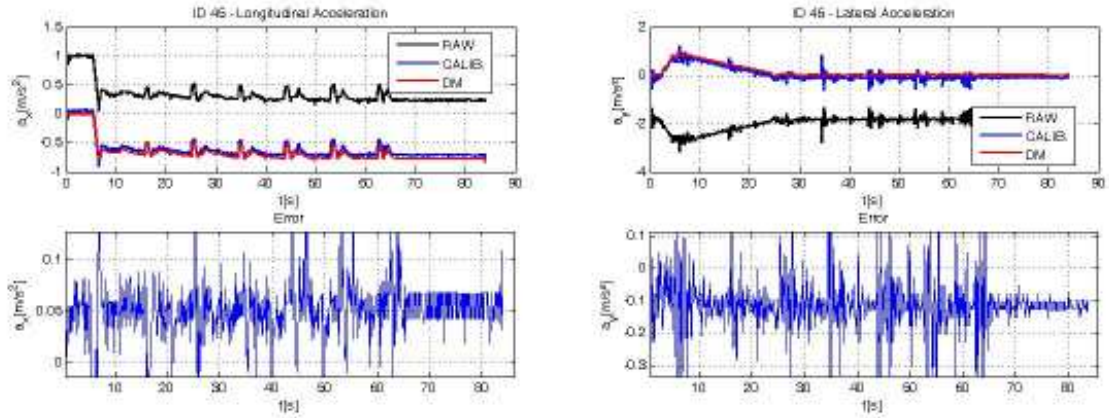

Figure 6.16: Path #45

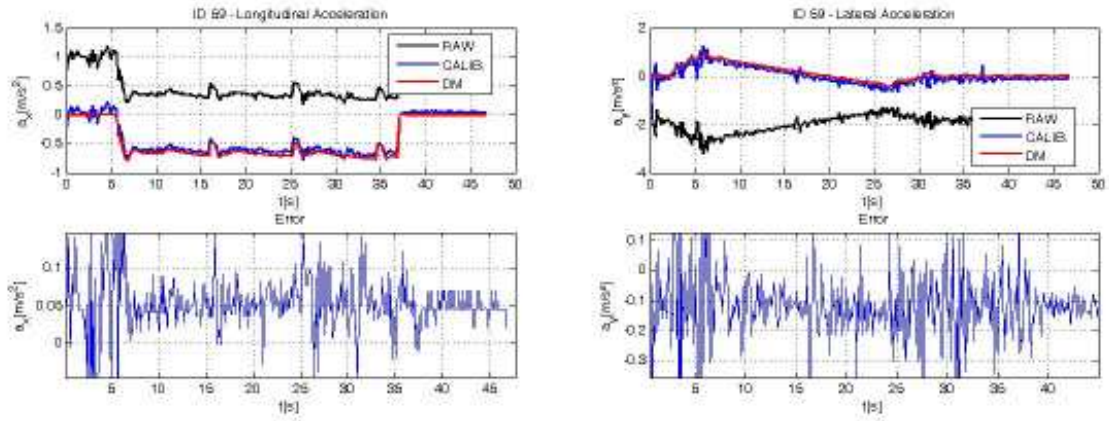

Figure 6.17: Path #59

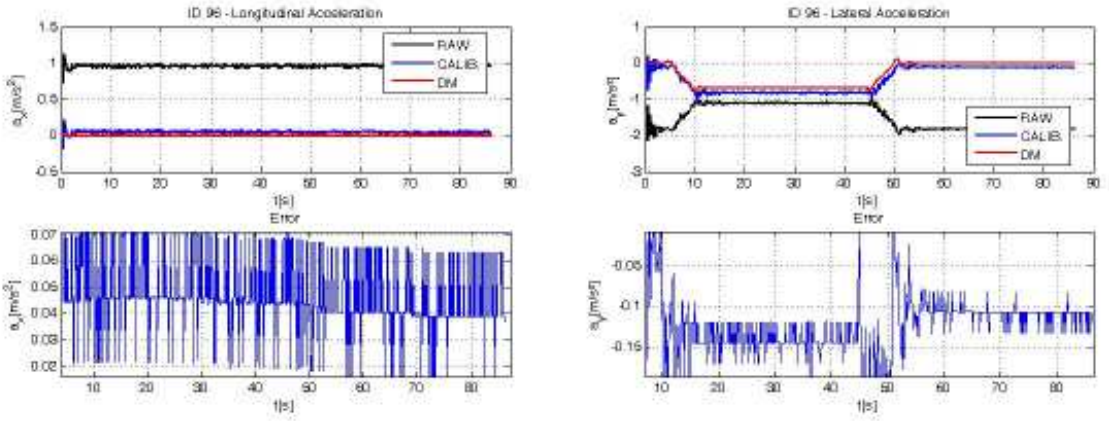

Figure 6.18: Path #96

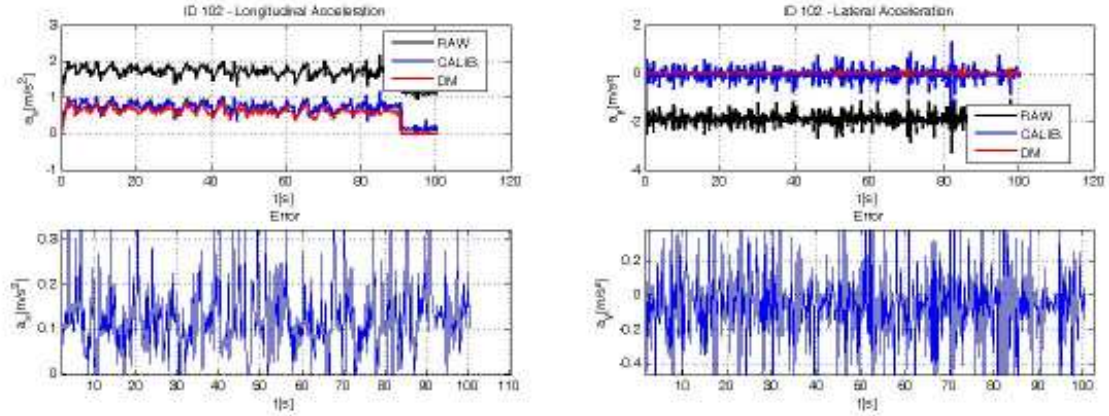

Figure 6.19: Path #102

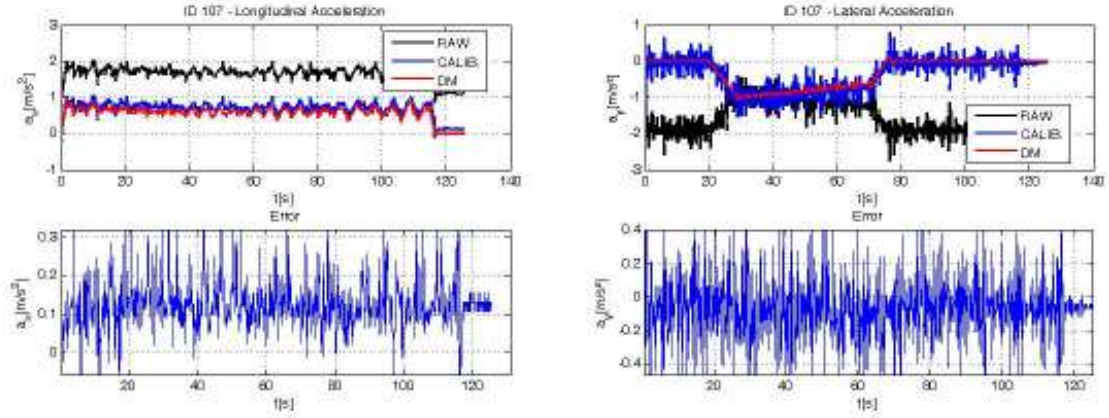

Figure 6.20: Path #107

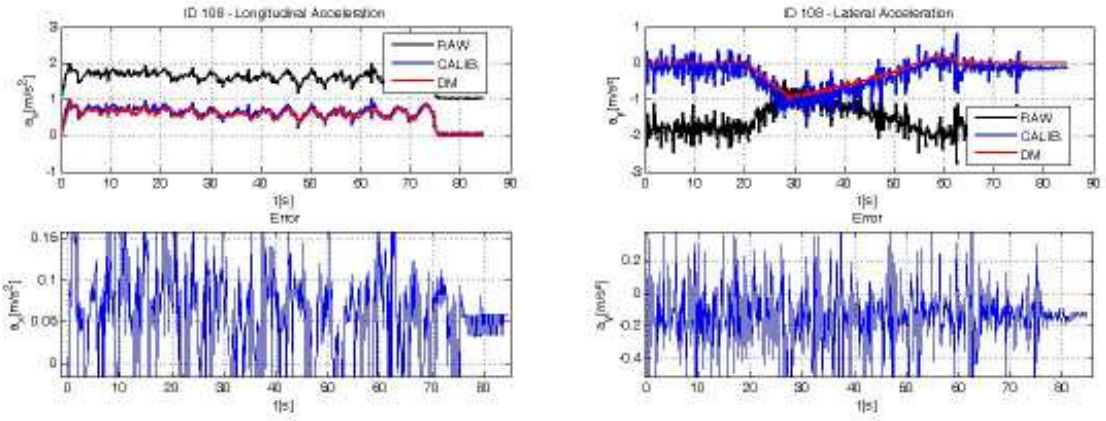

Figure 6.21: Path #108

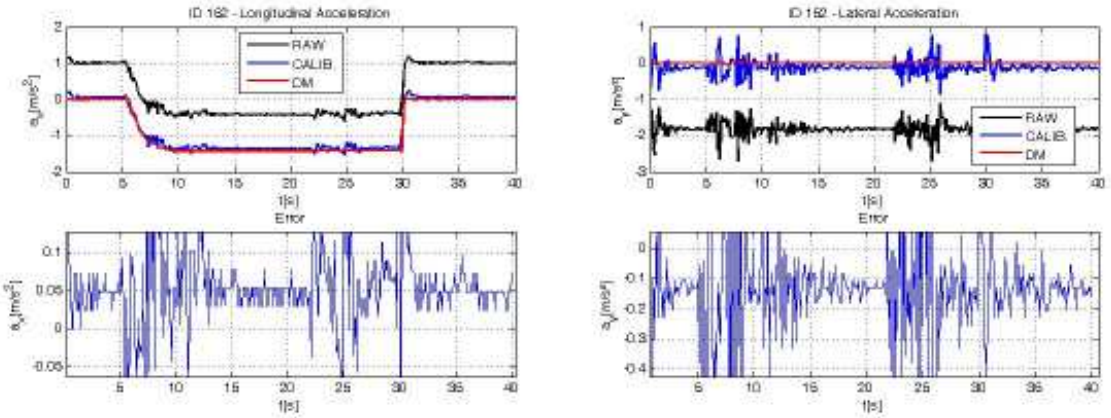

Figure 6.22: Path #152

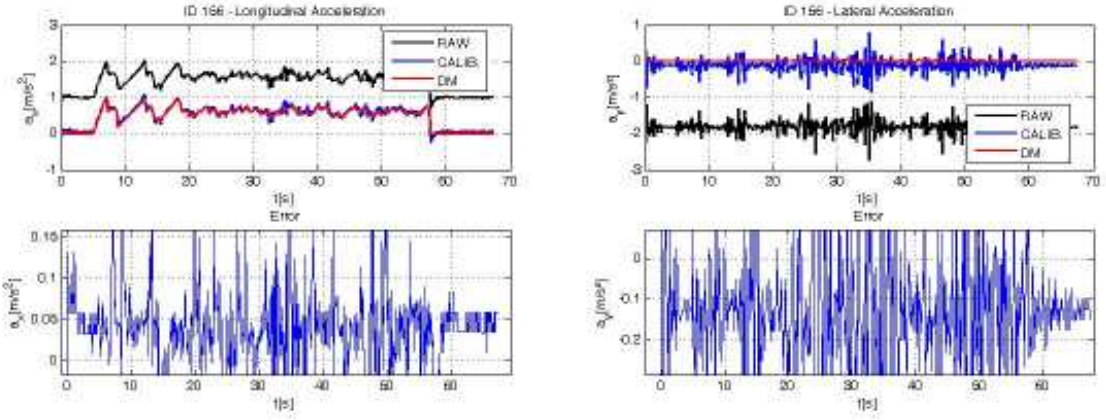

Figure 6.23: Path #156

In the Tab. 6.5 the residual offset, for each channel of each test run, are summarized. It is manifest that the assumption about $\Delta\bar{0}g$=0 is not verified, but it is positive that it assumes a quite constant value. In this way all the deterministic sources of errors can be removed in a calibration phase.

Path	$\Delta\bar{0}g_x$	$\Delta\bar{0}g_y$
6	0.0539	-0.5029
42	0.0493	-0.1188
45	0.0511	-0.1109
59	0.0516	-0.1246
96	0.0460	-0.1227
102	0.1226	-0.0618
107	0.1244	-0.0652
108	0.0517	-0.1396
152	0.0562	-0.1263
156	0.0373	-0.1299
average	0.0644	-0.0999

Table 6.5: Residual offset - accelerometer

6.4.2 Gyroscopes

In this section the graphs of the each of three axes measured by the gyroscope of the custom IMU board are compared to the reference signals, i.e. the ten paths described in the Tab. 5.3.

For each figure the following signals have been reported:

- the reference signal generated by the DM (3D multibody model) - red line;
- the raw measurement of the custom IMU board - black line;
- the calibrated measurement of the custom IMU board, i.e. the raw one compensated through the temperature-based offset - blue line;

The lower subplot sketches the error between the reference signal and the calibrated measurement, in order to find the value of the residual offset.

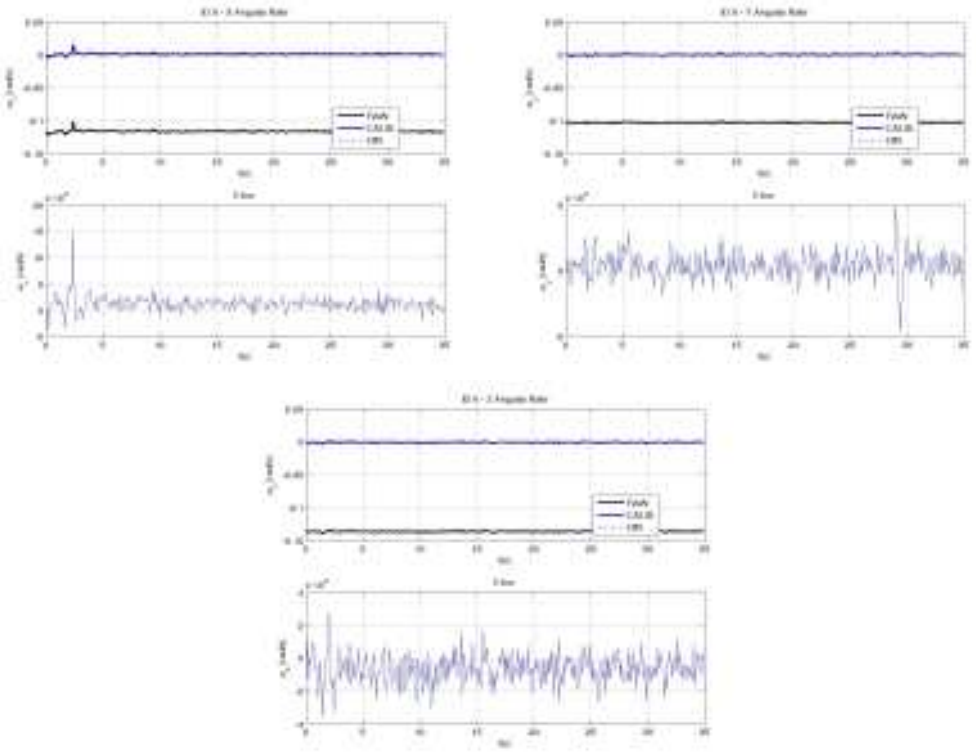

Figure 6.24: Path #6

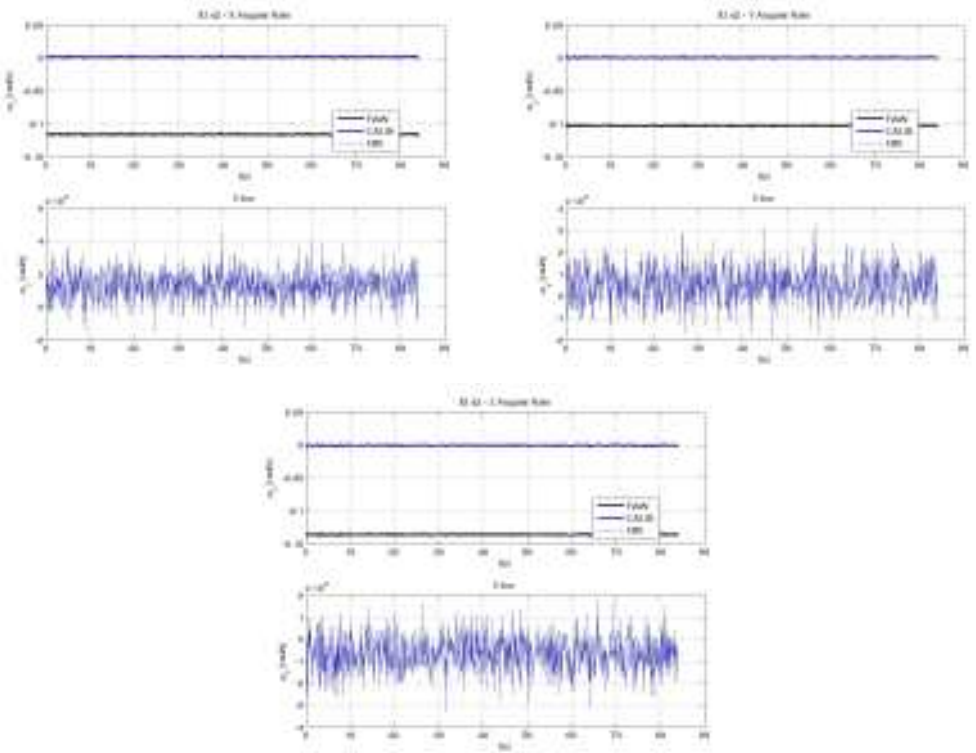

Figure 6.25: Path #42

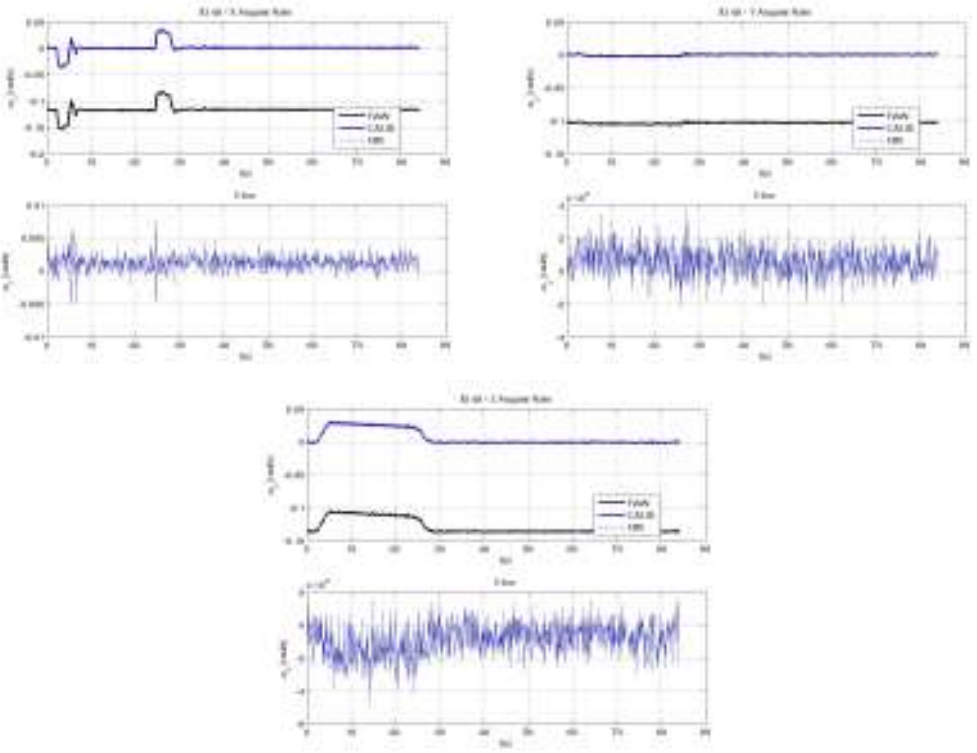

Figure 6.26: Path #45

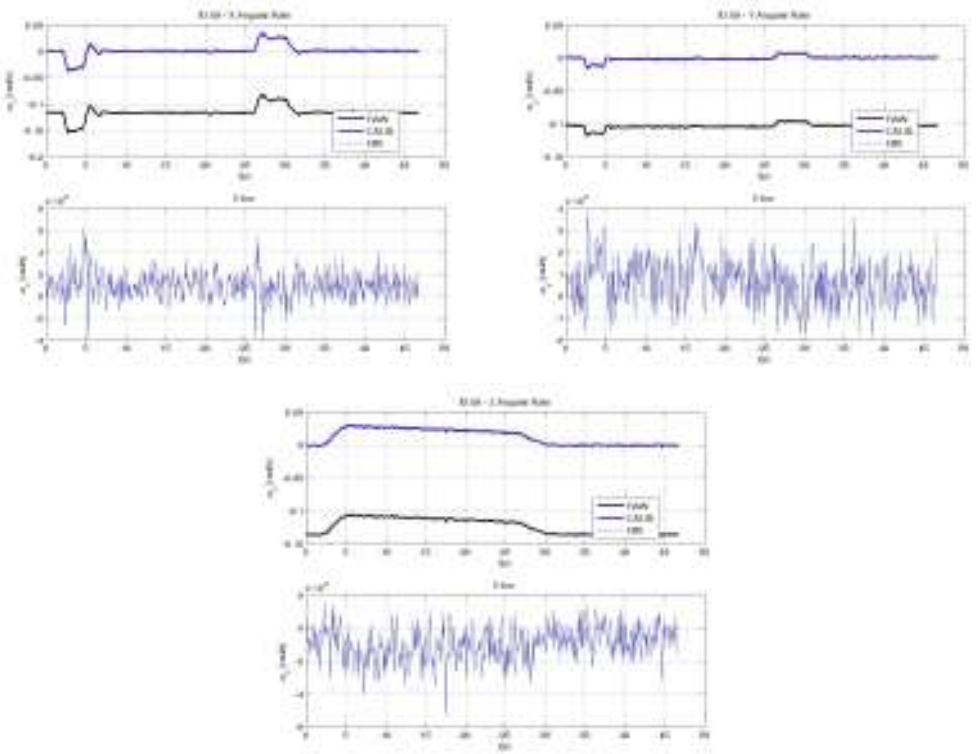

Figure 6.27: Path #59

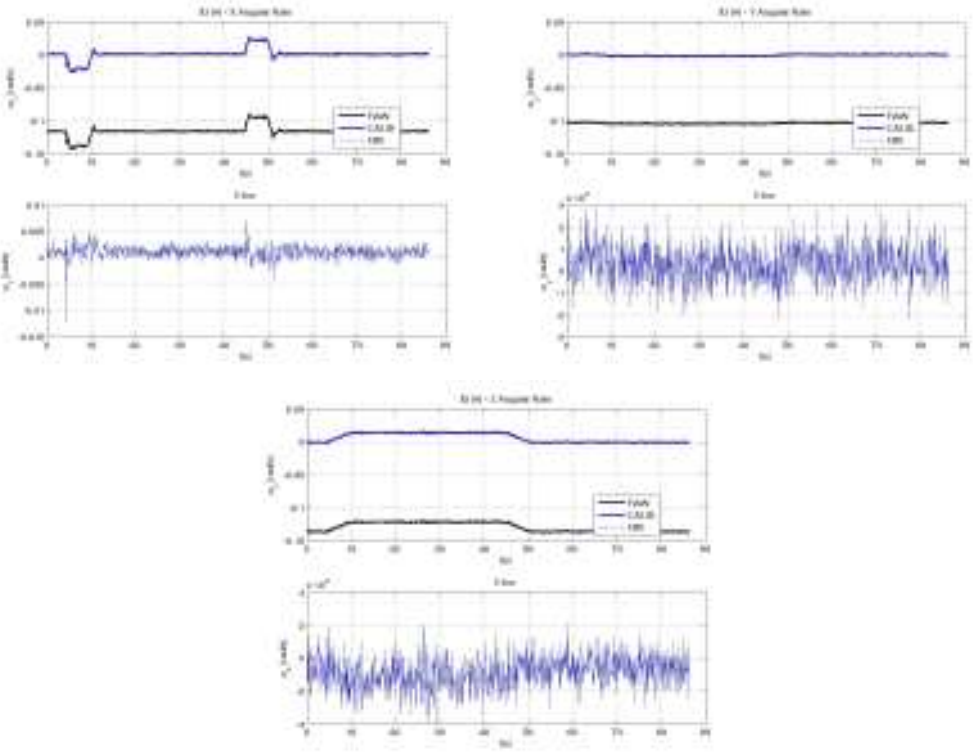

Figure 6.28: Path #96

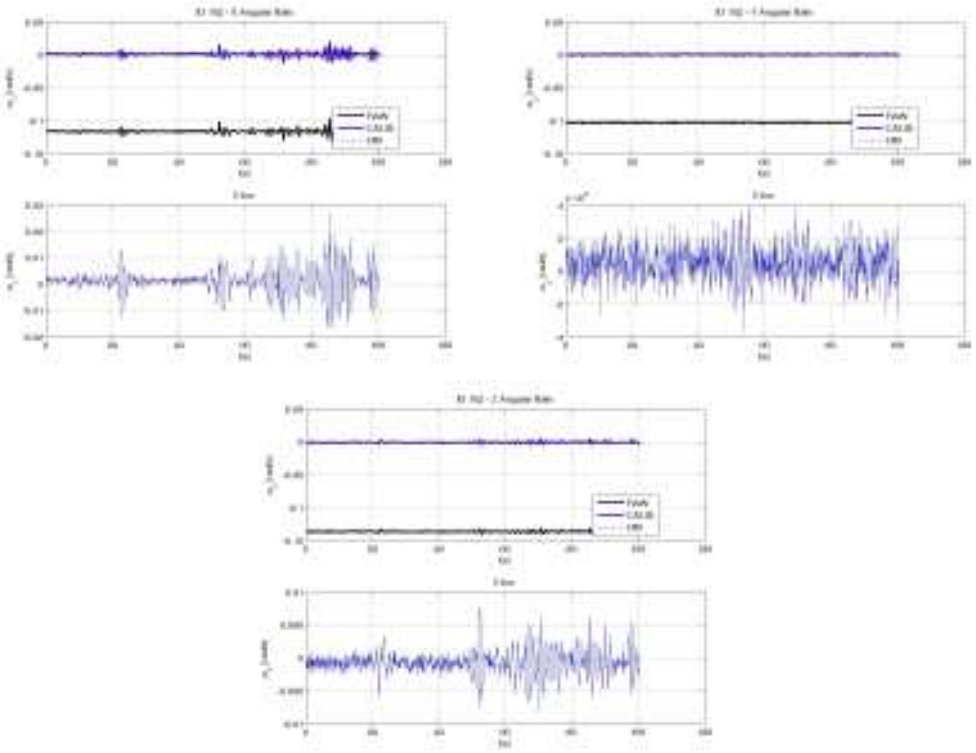

Figure 6.29: Path #102

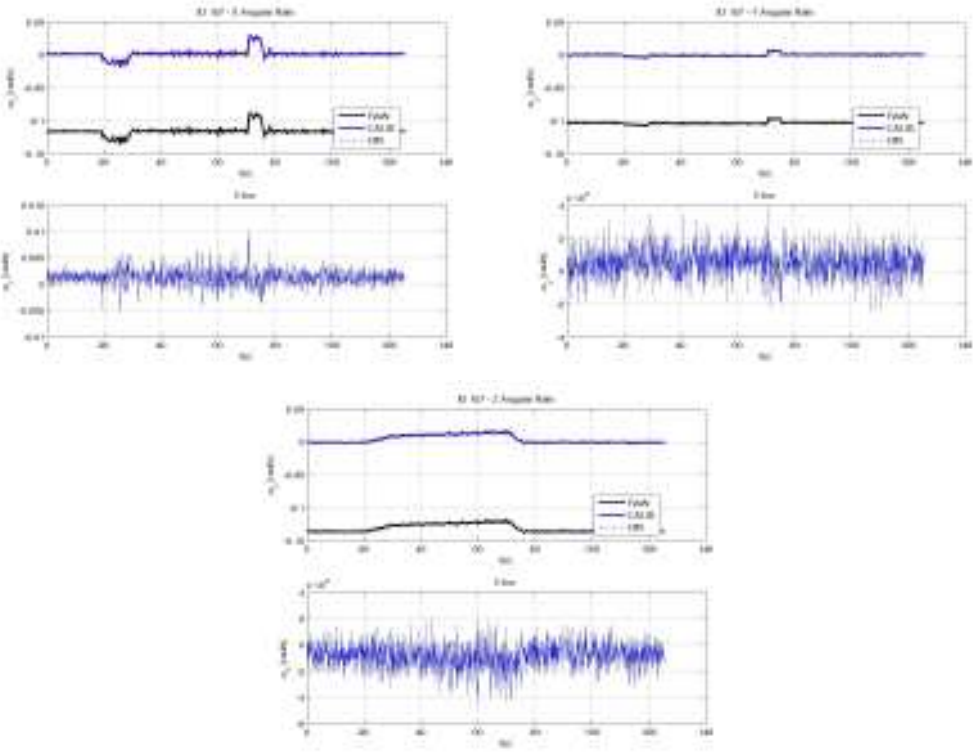

Figure 6.30: Path #107

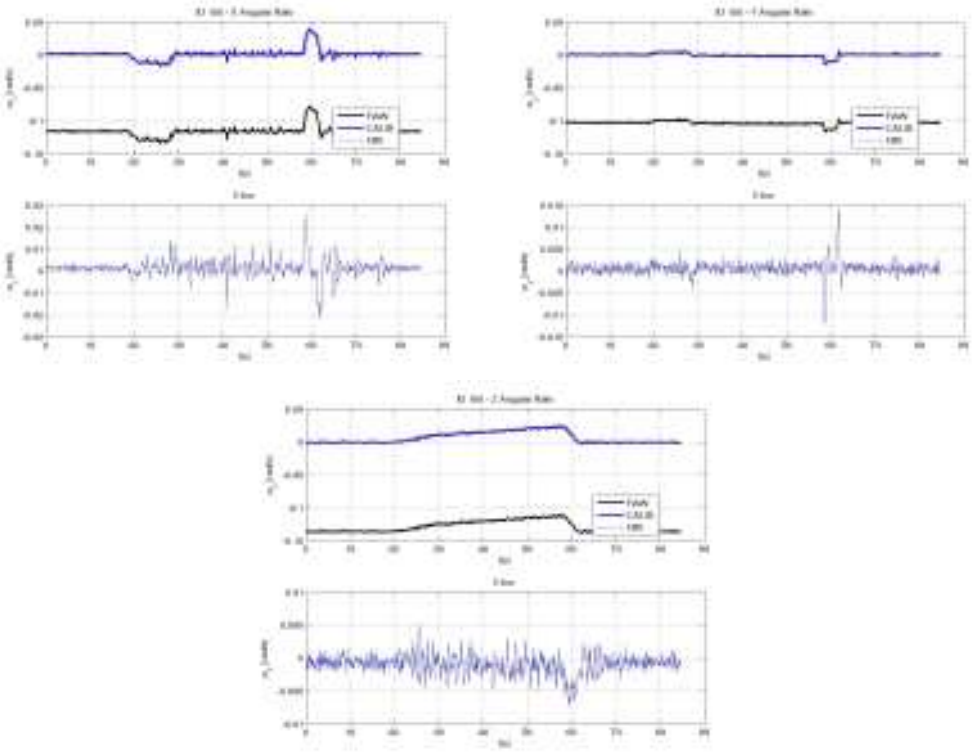

Figure 6.31: Path #108

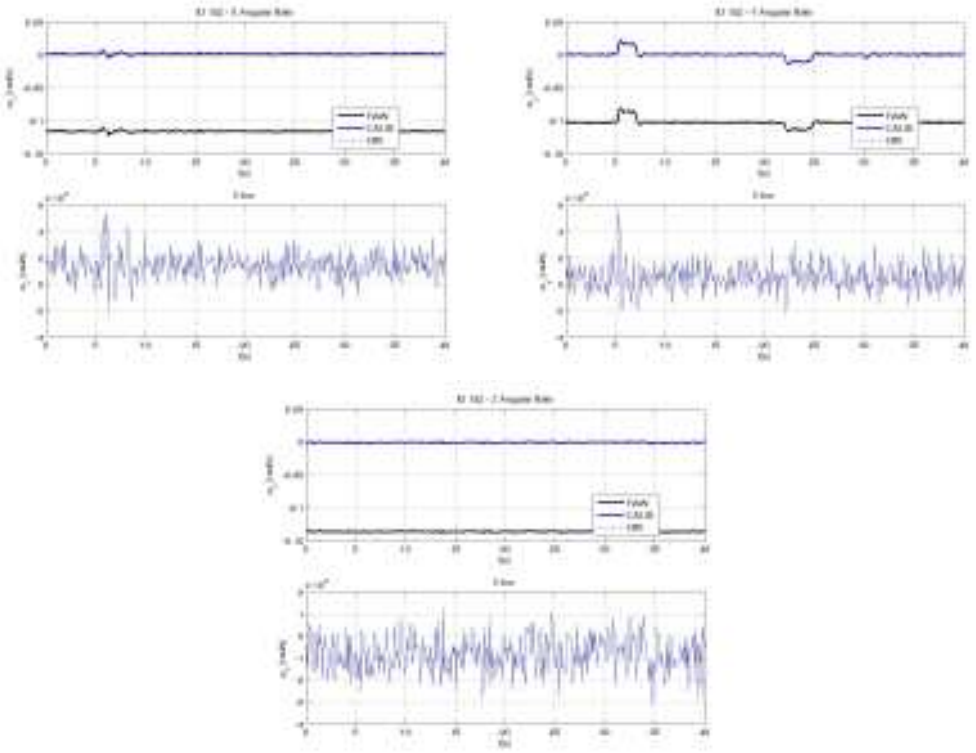

Figure 6.32: Path #152

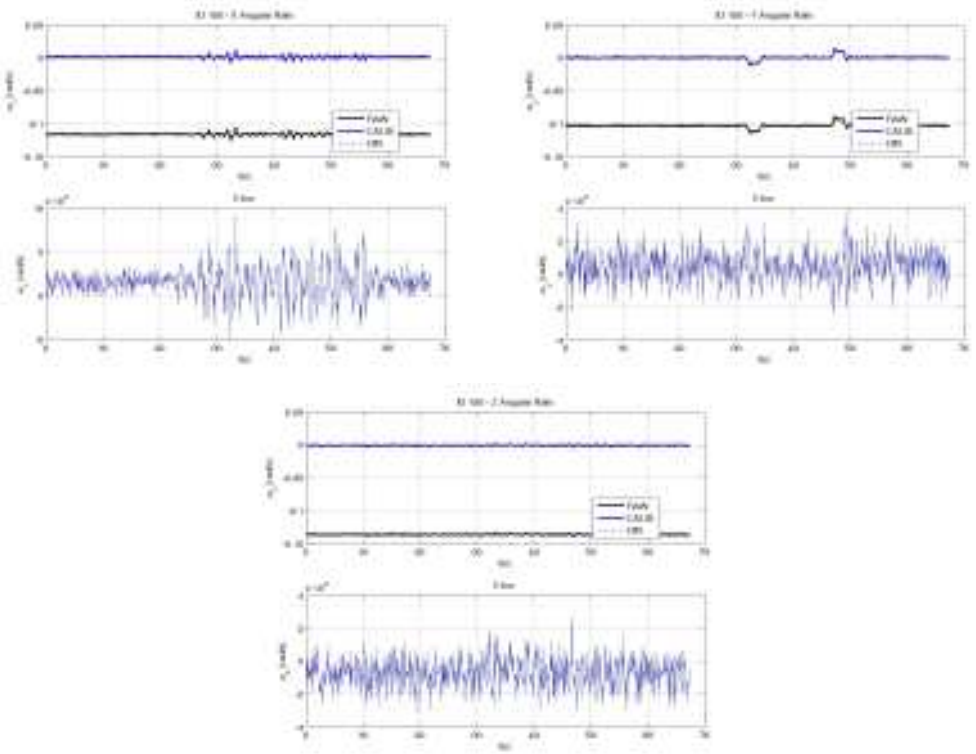

Figure 6.33: Path #156

As for the accelerometers, as in Tab. 6.6, the assumption about $\Delta 0\bar{\text{rate}}$=0 is not verified, even though it assumes a quite constant value. In this way all the deterministic sources of errors can be removed in a calibration phase for the gyroscope, too.

Path	$\Delta 0\bar{\textbf{rate}}_x$	$\Delta 0\bar{\textbf{rate}}_y$	$\Delta 0\bar{\textbf{rate}}_z$
6	0.0013	0.0004	-0.0007
42	0.0013	0.0005	-0.0006
45	0.0013	0.0006	-0.0009
59	0.0009	0.0006	-0.0010
96	0.0011	0.0003	-0.0009
102	0.0013	0.0005	-0.0007
107	0.0014	0.0005	-0.0008
108	0.0014	0.0006	-0.0010
152	0.0014	0.0005	-0.0008
156	0.0016	0.0005	-0.0007
average	0.0013	0.0005	-0.0008

Table 6.6: Residual offset - gyroscope

6.5 Testing of the innovative localization algorithm

The ten paths used in Sect. 3.3 to test the performance of the localization algorithm in a simulated scenario are used, in this case, for the HIL testing through the custom IMU board. In the following pages the graphs of the speed and travelled error estimation error (red line) are sketched in comparison of the corresponding ETCS requirement (green line). The results are good as the histogram of Fig. 6.34 shows: the percentage of time the error does not meet the ETCS requirement is very low (less than 2 % in the worst cases).

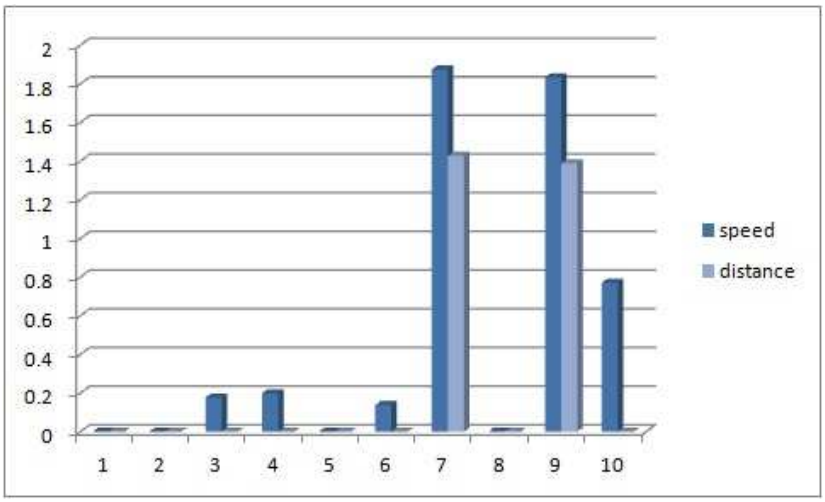

Figure 6.34: Percentage of time the estimates do not meet the ETCS requirements

Path #1

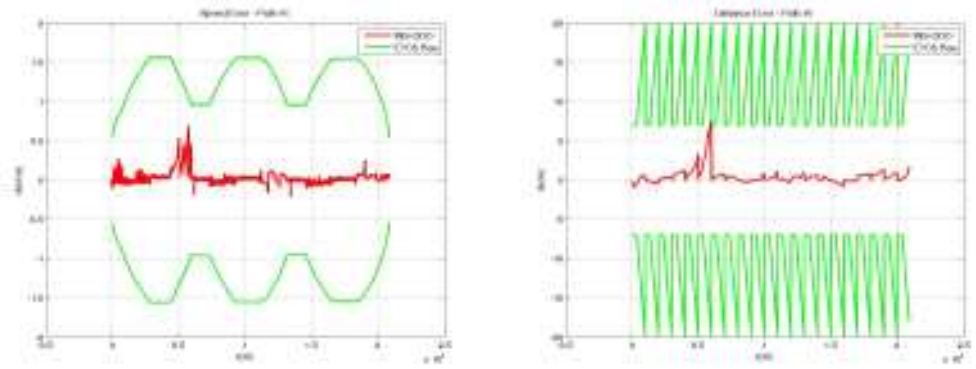

Figure 6.35: Path #1

Path #2

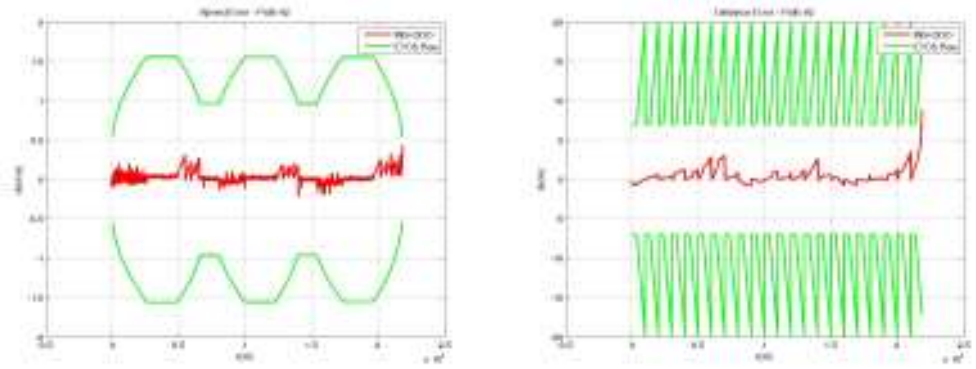

Figure 6.36: Path #2

Path #3

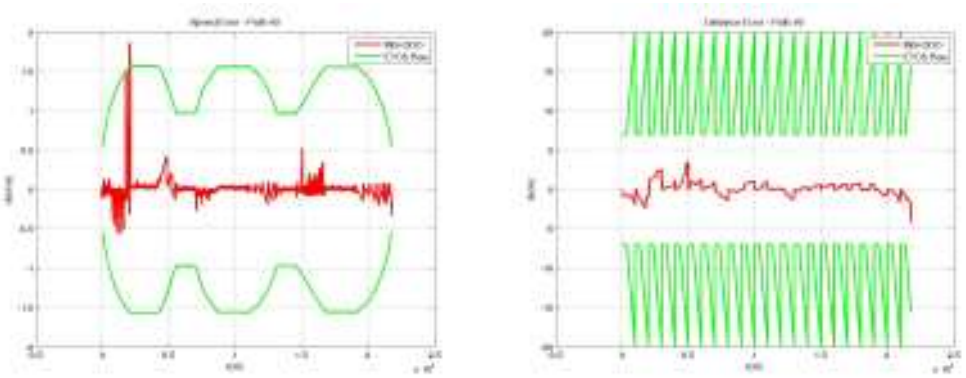

Figure 6.37: Path #3

Path #4

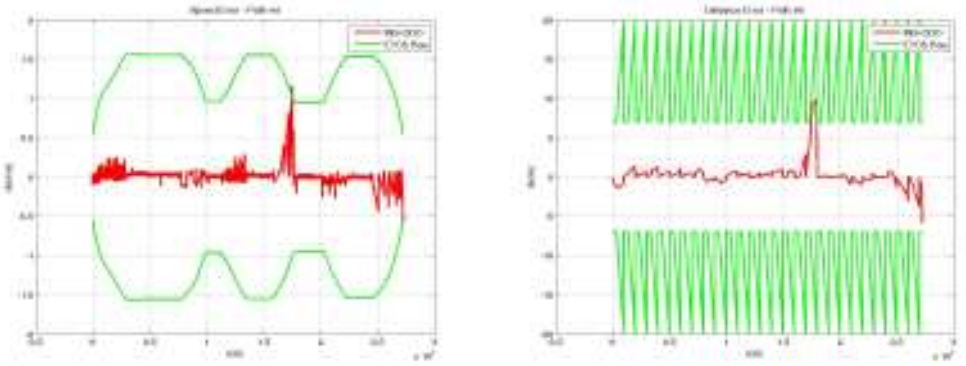

Figure 6.38: Path #4

Path #5

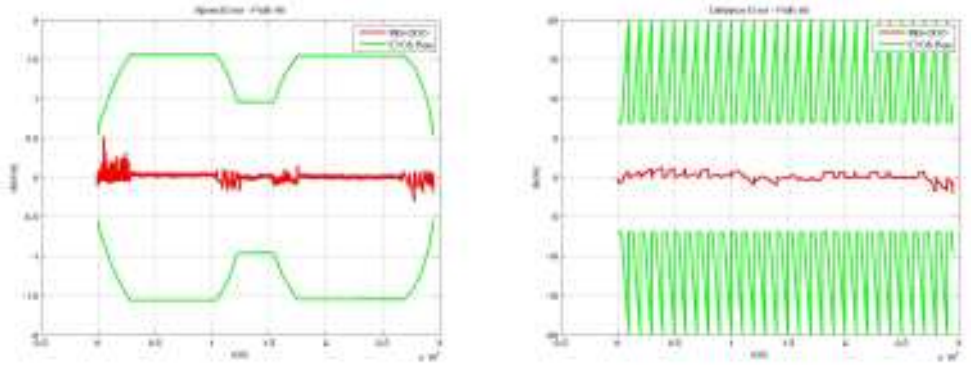

Figure 6.39: Path #5

Path #6

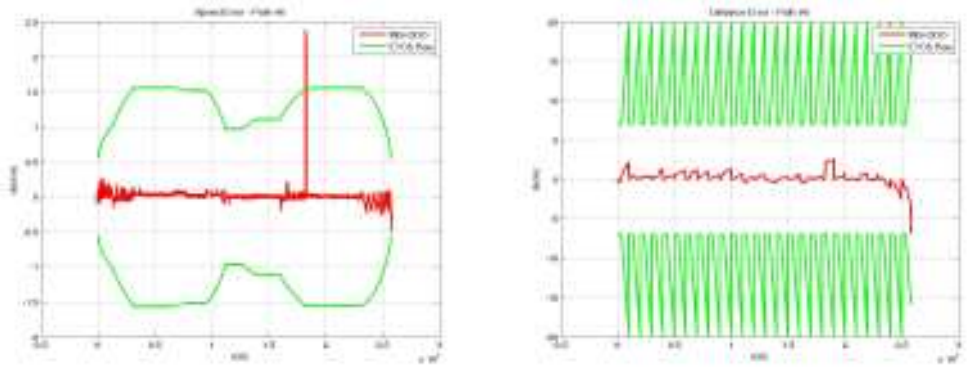

Figure 6.40: Path #6

Path #7

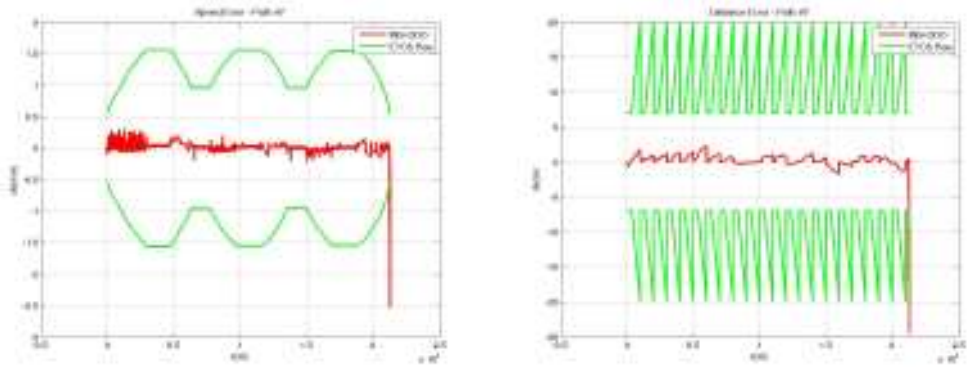

Figure 6.41: Path #7

Path #8

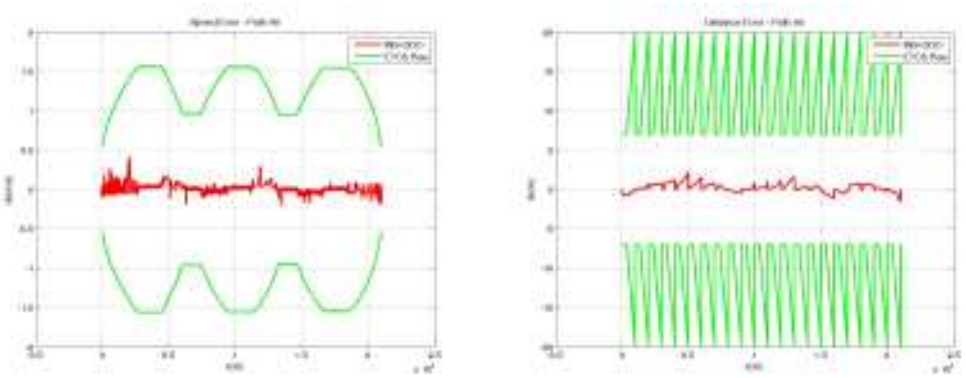

Figure 6.42: Path #8

Path #9

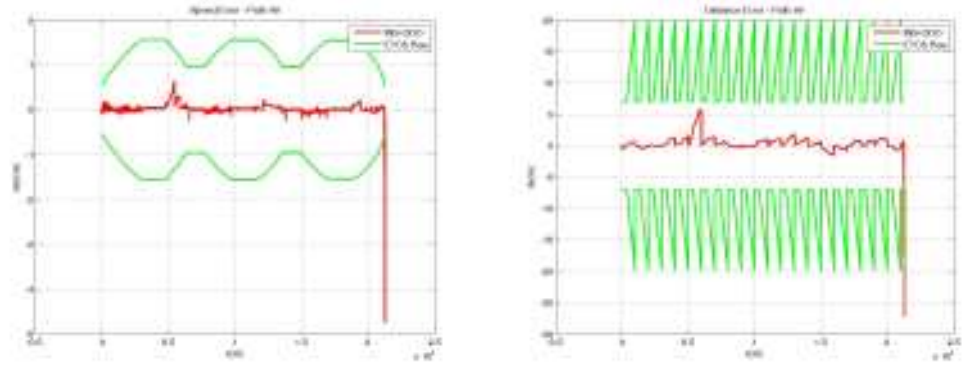

Figure 6.43: Path #9

Path #10

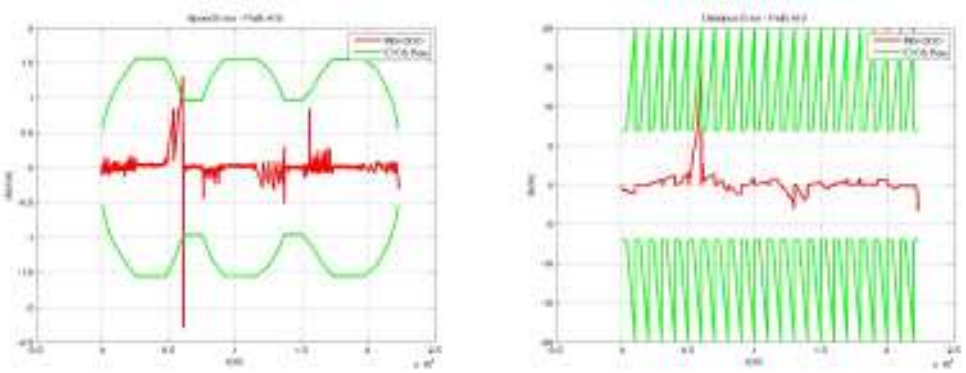

Figure 6.44: Path #10

Conclusions

The aim of this work has been the development of an innovative localization algorithm which could enhance the performance, in terms of speed and position estimation accuracy, of the classical odometry algorithms, such as the Italian SCMT, based on the measurement of the tachometers assembled on the axles of the wheels.

The state of the art of odometry algorithms has been investigated and different sensors have been analyzed. The solution proposed consists of a sensor fusion technique which fuses the information from an odometer and an IMU, thanks to the Kalman Filter theory.

The main features of the localization algorithm have been summarized and the sensor output signals have been simulated through a 3D multibody model of a railway vehicle. A huge number of simulated paths with a wide range of working conditions and track configurations has been used to test the algorithm.

The preliminary results show a significant improvement of the position and the speed estimation, compared to classical SCMT algorithm, using the percentage of time the error signal does not meet the ETCS requirements as performance parameter.

The work then has provided the development of a custom IMU board which has been designed by ECM in order to meet their industrial and business requirements (low-cost, easy-to-install, custom size). For this aim the using of the emergent MEMS sensors has been considered.

The board has been tested by the Department of Energy Engineering through the HIL test rig developed as a dynamic simulator for the testing of the inertial sensors and navigation algorithms.

The implementation of the HIL test rig has represented a strength for this work, since a method with general applicability in all fields dealing with inertial sensors has been developed.

The HIL test rig includes an industrial robot devoted to replicate the motion of the IMU to be tested, according to suitable washout filters design and kinematic data, produced by dynamic vehicle simulation or real test runs. This strategy has been tested by means of an “open” robot controller and a commercially available

IMU. The results have shown the possibility to replicate the most relevant frequencies of acceleration and angular rate signals of typical railway vehicle test runs.

Through the HIL test rig it has been possible to apply the testing procedure of the innovative localization algorithm to a set of ten worst-case-design paths, all characterized by a high degree of weakness, since the high level of stress imposed to the sensors.

The obtained results confirm the good prospects of the simulated testing: the speed and the position errors are always much smaller than the speed and position ERTMS requirement thresholds. At the same time the accuracy of the estimation is much greater than that provided by the classical algorithms.

In the next spring the final testing of the proposed algorithm will be performed through appropriate on-track tests. If the good results will be confirmed, the custom IMU board and the innovative localization algorithm will be included in the portfolio of products provided by ECM.

Figure 6.45: HIL test rig

Bibliography

[1] IEEE Standard. *Standard for Inertial Sensor Terminology*. IEEE. 2001.

[2] UIC B126.15. *Braking Questions Methodology for the Safety Margin ETCS/ERTMS*. Union International des Chemins de fer. 2006.

[3] UIC B126.15. *Braking Questions Safety Margins for Continuous Speed Control Systems on Existing Lines and Migration Strategy for ETCS/-ERTMS*. Union International des Chemins de fer. 2005.

[4] AA.VV. "Odometria SCMT: Principi generali dell'algoritmo per il calcolo della velocitÃ stimata in caso di pattinamento o slittamento degli assi di misura". In: *Trenitalia - Unità Tecnologie Materiale Rotabile, Direzione Ricerca Ingegneria e Costruzioni - Specifica Requisiti Funzionali, specifica n^o 372574 esp. 03* (10/10/2001).

[5] B. Allotta, Bioli, and V. G. Colla. "'Kinematic Control of Robots With Joint Constraints". In: *Journal of Dynamic Systems, Measurement, and Control* 121 (1999), pp. 433–442.

[6] B. Allotta, V. Colla, and M. Malvezzi. "Train position and velocity estimation using wheel velocity measurements". In: *Proc. of the IMechE, Journal of Rail and Rapid Transit* 216 (2002), pp. 207–225.

[7] B. Allotta, L. Pugi, et al. "Evaluation of odometry algorithm performances using a railway vehicle dynamic model". In: *Vehicle System Dynamics* 50.5 (2012), pp. 699–724. DOI: 10.1080/00423114.2011.628681.

[8] Y. Bar-Shalom, X.R. Li, and T. Kirubarajan. *Estimation with Applications to Tracking and Navigation: Theory Algorithms and Software*. Wiley-Interscience publication. Wiley, 2004.

[9] N. Bin. "Analysis of train braking accuracy and safe protection distance in automatic train protection (ATP) systems". In: *Proc. of the 5th COMPRAIL*. Berlin, 1996, pp. 11,118.

[10] G. Cocci, M. Malvezzi, et al. “Braking Performance Monitoring in Service for the Validation of the Safety Margins used for the Definition of Braking Curves of ATP/ATC Systems”. In: *Proceedings of WCRR2006*. Montreal, 2006.

[11] V. Colla, M. Vannucci, et al. “Estimation of train speed via neuro—fuzzy techniques”. In: *Proceedings of the 7th International Work-Conference on Artificial and Natural Neural Networks: Part II: Artificial Neural Nets Problem Solving Methods*. IWANN ’03. Menorca, Spain: Springer-Verlag, 2003, pp. 497–503.

[12] H.F Durrant-Whyte and B. Barshan. “Inertial navigation systems for mobile robots”. In: *IEEE Transactions on Robotics and Automation* 11 Issue 3 (1195), pp. 328 –342.

[13] N. El-Sheimy, S. Nassar, and A. Noureldin. “’Wavelet de-noising for IMU alignment”. In: *Aerospace and Electronic Systems Magazine, IEEE* 19 (2004), pp. 32 –39.

[14] P. Ernest, R. Mazl, and L. Preucil. “Train Locator Using Inertial Sensors and Odometer”. In: *IEEE Intelligent Vehicles Symposium*. University of Parma, 2004, pp. 860–865.

[15] C. Esveld. *Modern Railway Track*. Delft, Netherlands: Delft University of Technology, 2001.

[16] D. Ferrazzin. “’Study and Design of Motion Base for Driving Simulators”. Ph.D. diss. Pisa, Italy: Scuola Superiore di Studi Universitari e di Perfezionamento S.Anna, 2001.

[17] D. Gebre-Egziabher. “Design and Performance Analysis of a Low-Cost Aided Dead Reckoning Navigator”. Ph.D. diss. Standford, USA: Standford University, 2004.

[18] S. Godha. *Performance Evaluation of Low Cost MEMS-Based IMU Integrated with GPS for Land Vehicle Navigation Application*. 2006.

[19] Peter R. Grant and Lloyd D. Reid. “Motion Washout Filter Tuning: Rules and Requirements”. In: *Journal of Aircraft* 34.2 (1997), pp. 145–151.

[20] Peter R. Grant and Lloyd D. Reid. “PROTEST: An Expert System for Tuning Simulator Washout Filters”. In: *Journal of Aircraft* 34.2 (1997), pp. 152–159.

[21] A. Heidari, M.A. Sandidzadeh, and S. Farshad. “A novel method for estimation of train speed and location using traction motor voltage and current”. In: *Proceedings of the Institution of Mechanical Engineers, Part F: Journal of Rail and Rapid Transit* 226, Iss: 4 (2012), pp. 421–433.

[22] H. Hou. *Modeling Inertial Sensors Errors Using Allan Variance*. 2004.

[23] S. Iwnicki. *Handbook of Railway Vehicle Dynamics*. Taylor and Francis, 2006.

[24] A. Khodadadi, A. Mirabadi, and B. Moshiri. "Assessment of particle filter and Kalman filter for estimating velocity using odometery system". In: *Sensor Review* 30, Iss: 3 (2010), pp. 204–209.

[25] M. Malvezzi. "Odometry Algorithms for Railway Applications". Ph.D. diss. Bologna, Italy: Università degli Studi di Bologna, 2003.

[26] M. Malvezzi, B. Allotta, and L. Pugi. "Feasibility of Degraded Adhesion Tests in a Locomotive Roller Rig". In: *Proc. of the ImechE, Part F, Journal of Rail and Rapid Transit* 222 (2008).

[27] M. Malvezzi, B. Allotta, and M. Rinchi. "Odometric estimation for automatic train protection and control systems". In: *Vehicle System Dynamics: International Journal of Vehicle Mechanics and Mobility* 49 (2010), pp. 723–739.

[28] M. Malvezzi, F. Bartolini, et al. *Analysis of braking performance for the definition of emergency braking intervention in ATP systems*. Vol. Advanced Train Control Systems. WIT Press - Ning, Bin, 2010, pp. 133–142.

[29] G. Marani, J. Kim, et al. "A real-time approach for singularity avoidance in Resolved Motion Rate Control of Robotic Manipulators". In: *Proc. of the 2002 IEEE International Conference on Robotics and Automation*. Washington DC, USA, 2002.

[30] E. Meli, M. Malvezzi, et al. "A railway vehicle multibody model for real-time applications". In: *Vehicle System Dynamics* 46 Issue 12 (2008), pp. 1083–1105.

[31] R. Merry, R. van de Molengraft, and M. Steinbuch. "Error modeling and improved position estimation for optical incremental encoders by means of time stamping". In: *Proceedings of the 2007 American Control Conference*. 2007.

[32] A. Mirabadi, N. Mort, and F. Schmid. "Application of sensor fusion to railway systems". In: *IEEE/SICE/RSJ International Conference on Multisensor Fusion and Integration for Intelligent Systems*. 1996, pp. 185–192.

[33] A. Mirabadi, N. Mort, and F. Schmid. "Fault detection and isolation in multisensor train navigation systems". In: *UKACC International Conference on Control(Conf. Publ. No. 455)*. 1998, pp. 969–974.

[34] Ahmad Mirabadi, Felix Schmid, and Neil Mort. "Multisensor Integration Methods in the Development of a Fault-Tolerant Train Navigation System". In: *The Journal of Navigation* 56 (03 Aug. 2003), pp. 385–398. ISSN: 1469-7785.

[35] Meyer A. Nahon and Lloyd D. Reid. “Simulator Motion-Drive Algorithms: A Designer’s Perspective”. In: *Journal of Guidance, Control, and Dynamics* 13.2 (1990), pp. 356–362.

[36] S. Nassar. “Improving the Inertial Navigation System (INS) Error Model for INS and INS/DGPS Applications”. Ph.D. diss. Calgary, Canada: Department of Geomatics Engineering, University of Calgary, 2003.

[37] “Odometer FFFIS”. In: *EEIG 97E2675B* Version5 (31/07/98).

[38] “Performance Requirements for STMs”. In: *EEIG ERTMS Users Group - Reference EEIG Subset 059* Issue 0.0.6 (28/03/00).

[39] “Performance Requirements for STMs”. In: *EEIG ERTMS Users Group - Reference EEIG Subset 041* Issue 2.0.0 (30/03/00).

[40] M. Petovello. “Real-time Integration of a Tactical-Grade IMU and GPS for High- Accuracy Positioning and Navigation”. Ph.D. diss. Calgary, Canada: Department of Geomatics Engineering, University of Calgary, 2003.

[41] L. Pugi, M. Malvezzi, et al. “Simulation of WSP Systems on MI-6 Test rig”. In: *Vehicle System Dynamics* 44 (Supplement 2006), pp. 843–852.

[42] L. Pugi, M. Rinchi, et al. “Development of an experimental rig for HIL testing of Railway Radar Speed Sensors”. In: *Railway Engineering-2004*. Commonwealth Institute, London, 2004.

[43] C. W. Schwarz. “Two Mitigation Strategies for Motion System Limits in Driving and Flight Simulators”. In: *Trans. Sys. Man Cyber. Part A* 37.4 (July 2007), pp. 562–568.

[44] Sintesi S.C.p.A. *C4G Open Library User’s Guide v1.2.3*. 2008.

[45] Sintesi S.C.p.A. *Orchestra Core User’s Guide v1.8.0*. 2010.

[46] Sintesi S.C.p.A. *Orchestra Designer User’s Guide v2.3.2*. 2010.

[47] Sintesi S.C.p.A. *Orchestra HMI Human Machine Interface User’s Guide v1.8.0*. 2010.

[48] Sintesi S.C.p.A. *Orchestra v3.5-1 Installation Procedure v1.0.0*. 2010.

[49] Eun-Hwanr Shin. “Estimation Techniques for Low-Cost Inertial Navigation”. Ph.D. diss. Calgary, Canada: Department of Geomatics Engineering, University of Calgary, 2005.

[50] B. Siciliano, L. Sciavicco, et al. *Robotics: Modelling, Planning and Control*. Advanced Textbooks in Control and Signal Processing. Springer, 2011.

[51] Bruno Siciliano. “Kinematic control of redundant robot manipulators: A tutorial”. English. In: *Journal of Intelligent and Robotic Systems* 3 (3 1990), pp. 201–212. ISSN: 0921-0296.

[52] COMAU S.p.A. *C4G OPEN Software di Sistema Rel. 3.1x*. 2003.

[53] COMAU S.p.A. *EZ PDL2 Ambiente di programmazione facilitato Software di Sistema Rel. 2.4x*. 2005.

[54] COMAU S.p.A. *SMART SiX Specifiche Tecniche*. 2005.

[55] “Specific Transmission Module FFFIS”. In: *EEIG ERTMS Users Group - Reference EEIG Subset 035* Issue 2.0.0 (30/03/00).

[56] G. Strang and T. Nguyen. *Wavelets and Filter Banks*. Wellesley-Cambridge Press, 1996.

[57] D.H. Titterton and J.L. Weston. *Strapdown Inertial Navigation Technology - 2nd Edition*. Eds. Institution of Electrical Engineers, Stevenage, UK: In IEE Radar, Sonar, Navigation and Avionics Series 17, N. Stewart, H. Griffiths, 2004.

[58] Xsens Technologies B. V. *MTi-G User Manual and Technical Documentation*. 2009.

[59] G. Vicuna. *Organizzazione e Tecnica Ferroviaria*. Roma, Italy: Ed. CIFI, 1986.

[60] G. Welch and G. Bishop. *An Introduction to the Kalman Filter*. 1995.

[61] Oliver J. Woodman. *An introduction to inertial navigation*. Tech. rep. UCAM-CL-TR-696. University of Cambridge, Computer Laboratory, Aug. 2007.